Quantifying Disequilibrium in U-Series Decay using High-Purity Germanium Spectrometry

Thesis submitted in accordance with the requirements of the University of Liverpool for the degree of Doctor in Philosophy

by

Sumia Abdualhadi

Oliver Lodge Laboratory

2016

Abstract

Many of the naturally occurring radioactive elements are members of radioactive decay chains. These chains originate from parent nuclides with very long half-lives and end with a stable nuclide of lead. In any natural material containing uranium which was not disrupted, a state of secular equilibrium will occur between parent nuclide and its daughter products. However, when sedimentary deposits are formed, many geological processes can occur which may cause isotopic fractionation of the elements resulting in a state of disequilibrium between the parent nuclide and its daughters in the chain. This study is aimed at the determination of the activity concentrations of radionuclides from U-series decay and hence quantifying possible disequilibrium in 14 sediment samples selected from four different locations. Six samples were collected from Namibia in the South Africa, four samples were from the Cambridge Gulf in Western Australia and the four remaining samples were from Czech Republic and South Germany regions in Europe. This work was carried out with a novel Broad Energy Germanium (BEGe) detector inside a 50mm thick lead shield. The BEGe detector utilises a novel point like electrode structure which through extremely low capacitance (1pF) provides excellent an energy resolution at low energy. This performance is far superior to conventional germanium detectors, which enables a potential step change in the ability to resolve low energy peaks on a background. Gamma-ray energy resulting in excellent spectra. Gamma-ray transitions lines ranging from 46 keV up to 1.7 MeV associated with decay products of the ^{238}U and ^{232}Th decay chains have been analysed separately to obtain more statistically significant overall results. In the measurements of environmental samples using gamma-ray spectrometry, the main concern is a reliable efficiency calibration. This is crucial especially for the analysis of low-energy gamma emitters (<100 keV) such as ^{210}Pb (46.5 keV) and ^{234}Th (63.3 keV and 92.6 keV). Modelled efficiency calibrations using the LabSOCS (Laboratory Sourceless Object Calibration Software) were applied within this work. A series of validation tests was performed and evaluated for different sample types, densities and volumes. Using

this method, an improvement can be obtained in the reliability of the derived activity concentrations.

The sample preparation and the gamma-ray spectroscopic analysis technique are discussed in detail. The specific activities of radionuclides from the ^{238}U decay chain ranged from 16.8 ± 2.3 to 80 ± 5 Bq/kg for ^{234}Th, from 14 ± 3 to 98 ± 6 Bq/kg for ^{226}Ra, from 16.8 ± 0.6 to 116 ± 3 Bq/kg for ^{214}Pb, from 16.6 ± 0.7 to 112 ± 3 for ^{214}Bi and from 15.9 ± 2.6 to 114 ± 8 Bq/kg for ^{210}Pb. Six samples were found to be in disequilibrium as a result of an excess in ^{226}Ra activity concentrations. The ^{226}Ra/^{238}U activity ratio in these samples ranged from 1.22 ± 0.13 to 1.77 ± 0.15. Notably, these samples were collected from an area in Namibia where leaching of radium has taken place. In the remaining samples the results showed secular equilibrium. The activity concentrations of ^{228}Ac ranged from 20.6 ±1.0 to 60.6 ± 2.0 Bq/kg, of ^{212}Pb from 20.0 ± 0.9 to 59.7 ± 2.5 Bq/kg and of ^{208}Tl from 21.1 ± 1.0 to 58.6 ± 2.4 Bq/kg, from ^{232}Th decay chain. All results show secular equilibrium for this decay chain.

The results obtained for the uranium and thorium concentrations some of the investigated samples are consistent with mass spectrometry (ICP-MS) and other gamma-ray spectrometry measurements.

Acknowledgements

I would like to thank Allah who granted me the health and strength that allow me to overcome lifes difficulties, fulfill my responsibilities as a mother for five children and accomplish this academic achievement. Above all, I would like to thank my beloved husband, Saad Omar, for his encouragement to undertake the PhD. journey. Without his love, support and patience I would have done nothing. I will never forget his choice to leave his own career and be with me during my study. I owe him a debt of gratitude and will continue for my whole life. I would also like to thank my sons; Sand, Suhil, Sif-Dein and the little one Saji and my daughter Sama for dealing with a student mother who was even more stressed and busy than usual. I will never forget the strength that they provided me with their prayers all the times. I would like to thank my parents, sisters and brothers for their support during the difficult times.

I would like to express my gratitude to my supervisors, Prof. Paul Nolan, Dr. David Joss and Dr. Barbara Mauz for their trust in me, which encouraged me to know the strength in myself, and motivated me to work harder and achieve this success. Their incredible attention, explanations, advice, and guidance are highly appreciated. Also I will not forget to thanks Dr. Barbara for her generous help in sample collection, without which I could never finish the practical part of my research.

Special thanks to Mr. Mike ÓConnor, technician from the School of Environmental Science, University of Liverpool, for the valuable technical support with XRF technique, Mr. Stephen Chappell, physics technician at the Central Teaching Laboratory, University of Liverpool, for his help during the samples analysis with gamma-ray spectrometry and Prof. John Boyle from the School of Environmental Science, University of Liverpool, for his assistance in processing XRF technique data. Without their help this research could not be finished. Appreciation must go to Dr. Jason Day from Department of Earth Sciences, University of Cambridge for his help in the analyses with ICP-MS technique. I am very grateful to Prof. Peter Appleby for his help and advice in interpreting the obtained

results.

I am deeply indebted to The Libyan Embassy London-Cultural Affairs and Ministry of Higher Education for the financial support. I am also very grateful to the Nuclear Physics Group at the department of Physics, University of Liverpool for providing the various facilities for doing my research. Finally, I express my regards to all of those who supported me in any respect during the completion of my research journey.

Contents

1 Introduction **2**

1.1 Background 2

1.1.1 Radiation sources 2

1.1.2 The concept of radioactive disequilibrium 7

1.1.3 Development of methods for detection of radionuclides from U-series decay 9

1.2 Aims and Objectives of the Study 12

1.3 Research benefits and impact 14

2 Nuclear Decays and Radioactivity **16**

2.1 Radioactivity and Radioactive Decay 16

2.2 The radioactive decay law 18

2.3 Branched decay 21

2.4 Radioactive decay chains 22

2.4.1 The Bateman equations 25

2.5 Radioactive equilibrium 27

2.5.1 Secular equilibrium 27

2.5.2 Transient Equilibrium 30

2.5.3 No Equilibrium 31

3 Gamma-ray spectrometry technique **33**

3.1 Gamma-ray interactions in matter 33

3.1.1 Photoelectric effect 34

3.1.2 Compton scattering . . . 35
3.1.3 Pair production . . . 35
3.2 Gamma-ray interactions in a Ge spectrometer . . . 36
3.3 Gamma-ray spectrometer system . . . 38
3.3.1 Germanium and silicon crystals . . . 40
3.3.2 Detector and processing electronics . . . 42
3.3.3 Shielding . . . 45
3.3.4 Dewar and cryostat . . . 46

4 System calibration **47**
4.1 Energy calibration . . . 48
4.2 Resolution . . . 49
4.3 Efficiency calibration . . . 53
4.3.1 Experimental efficiency calibration . . . 55
4.3.2 Self-absorption corrections and low-energy efficiency . . . 59
4.3.3 Determination of the sample's chemical compositions . . . 62
4.3.4 Efficiency calibration with LabSOCS . . . 64
4.3.5 Density and elemental composition effects . . . 66
4.3.6 Thickness and diameter effects . . . 72
4.4 Validation of LabSOCS . . . 76
4.5 Conclusion . . . 81

5 Environmental aspects and activity determinations **82**
5.1 Sample collection and preparation . . . 82
5.2 Calculation of the minimum detectable level . . . 83
5.3 Background subtraction and nuclides identification . . . 87
5.4 Photopeak determination . . . 88
5.5 Activity calculations . . . 90
5.6 Uncertainty calculation . . . 90
5.7 Determination of ^{238}U and ^{232}Th . . . 91

5.8 Correction for ^{226}Ra from ^{235}U 94
5.8.1 Calculation of ^{238}U decay rate 94
5.8.2 Calculation of ^{235}U decay rate 95
5.8.3 Calculation of gamma fraction 95
5.9 Correction for coincidence summing 95

6 Results and discussion **98**
6.1 Specific activities of the radionuclides from the ^{238}U and ^{232}Th decay chains 98
6.2 Concentration of ^{238}U and ^{232}Th 106
6.3 Disequilibrium in the Uranium series 108
6.3.1 Possible origins of disequilibrium in sediment and soil samples . . . 108
6.3.2 Interpreting of the state of disequilibrium 109
6.4 Reliability of the method 113

7 Conclusions and Future Work **119**
7.1 Summary 119
7.2 Conclusion 121
7.3 Future Work 122

Appendices **123**

A **124**
A.1 Standard sources certificates 124
A.1.1 **N**PRL604 Marinelli Beaker 125
A.1.2 **I**AEA-375 Standard Material 126
A.1.3 **I**AEA-312 Standard Material 128
A.2 Samples specifications 130
A.3 Tables of Results for the activity calculations 132
A.4 The spectra of the measured samples 135
A.4.1 **S**tandard materials 135
A.4.2 **S**amples from Czech Republice 137

A.4.3 **S**ample from Germany 138
A.4.4 **S**amples from Australia 139
A.4.5 **S**amples from Namibia 140

List of Figures

2.1 The exponential radioactive decay curve for a radionuclide with 24 days half-life. 21

2.2 A diagram showing the decay scheme of the ^{40}K radionuclide (Edited from [59]). 22

2.3 Scheme of multiple decay similar to the natural decay chains. 23

2.4 The ^{238}U natural decay chain [1]. 24

2.5 The ^{232}Th natural decay chain [1]. 24

2.6 The ^{235}U natural decay chain [1]. 25

2.7 Growth of a short lived daughter ^{234}Th (24.1 d) from a much longer lived parent ^{238}U (4.5×10^9 y) until reaching Secular Equilibrium. 29

2.8 Growth and decay of a short lived daughter (^{230}Th) from a slightly longer lived parent (^{234}U) in Transient equilibrium. 31

2.9 A logarithmic plot of the growth and decay of a longer lived daughter from a short lived parent in case of no equilibrium. Np and Nd indicate the amount of parent and daughter nuclei, respectively. 32

3.1 The relative important of the three major type of gamma-ray interaction [59, 81]. 36

3.2 Interactions of gamma rays in a large detector and the resulting spectrum. Photoelectric, Compton and pair production interations are labeled as PE, CS and PP, respectively. 37

3.3 Interactions of gamma rays in a small detector and the resulting spectrum. Photoelectric, Compton and pair production interations are labeled as PE, CS and PP, respectively. 37

3.4 Interactions of gamma rays in a real detector and the resulting spectrum. Photoelectric, Compton and pair production interations are labeled as PE, CS and PP, respectively. 38
3.5 The ^{60}Co gamma-ray spectrum acquired from BEGe-2825 detector with the two characterised peaks labeled. 39
3.6 Band structure for electron energies in insulators and semiconductors modified from. 40
3.7 N-type semicondutor. 41
3.8 P-type semicondutor. 42
3.9 Main components of a system for gamma-ray spectroscopy. 43
3.10 The flow chart for the detection of gamma rays in a Germanium spectrometer. 44
3.11 Broad Energy Germanium Detector Dimisions [89]. 44
3.12 BEGe detector, shielding system and cryostat. 46

4.1 The energy calibration line for the BEGe-2825 detector. Regression coefficient is 1. 49
4.2 Full Width at Half Maximum [59]. 50
4.3 A plot of Full-Width Half-Maximum (FWHM) as a function of gamma-ray energy for a Broad-Energy Ge (BEGe) detector (a) and NaI(Tl) detector (b). 51
4.4 A plot of Full-Width Half-Maximum (FWHM) as a function of gamma-ray energy for a Broad-Energy Ge (BEGe) detector and Coaxial Ge detector of the same diameter. The same data presented in Table. 4.2 and Table. 4.3. . 52
4.5 A plot of the IAEA-375 standard source spectrum from the Broad-Energy Ge (BEGe) detector. 54
4.6 Experimental efficiency plots for BEGe detector from different standards (as described in the text). 58
4.7 The same as Fig. 4.6 using log log scales. 58
4.8 A schematic view of the measurement arrangment; D_1 the container diameter, D_2 the detector diameter, H_1 the container thickness and H_2 the sample thickness. Typical values are shown. 60

4.9 A plot for gamma-ray transition data presented in Table 4.6. 62
4.10 Planetary Ball Mill Instrument used to prepare the samples for XRF analysis. 63
4.11 The X-ray fluorescence system and some of the analysed samples. 64
4.12 Modelled efficiencies for one of the realistic samples (LV396) with varied density and constant thickness and chemical compositions. 67
4.13 Modelled efficiencies for one of the realistic samples (LV389) with varied density and constant thickness and chemical compositions.. 68
4.14 Modelled efficiencies with varied chemical compositions and constant thickness and density compared with LV396 sample (Table. 4.6), which is used for measurements in the present work. 70
4.15 Modelled efficiencies with varied chemical compositions and constant thickness and density compared with LV389 sample, which is used for measurements in the present work.. 71
4.16 Varying the efficiency with the sample thickness in the energy range from 46 -1000 keV. 72
4.17 Varying the efficiency with the sample thickness in the energy range from 46 - 300 keV for LV396 sample. 74
4.18 Varying the efficiency with the sample diameter in the energy range from 46 -1000 keV. 75
4.19 Modelled efficiency plots for two of the measured sample. 76
4.20 Measured and model efficiency data points from ^{210}Pb and ^{137}Cs from the calibrated source LDP1. 77
4.21 A comparison between experimental attenuation measurements normalised to modelled results for LV389 sample; the presented errors are due to the experimental results. 78
4.22 A comparison between experimental attenuation measurements normalised to modelled results for LV519 sample; the presented errors are due to the experimental results. 79

4.23 Modelled efficiency data points for standard material with different thicknesses (d1=10.04 cm, d2=10.22 cm and d3=11.25 cm) compared to measured effieincy (source base efficiency) [105]. 80

5.1 The locations of the four samples of LV519, LV520, LV521 and LV522 on the map of Australia. This map was created using Google Earth. 84
5.2 The locations of six samples that were found in disequilibrium on the map of Namibia in South Africa. This map was created using Google Earth. . . 84
5.3 The locations of four samples of LV389, LV390, LV391 and Nussi on the map of Czech Republic and south Germany in Europe. This map was created using Google Earth. 85
5.4 A prepared sample filling in a cylindrical container and sealed. 85
5.5 A background spectrum from BEGe detector for a time of 257697.6 s. The gamma-ray energies from uranium and thorium identified are labeled. . . . 88
5.6 Example of fitting the 92-93 keV energy region using Gf3 software. Left panel: typical spectrum before fitting. Right panel: the same spectrum showing fitted peak shapes. Numbers are labels of fits. 89
5.7 Selected paths in the decay scheme of ^{214}Bi to 0.768 MeV and 1.120 MeV gamma-ray emissions [120]. 97

6.1 Comparison of the results of the ^{234}Th specific activities using its peaks at 63.3 keV and 92.6 keV in the all measured samples. The line represents the 1 : 1 agreement. 100
6.2 ^{214}Pb and ^{226}Ra diagram of samples. The equilibrium line is displayed. . . 101
6.3 ^{214}Bi and ^{226}Ra diagram of samples. The equilibrium line is displayed. . . . 102
6.4 ^{214}Bi and ^{226}Ra diagram of samples. The equilibrium line is displayed. . . . 103
6.5 ^{228}Ac and ^{212}Pb diagram of samples. The equilibrium line is displayed. . . . 105
6.6 ^{228}Ac and ^{208}Tl diagram of samples. The equilibrium line is displayed. . . . 106

6.7 ^{226}Ra and ^{234}Th diagram for all the measured samples. The equilibrium line is displayed. ^{226}Ra varied in the six samples from Namibia (open circle pattern). These data are indicated in Table 6.1. 111

6.8 The variation of ^{234}Th and ^{226}Ra in samples that were found in equilibrium as indicated in Table 6.1. The numbers of 1, 2, 3, 4, 5 and 6 on X-axis refer to the samples ID of LV393, LV395, LV396, LV398, LV523 and LV524, respectively. 112

6.9 The variation of ^{234}Th and ^{226}Ra in non-equilibrium data as discussed above and shown in Table 6.1. The numbers of 1, 2, 3, 4, 5, 6, 7 and 8 on X-axis refer to the samples ID of LV519, LV520, LV521, LV522, LV389, LV390, LV391 and Nussi, respectively. 114

6.10 Comparison between the ^{238}U concentrations determined by gamma-ray spectrometry (BEGe detector) and ICP-MS system. 115

6.11 Comparison between the ^{232}Th concentrations determined by gamma-ray spectrometry (BEGe detector) and ICP-MS system. 116

List of Tables

1.1 The Uranium series [6, 7]. 4

1.2 The Thorium series [6, 7]. 5

1.3 The Actinium series [6, 7]. 6

1.4 The most significant gamma-ray emitting radionuclides in the natural decay series [7]. 8

3.1 Specification of the system used. 45

4.1 Decay data for radionuclides in the NPRL-604 Marinelli source used in the energy calibration. The gamma-ray energies and channel numbers measured after the calibration are shown to the right-hand side of the vertical line. . . 48

4.2 Data for FWHM against gamma-ray energy for BEGe detector. 53

4.3 Data for FWHM against gamma-ray energy for Coaxial detector. 53

4.4 Radionuclides, activties and geometries used for comparing the experimental detection efficiency; [1] recommended values obtained from the reference sheet for the material(IAEA, 2000) with 95% Confidence interval of 15.7-17.4 and 81.3-101.5 for ^{238}U and ^{232}Th, respectively. 57

4.5 List of sources and their gamma-ray energies used to correct for samples attenuation. 60

4.6 Gamma-ray transitions (I/I_0) for set of samples with different chemical compositions, densities and thickness for different photon energies. 61

4.7 The chemical compositions for the samples from Namibia. 64

4.8 The chemical compositions for the samples from Australia. 65

4.9 The chemical compositions for the samples from Czech Republic. 65
4.10 Chemical compositions (%) for LabSOCS default material used in Fig. **??** and Fig. 4.14. 69
4.11 Parameters in bold entered to LabSOCS for uncertainty estimates. 73
4.12 Recommended uncertainties for LabSOCS efficiencies [103]. 75
4.13 Modelled and measured efficiency for 46.5 keV and 662 keV gamma energies from LDP1 standard source described in Table 4.4. Uncertainty on the model is based on the variation results discussed above. 78

5.1 MDA (Bq) of radionuclides in based on one of the analysed samples (LV389) for a counting time of one week (604800 s). 86
5.2 Gamma-ray energy from uranium and thourium decay series and associated uncertainty on their gamma-ray emissions [7]. 92
5.3 Gamma-ray energies and associated emission probability per decay used for activity concentration determination; [1] The emission probability is the sum of the double gamma-ray at 62.9 keV and 63.3 keV (0.016, 3.7), [2] the emission probability is the sum of the double gamma-ray at 92.4 keV and 92.8 keV (2.13, 2.10), [3] the gamma-ray emissions corrected for the fraction of beta emission to ^{212}Po nuclide (64.1%). 93

6.1 Specific activities of the relevant radionuclides from ^{238}U decay series. . . . 99
6.2 Specific activities of the relevant radionuclides from ^{232}Th decay series. . . . 104
6.3 The elemental concentrations of uranium and thorium in all the measured samples. 107
6.4 The activity ratio of ^{226}Ra to ^{238}U (^{234}Th) in all the measured samples. . . 113
6.5 ^{238}U and ^{232}Th concentrations (ppm) from two independent techniques; [1]using BEGe detector, [2]using ICP-MS system. 115
6.6 ^{238}U, ^{232}Th and ^{226}Ra concentrations (ppm) for IAEA-312 standard material from gamma spectrometry using BEGe detector and data presented in the reference sheet in Appendix A (A.1.3). 116

6.7 A comparison for concentrations of ^{238}U and ^{232}Th from Nussi sample obtained using different gamma-ray spectrometry systems; * Ge detector, • neutron activation analysis. Details about the results presented in this Table can be obtained by a personal communication with Babara Mauz. . . . 117

6.8 ^{234}Th and ^{210}Pb activities (Bq/kg) from two germanium detectors; * details about the results from this detector can be obtained by a personal communication with Babara Mauz. . . . 118

A.1 Samples description; ; [1] poorly means different range of grain sizes, [2] well means that the grain sizes are all consistent. . . . 131

A.2 Namibia samples. . . . 133

A.3 Australia samples. . . . 134

A.4 Nussi and samples from Czech Republic. . . . 134

Chapter 1

Introduction

1.1 Background

1.1.1 Radiation sources

Naturally occurring radionuclides arising from cosmic and terrestrial sources are the main sources of environmental radiation. Cosmic radiation reaches the Earth from interplanetary space and from the Sun [1, 2]. They are classified into primary cosmic rays, which are stable charged particles and nuclei accelerated at astrophysical sources, and secondary cosmic rays are particles produced via the interaction of the primaries with the elements they encounter in the atmosphere [1]. The accelerated primary cosmic rays induce nuclear reactions in the atmosphere, which may produce radioactive isotopes [3, 4, 5]. In addition, showers of electrons and mesons are produced by these interactions [3, 4, 5]. ^{7}Be, ^{22}Na, ^{38}S, ^{38}Cl and ^{26}Al are examples for naturally occurring radionuclides that are gamma-ray emitters and produced by cosmic-rays [1, 6, 7]

Terrestrial gamma radiation gives rise to more than 80% of the total dose of ionising radiation to which the population is exposed [8]. Terrestrial radionuclides can be found as singly occurring radionuclides and nuclides that are members of the three main decay chains (^{238}U, ^{235}U and ^{232}Th). Singly occurring radionuclides decay into a stable product. ^{40}K is an example of a singly occurring radionuclide, which decays either into ^{40}Ca by β-emission or into an excited state of ^{40}Ar by electron capture. The ^{40}Ar excited state decays

very quickly to the ground state following the emission of a 1460 keV γ ray. The natural radioactive decay series comprise three long chains that originate from ^{238}U, ^{235}U and ^{232}Th. Uranium and thorium and their decay products are the primary sources of natural radioactivity in the environment. These nuclides are found in most types of soil and rocks, and their concentration in the latter is dependent on their formation process. For example, granite contains higher concentrations of elements from the decay series radionuclides than sandstone and limestones rocks [3, 4] due to their production in volcanic processes that convey material from the Earth's mantle. It is also believed to be influenced by processes related to the pre-existing continental crust and the fractional crystallisation where crystals are removed from magma as they form [9, 10]. For this reason, igneous rocks of granitic composition are strongly enriched in uranium and thorium (on an average 5 ppm of U and 15 ppm of Th), compared with the Earth's crust (average 1.8 ppm for U and 7.2 ppm for Th), the upper continental crust (average 2.7 ppm for U and 10.5 ppm for Th) [10, 11].

The parent radionuclides in these series are primordial in origin because they are so long lived since they still exist some 4.5 billion years after the solar system was formed [12, 4]. The main radioisotopes, half-lives and principal radiations from ^{238}U, ^{232}Th and ^{235}U are shown in Tables. 1.1, 1.2 and 1.3, respectively [13].

Table 1.1: The Uranium series [6, 7].

Isotope	Half-life	Radiation	Energies (MeV)	Yield (%)
^{238}U	4.5 x 10^9 y	α	4.19, 4.15	79, 21
		γ	0.049	0.064
^{234}Th	24.1 d	β	0.199, 0.107	78, 14
		γ	0.063, 0.092	3.7, 4.23
^{234m}Pa	6.7 h	β	2.27	98
		γ	1.001	0.84
^{234}U	2.5 x 10^5 y	α	4.77, 4.72	71, 28
^{230}Th	8 x 10^4 y	γ	4.68, 4.61	76, 23
^{226}Ra	1600 y	α	4.78, 4.60	94, 6
		γ	0.186	3.6
^{222}Rn	3.8 d	α	5.49	100
^{218}Po	3.1 m	α	6.0	100
^{218}At	1.5 s	α	6.7, 6.8	89, 4
^{214}Pb	26.8 m	β	0.67, 0.72, 1.02	46, 40, 11
		γ	0.352, 0.295, 0.242	36, 18, 7
^{214}Bi	20 m	β	3.27, 1.54, 1.50	19, 18, 17
		γ	0.609, 1.76, 1.12	15.3, 14.9, 45
^{214}Po	1.6 x 10^{-6} s	α	7.68	100
^{210}Tl	1.3 m	β	1.86	24
		γ	0.79	98
^{210}Pb	22 y	γ	0.046	4.25
		β	0.017, 0.063	84, 16
^{210}Bi	5.0 d	γ	0.27, 0.30	51, 28
		α	4.95, 4.91	55. 40
^{210}Po	138 d	α	5.3	100
^{206}Pb	stable	-	-	-

Table 1.2: The Thorium series [6, 7].

Isotope	Half-life	Radiation	Energies (MeV)	Yield (%)
^{232}Th	14 x 10^{9} y	α	4.01, 3.95	78, 22
		γ	0.064	0.26
^{228}Ra	5.8 y	β	0.039, 0.025	40, 20
^{228}Ac	6.15 h	β	1.17, 2.08	30, 7
		γ	0.911, 0.969, 0.338, 0.328	26, 16, 11, 3
^{228}Th	1.9 y	α	5.42, 5.34	72, 27
^{224}Ra	3.66 d	α	45.42, 5.34	95, 5
		γ	0.24	4.1
^{220}Rn	56 s	α	6.29	>99
^{216}Po	15 x 10^{-2} s	α	6.78	100
^{212}Pb	10.64 h	β	0.331, 570	100
		γ	0.239, 0.300	43.6, 3.30
^{212}Bi	60.6 m	α	6.05, 6.90	25, 10
		β	2.25	55
		γ	0.727	7
^{212}Po	3 x 10^{-7} s	α	8.78	100
		γ	2.61	3
^{208}Tl	3.1 m	β	1.80, 1.29, 1.52	49, 24, 22
		γ	2.614, 0.583, 0.510, 0.861	99.8, 85, 23, 13
^{208}Pb	stable	-	-	-

Table 1.3: The Actinium series [6, 7].

Isotope	Half-life	Radiation	Energies (MeV)	Yield (%)
^{235}U	7 x 10^8 y	α	4.40, 4.36, 4.2, 4.6	58, 19, 6, 5
		γ	0.185, 0.143, 0.163, 0.205	57, 11, 5, 5
^{231}Th	25.5 h	β	0.30, 0.31, 0.29	40, 32, 12
		γ	0.027, 0.302	10, 2.2
^{231}Pa	3.3 x 10^4 y	α	5.01, 4.95, 5.03, 5.06	25, 23, 20, 11
		γ	0.027, 0.29	6, 6
^{227}Ac	21.8 y	α	4.94	0.55
^{227}Th	18.7 d	α	6.04, 5.98, 5.76, 5.71	24, 24, 20, 8
		γ	0.24, 0.26	13, 7
^{223}Fr	22 m	β	1.10, 1.07, 0.91	70, 15, 10
		γ	0.05	34
^{223}Ra	11.4 d	α	5.72, 5.61	52, 25
		γ	0.27, 0.32, 0.34	14, 4, 3
^{219}Rn	4.0 s	α	6.82, 6.55, 6.42	80, 13, 8
		γ	0.271, 0.402	11, 7
^{215}Po	1.78 x 10^{-3} s	α	7.39	100
^{215}At	10^{-5} s	α	8.03	100
^{211}Pb	36 m	β	1.37	91
		γ	0.40	4
^{211}Bi	2.14 m	α	6.62, 6.28	84, 16
		γ	0.351	13
^{207}Tl	4.77 m	β	1.42	>99
^{207}Pb	stable	-	-	-

1.1.2 The concept of radioactive disequilibrium

The transformation of the long-lived primary radionuclides into stable elements involves a complex series of radioactive decays with different half-lives and, in some cases, chemical properties. In any geological undisturbed sample, all members are in secular equilibrium, which means that the activity of disintegrating atoms per unit time is identical for all members in the respective series [14]. However, if natural processes in the environment such as mobilization of soluble elements or precipitation of minerals in an aquatic environment cause chemical fractionation between the different elements (U, Th, Ra), the decay series are set into a state of radioactive disequilibrium [14]. This fractionation allows radionuclides in the decay series to be used as a dating tool for many geological processes. In other words, the existence of disequilibrium in sediments is the signature of past or still active geological processes that affect radiochemical composition of the sample and its surroundings [15]. A comprehensive review for several types of dating using U-series radionuclides can be found in Ivanovich and Harmon [14].

Investigation of the state of secular equilibrium in a particular environmental system requires the quantitative identification and measurement of radionuclides from U-series and other decay. This can be achieved using gamma-ray spectrometry to measure the intensity of the gamma-emitting radionuclides in the decay series within a sample. Therefore, it is essential to know the radionuclides with sizeable gamma-ray branches that can be detected using high-resolution HPGe detectors. Table 1.4 lists the most significant gamma-emitting radionuclides that can be detected in the uranium and thorium decay series.

Table 1.4: The most significant gamma-ray emitting radionuclides in the natural decay series [7].

Radionuclide	Half-life	γ-energies (keV)	Yield (%)
	^{238}U decay series		
^{234}Th	24.1 d	62.9, 63.3	0.02, 3.7
		92.4, 92.8	2.1, 2.1
^{234m}Pa	6.7 h	766.4	0.32
		1001.0	0.84
^{226}Ra	1600 y	186.2	3.6
^{214}Pb	26.8 m	242.0	7.3
		295.2	18.4
		352.0	35.6
^{214}Bi	20 m	609.3	45.5
		1120.3	14.9
		1238.1	5.8
		1764.5	15.3
^{210}Pb	22 y	46.5	4.2
	^{232}Th decay series		
^{228}Ac	6.15 h	209.3	3.9
		338.3	11.3
		911.2	25.8
		969.0	15.8
^{212}Pb	10.6 h	238.6	43.6
		300.1	3.3
^{212}Bi	60.6 m	727.3	6.7
^{208}Tl	3.1 m	583.2	85.0
		860.6	12.5
		2614.5	99.8
	^{235}U decay series		
^{235}U	7 x 10^8 y	185.7	57.0
		143.8	11.0
		163.4	5.1
		205.3	5.0
^{231}Pa	3.3 x 10^4 y	300.2, 302.7	2.4, 2.3

1.1.3 Development of methods for detection of radionuclides from U-series decay

Despite the fact that disequilibrium in U-series decay is one of the powerful tools and chronometers of weathering processes, the improvements of analytical techniques have been slow as a result of complications in accurately measuring U-series radionuclides [12]. U-series nuclides in geological samples have been measured using either direct or indirect techniques over several decades. These methods include counting methods, i.e. alpha, beta and gamma spectrometry and mass spectrometry based on, for example, thermal ionization mass spectrometry (TIMS), inductively coupled plasma mass spectrometry (ICP-MS), fast source mass spectrometry and accelerator mass spectrometry. Among all these methods, only gamma-ray spectrometry does not require complicated and long preparations for the source being measured.

The Thermal Ionisation Mass Spectrometric (TIMS) measurement was initially applied in the past decade for long-lived uranium-series nuclides [16, 17]. This technique allows sensitive precision measurements, which have been developed for several applications in uranium-series geochronology and geochemistry of young sediments and rocks. This led to the invention of advanced thermal ionisation techniques such as Inductivity Coupled Plasma Mass Spectrometry (ICP-MS), which started to be utilised by archaeologists in the early, or mid-1990s [16, 17]. However the negative aspect of this technique is that the processing of samples, for example, digestion of soil [18] is time-consuming and dedicated laboratory equipment is required [17].

The Alpha spectrometric technique is a method of choice for the analysis of radioisotopes [19], however, it requires long processes for analysis preparations such as the separation of radionuclides [18] and has strict requirements for the source under analysis. For instance, the source has to be thin, massless and smaller in area than the active area of the detector [1]. The results of the analysis will be unreliable if these conditions are not considered. This necessity for the source preparation makes the alpha spectrometry technique time consuming for analysing environmental samples.

Marie Sklodowska Curie was the first scientist who studied the natural radioactivity

following the discovery of this phenomenon by Becquerel in 1896 [20]. Many chemists, geologists, and physicists then followed this study by a comprehensive research on the natural radioactivity of rocks, minerals, natural waters, and the atmosphere. They used different experimental methods such as photographic plate, electroscope, electrometer, and ionization chambers [20, 21]. The Geiger-Muller tube was developed in 1908 and first adapted for use in 1932 by Shrum and Smith [22]. In 1944, Curran and Baker developed scintillation counters based on sensitive photomultiplier tubes. Krebs first introduced this counter in 1941, based on a photosensitive Geiger-Muller counter [23]. This was followed by an intensive development for scintillation materials started after the discovery of NaI(Tl) for gamma-ray detection by Robert Hofstadter in late 1940s [24].

Mass spectrometry (MS) is another significant method for decay series measurements and has a high degree of sensitivity. The use of this technique for measuring isotopic abundances was first demonstrated in 1919 by Francis William Aston[25]. The two widely used mass spectrometry methods for the analysis of uranium are inductively coupled plasma mass spectrometry (ICP-MS) and isotope ratio mass spectrometry (IR-MS) [26, 27]. However, the requirements for multi-step sample preparation prior to ICP-MS experiments make this a difficult, expensive and time consuming technique. The sample pre-treatment procedures may decrease detection sensitivity and introduce chemical impurities. This approach gives accurate results, but it is time consuming, lengthy and costly. Furthermore, most of the techniques considered to be very precise and accurate such as ICP-MS, determine only parent nuclide concentrations [28, 29]. Therefore, it is difficult to examine the equilibrium condition completely in either the ^{238}U or ^{232}Th decay chains. For these reasons, it is necessary to develop a new approach for uranium determination by gamma-ray spectrometry, which also reduces treatment and disposal costs incurred using other techniques.

Scintillation gamma spectroscopy was one of the widely used techniques to quantify U-series radionuclides in the 1990s [30]. Some researchers measured the high-energy gamma rays using this technique. For example, gamma emissions from the ^{214}Bi radionuclide from the ^{238}U decay series [30, 31]. Other researchers used to it to measure the geological

uranium based on its low-energy gamma emissions from ^{210}Pb and ^{226}Ra [30, 32]. However, these detectors are limited by poor energy resolution and the separation of gamma emissions in the spectra, that are often close in transition energy, is difficult or impossible.

Several researchers used a combination of different methods to quantify disequilibrium in U-series decay. For instance, high-resolution gamma and alpha-particle spectrometry enabled the present-day equilibrium state of the decay chains to be fully assessed [28, 29, 33]. For example, the combination of alpha and gamma spectrometry enabled the investigation of the level of disequilibrium in U-series decay [28, 34]. The concentration of uranium and thorium and their daughters were also determined using the combination of inductively coupled plasma mass spectrometry (ICP-MS) and gamma-spectroscopy, for example [29].

In several recent studies, an indirect determination for ^{238}U from its daughters ^{214}Bi and ^{214}Pb is the method of choice [35]. However, these radionuclides are controlled by their parent ^{226}Ra, which is in turn dependent on the gaseous radionuclide of ^{222}Rn as will be explained later in this thesis. In addition, this method is based on the assumption that equilibrium is established between ^{238}U and its daughters ^{214}Bi and ^{214}Pb, which has a limitation with reporting many cases of disequilibrium in natural systems [36, 37].

The use of ^{234}Th to determine it parent ^{238}U was established since 1970s. For example, some researchers used this procedure to quantify the parent of ^{238}U from its daughter ^{234}Th using the peak 63.3 keV [38, 39]. This was followed by using the second peak of 92.8 keV from ^{234}Th [40, 41]. However, correction for self-absorption effects has been a constant challenge with using these low energy gamma rays . In contrast, using this daughter with short half-life (24.1 d) compared to the long-lived parent ^{238}U eliminates the inaccuracy due to disequilibrium conditions in the uranium decay series, which is achieved quickly. Therefore, many researchers introduced different procedures to correct for this effect [42, 43, 44]. The use of 766.4 and 1001 keV peaks from ^{234m}Pa daughter to determine ^{238}U has also been the preferred method proposed by several researchers [45, 46, 47, 48]. Although these peaks are negligibly affected by self-absorption, a comparison was carried out [46], showed that the results obtained with ^{234}Th were 25 and 12 times accurate than

those from 766.4 and 1001 keV, respectively. Furthermore, the overlap of 766.4 keV gamma ray with 768.7 keV ^{214}Bi peak (4.89%) makes it undesirable for uranium analysis [46]

Semiconductor detectors have become the method of choice for determination of nuclear radiation using gamma spectrometry due to short time required for measurements, relative simplicity, lower cost and lack of complicated sample preparation. The most significant feature of gamma spectrometry is the applicability to analyze bulk samples that usually require little, or no, radiochemical preparation. For instance, soils and sediments can often be directly placed into the container after only very basic preparation (e.g. drying, sieving etc.).

One of the favourable semiconductors detectors used for measuring the environmental samples is the high purity germanium detector (HPGe) [49]. This detector type has been used to determine naturally occurring radioisotopes for several purposes including the assessment of the level of radioactivity [35, 50, 51, 52] and the study of disequilibrium in U-series decay and dating applications [28, 34, 53, 54]. The application of this technique used for the measurement of radionuclides from U-series decay presented in this thesis. The importance of this non-destructive technique requires extensive developments in the methods for better performance and precision analysis.

1.2 Aims and Objectives of the Study

The precision and accuracy of measurements of natural sources of radiation depends on the method of measurement. Development of the present technique is aimed at enhancing this accuracy. The measurement of natural radioactivity; particularly the radioisotopes from the natural decay series of uranium and thorium requires the analysis of environmental samples. It seeks to determine the elemental and/or activity concentrations for the radionuclides being investigated. Thus quantifying radioactive equilibrium in these decay chains. The following aspects are in this work are:

- The conventional procedure to determine the activity of radionuclides from the uranium decay series is largely dependent on using reference material or standard calibration samples; particularly when using gamma-ray spectrometry for analysis.

These standards have to be in a similar matrix and geometry to the investigated samples. This can be difficult to obtain for some samples under investigation. A crucial part of the current efficiency calibration procedure is using the modelling LabSOCS software (Laboratory Sourceless Object Calibration Software), the results of which are validated experimentally. Using a standard Broad Energy Germanium (BEGe) detector with a superior energy resolution at low gamma-ray energy is another important aspect of the present research. This is important for low energy gamma rays as it results in an improved peak height to background.

- In the present work the variation of the sample's parameters; the thickness, the diameter, the density and the chemical compositions and their influences on the detection efficiency are discussed in detail. The conventional method of the efficiency calibration using standard material is also outlined to some extent for the purpose of validating both the detector's characterisation and the method followed for determination of the detection efficiency using LabSOCS software.

- In the uranium series decay, disequilibrium originates as a result of disturbing the system by the fractionation of some of the daughter nuclei. Quantifying disequilibrium is attained by determining the activity concentrations for the radionuclides for which equilibrium is established quickly with the parent and those later in the decay chain where interruption can take place. This research is intended to quantify the first daughter radionuclide ^{234}Th, where equilibrium is established very quickly because of its half-life (24.1 days). This radionuclide has been previously used in several studies. However, the present procedure will solve a difficult aspect associated with it as the gamma rays emitted are low energy. The sample self-absorption is a challenge with such a low energy emitting nuclide.

- In the present work the decay series of ^{238}U was found in disequilibrium in some of the measured samples, whereas ^{232}Th was found in equilibrium in all of them.

- Finally, a major aspect to be addressed in this study is the practical validation of the results from the proposed methods using independent techniques, which will confirm

the accuracy of determining the activity concentrations for radionuclides and thus quantifying disequilibrium in uranium decay series.

1.3 Research benefits and impact

- Research into the behaviour of radionuclides is necessary to understand and predict the migration of contaminant actinides and related species [16]. The results in the present study can be used as a baseline for the level of radionuclides from U-series decay in the investigated regions.

- The study of the isotopic compositions for radionuclides from U-series decay can generate considerable information regarding radionuclide water-rock interactions and weathering release rates. For example the alkaline earth radium, and to greater extent the less soluble actinide thorium, are quickly removed from groundwater by water-rock interactions, and so are strongly depleted. Both of these elements have very long-lived isotopes, and so their isotope compositions reflect processes over a range of time scales [14, 16]. The results in the present study can be used as a guideline for the observation of any possible environmental processes.

- The measurement of radionuclides from U-series decay and hence quantifying possible disequilibrium can be used as a powerful tool for dating some environmental samples. However, this research is not intended to discuss any of theses dating methods.

The rest of this thesis is divided into five chapters. The second chapter gives a general idea about the nuclear decays and radioactivity followed a brief discussion about the cases of radioactive equilibrium with some examples for radioactive nuclides. The third chapter is focusing more on gamma-ray spectrometry technique by discussing the interactions by which gamma rays are detected in matter and giving a general idea about the detector and its different features. It also discusses in detail the method that has been for the system calibration. The fourth chapter presents the environmental aspects for the sample collection and preparation and the methods that have been applied for the experimental

measurements and the activity determinations followed by some procedures that were used to validate the method. In the fifth chapter, the results obtained by analysing the samples are presented and discussed. The final chapter presents the conclusion with a suggestion of future work.

Chapter 2

Nuclear Decays and Radioactivity

This chapter introduces the background of the radioactivity and radioactive decay. This includes different types of radioactive decay, radioactive decay chains and radioactive equilibrium. The radioactive decay law is also covered in this chapter with the relevant equations for each type of radioactive equilibrium extracted from the Bateman solutions.

2.1 Radioactivity and Radioactive Decay

The study of radioactive substances has brought significant information on the structure of the heavier elements such as uranium and thorium. For example, decay spectroscopy has revealed that these elements are unstable and undergo spontaneous decays by the emission of alpha- and beta-particles [55].

The radioactive decay is a random process by which an unstable parent nuclide is transformed into a more stable daughter nucleus. In the case where the daughter nucleus is unstable subsequent decays proceed as a chain until the line of stability is reached [55, 56, 57, 58].

There are several types of radioactive decay modes such as alpha, beta and nucleon emission and further electromagnetic de-excitations such as gamma emission and internal conversion [1]. However only alpha, beta and gamma emissions will be discussed here.

Alpha decay

Alpha particles symbolized with α, are composed of two protons and two neutrons and constitute the ^{4}He nuclide [56, 59]. There are many alpha-decaying radioisotopes that are either naturally occurring such as ^{238}U and ^{232}Th or artificially synthesised such as ^{241}Am [59]. The emission of alpha particles from initial nucleus results in the reduction of both the mass and charge on the final product as indicated in the following schematic decay process [59, 60].

$$ {}^{A}_{Z}X \rightarrow {}^{A-4}_{Z-2}He + \alpha \tag{2.1} $$

The difference in mass energy between the parent and daughter nuclei releases energy in decay (the Q value) [56]. The energy released is shared between the alpha particles and the recoil nucleus and can be calculated according to the following equation [56, 59]

$$ Q = (m_p - m_D - m_\alpha)c^2 = E_D + E_\alpha, \tag{2.2} $$

where m_p, m_D and m_α are the masses of the parent, daughter and alpha particle, respectively, and E_D and E_α are the kinetic energies of daughter and alpha particle, respectively. More details about the alpha particles process may be found in [61, 62, 63].

Beta decay

Beta particles originate from the radioactive decay of certain neutron-rich or proton-rich unstable nuclei [56]. The beta particle is symbolized with β and corresponds to an electron orginating from this decay process. These particles can be either positive (positron, e^{+}) and result in the reduction of charge on the emitted nucleus or negative β (electron, e^{-}), which increases the charge on the emitted nucleus [56]. In radiation measurement, beta particles are the most common source of fast electrons [59]. The following schematic decay process indicates the emission of negative and positive beta particles, respectively [1, 56, 59].

$$^{A}_{Z}X \rightarrow ^{A}_{Z+1}Y + \beta^{-} + \overline{\nu}, \tag{2.3}$$

$$^{A}_{Z}X \rightarrow ^{A}_{Z-1}Y + \beta^{+} + \nu, \tag{2.4}$$

where X and Y the initial and final nucleus, respectively and $\overline{\nu}$ and ν are the antineutrino and neutrino, respectively.

As can be seen above, the first process involves the transformation of a neutron into proton whereas in β^{+} decay the proton is transformed into neutron. There is another process, that can take place alternatively to the emission of β^{+}, which is called electron capture (EC) [56].

Gamma emission

The emission of gamma radiation differs from alpha and beta decay since it is not a mode of radioactive decay. It is an electromagnetic process by which excess energy is dissipated from radionuclides in an excited state [1]. This state of excitation occurs often after the emission of alpha or beta particles [1, 56, 59]. Gamma rays are similar to X-rays in its nature (photons of electromagnetic radiation) however, they differ in terms of their origin [64]. Typically, the energy of gamma rays covers the range from 0.1 up to 10 MeV [56, 57]. There are several common sources for gamma rays that are used as calibration references. For example, ^{137}Cs (0.662 MeV), ^{22}Na (1.274 MeV), ^{60}Co (1.173 and 1.332 MeV) and many more [1]. More discussion about gamma decay and the interaction of gamma with matter will be detailed in later sections within this thesis.

2.2 The radioactive decay law

The radioactive decay is a statistical process and it cannot be predicted when any given nucleus will decay [57]. The average rate of radioactive decay or activity can be expressed

as [57]

$$A = \frac{dN}{dt} = -\lambda N, \tag{2.5}$$

where, N is the the number of radioactive nuclei at time t and λ is the decay constant defined as [57]

$$\lambda = \frac{ln(2)}{t_{1/2}}, \tag{2.6}$$

where $t_{1/2}$ the half-life of radioactive atom. The negative sign in Equation 2.5 indicates that the number of radioactive nuclei decreases as a function of time. This law of decay is applied to all radioactive nuclei but the decay constant is specified for each radionuclide [55, 58]. This indicates the basic assumption of radioactive decay theory, in which the probability per unit time is constant regardless of the age of the atoms. The exponential law of radioactive decay can be obtained by separating the variables of Equation 2.5 and integrating [57].

$$N(t) = N_0 e^{-\lambda t}, \tag{2.7}$$

where N_0 the number of atoms present initially at $t = 0$ and N is the number of atoms remaining after a time t [55, 58]. Assuming that the activity, i.e. disintegration per unit of time, of a radioactive product is A, equation 2.7 can be expressed in a different way as follows

$$A(t) = A_0 e^{-\lambda t}. \tag{2.8}$$

It is very common to measure the half-life $t_{1/2}$ to extract the decay constant (λ) for the decay rate of a specific radioactive nuclide. The half-life is defined by the time required for one half of the initial number of radioactive substance to decay. Thus by assuming $N = \frac{N_0}{2}$ in Eq. 2.7, the half-life is given by

$$t_{1/2} = \frac{ln(2)}{\lambda} = \frac{0.693}{\lambda}. \tag{2.9}$$

The decay constant λ can also be considered in terms of the mean lifetime, which is the sum of the lifetimes of a number of nuclei (before they have all decayed out) divided

by the number of nuclei [16], using the following equation

$$\tau = \frac{1}{\lambda} \tag{2.10}$$

Thus, the mean lifetime τ can be expressed in terms of the half-life by substituting Eq. 2.9 in Eq. 2.10.

$$\tau = \frac{t_{(1/2)}}{0.693}. \tag{2.11}$$

The Curie, assigned by Ci, is the original unit of activity, which is equal to 3.7 x 10^{10} decays per second, based on the activity of 1 gram of Radium (^{226}Ra). However, the current standard unit is Becquerel (Bq) in honour of Henri Becquerel who discovered the radioactivity of uranium in 1896 [1]. The prefixes kBq, MBq, GBq and TBq are often used because Bq is a very small unit for many purposes [55, 58, 65, 66]. The rate of radioactive decay varies even if the amounts of radioactive material are the same. For instance, equal amounts from radium and uranium will give different radiation per unit time [65]. There is another quantity that expresses the concentration of radioactivity which is known as a specific activity, which measures the activity per unit mass or volume of the transformed radioactive material. The Becquerel and Curie does not signify anything about this quantity, therefore the specific activity is measured by Becquerel or Curie per unit mass or volume [66]

An example of the radioactive decay law has been applied on an arbitrary radionuclide as shown in Fig. 2.1. The value of λ is taken as 2.88×10^{-2} days^{-1} corresponding to the half-life of 24 days. The curve represents the activity of the radionuclide A at any time and the value of initial number of A is taken as 1. After interval time of several days the amount of A decreases according to an exponential law with the time falling to half value in 24 days.

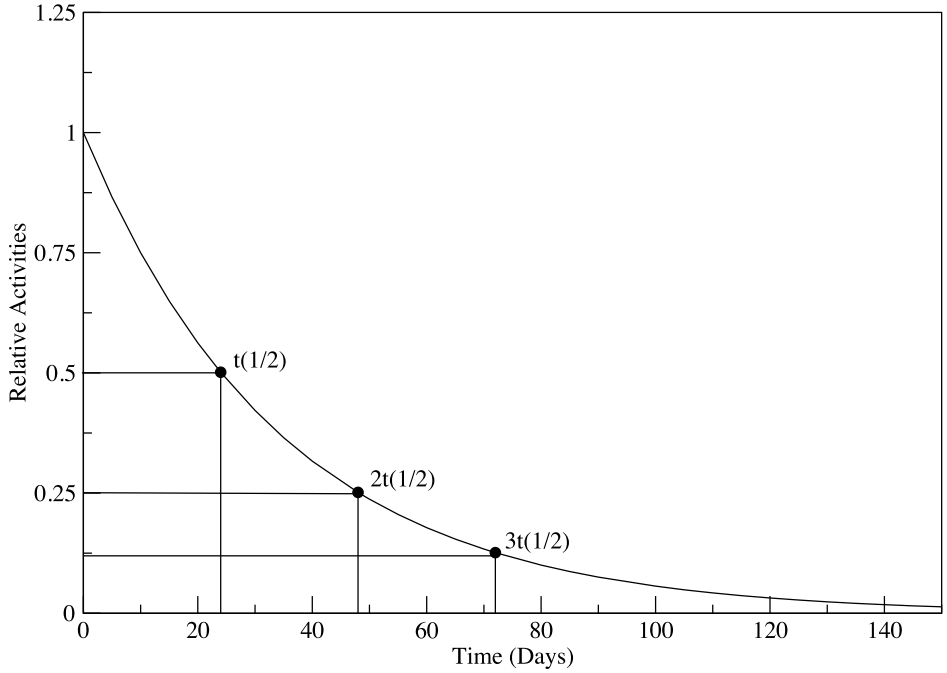

Figure 2.1: The exponential radioactive decay curve for a radionuclide with 24 days half-life.

2.3 Branched decay

In some cases, the parent nuclide may decay to more than one daughter nuclide. This mode of disintegration is named a branching decay [57, 60]. In this decay type each branching is assigned by a characterised partial decay constant, which can be determined for each decay, based on the half-life, by multiplying the total observed decay constant by the fraction of parent decay corresponding to that branch [60]. For example, the radionuclide ^{40}K, shown in Fig. 2.2, decays to two stable nuclei, ^{40}Ar by electron capture and ^{40}Ca by β-emission with branching ratios of 10.7% and 89.3%, respectively [1, 7]. The observed total decay constant is equal to 5.6 $\times 10^{-10}$ yr^{-1} based on the half-life of 1.25 $\times 10^{9}$ yr for ^{40}K. The partial constants are:

$$\lambda_{EC} = 0.107 \times 5.6 \times 10^{-10} = 5.93 \times 10^{-11}\ yr^{-1}, \tag{2.12}$$

$$\lambda_\beta = 0.893 \times 5.6 \times 10^{-10} = 4.95 \times 10^{-10}\ yr^{-1}, \tag{2.13}$$

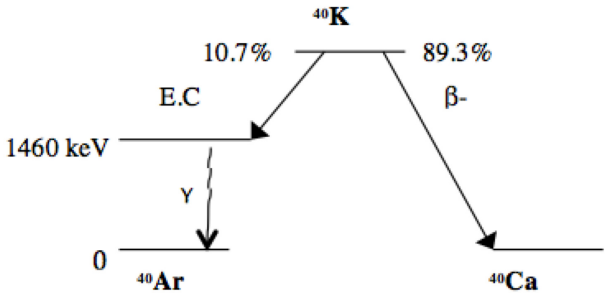

Figure 2.2: A diagram showing the decay scheme of the ^{40}K radionuclide (Edited from [59]).

The decay constants for ^{40}Ar and ^{40}Ca are 5.93 $\times 10^{-11}$ yr^{-1} and 4.95 $\times 10^{-10}$ yr^{-1}, respectively. Accordingly, the partial half-lives of 1.17 $\times 10^{10}$ yr for electron capture decay and 1.40 $\times 10^{9}$ yr for β-emission and the total observed decay constant, λ_K, is equal to the sum of the partial decay constants [1, 60] according to the equation

$$\lambda_k = \lambda_{Ar} + \lambda_{Ca}. \tag{2.14}$$

2.4 Radioactive decay chains

There are many cases by which radioactive nuclei decay towards the line of stability through a multistep decay chain [56, 57, 65, 67]. There are four naturally occurring radioactive decay series, which are named in terms of their original parent source, Uranium (^{238}U), Thorium (^{232}Th), Actinium (^{235}U) and the artificial Neptunium (^{237}Np). However, the three naturally occurring (U, Th and Ac) are still in existence because of their long half-lives while the half-life of the Np parent is 2.2 $\times$ 10^6 years, which is too short compared to the age of the earth [14, 66]. There are as many as 10 - 12 successive steps in the decay series of naturally occurring radionuclides [55, 60]. Figure. 2.3 indicates schematically the relation between elements in these radioactive decay series [1]. In such decay chains the evolution of the radioactive daughters and their subsequent decays is dependent on the

growth arising from the parent decay rate as well as the decay rate of the daughters at each step in the chain [68]. This is described later using the Bateman equations.

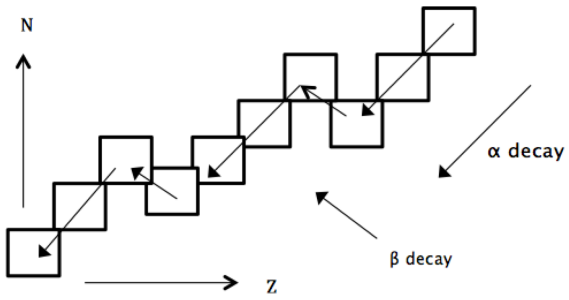

Figure 2.3: Scheme of multiple decay similar to the natural decay chains.

As can be seen from Fig. 2.4, Fig. 2.5 and Fig. 2.6, each radioactive decay chain is headed by a long-lived nuclide, ^{238}U (4.5×10^9 y), ^{235}U (7.1×10^8 y) and ^{232}Th (1.4×10^{10} y) [59]. These three long-lived parents decay to the stable lead isotopes of ^{206}Pb,^{207}Pb and ^{208}Pb, respectively through a series of intermediary decay products. The half-lives of intermediate nuclei ranges from microseconds to hundreds of years [14, 16].

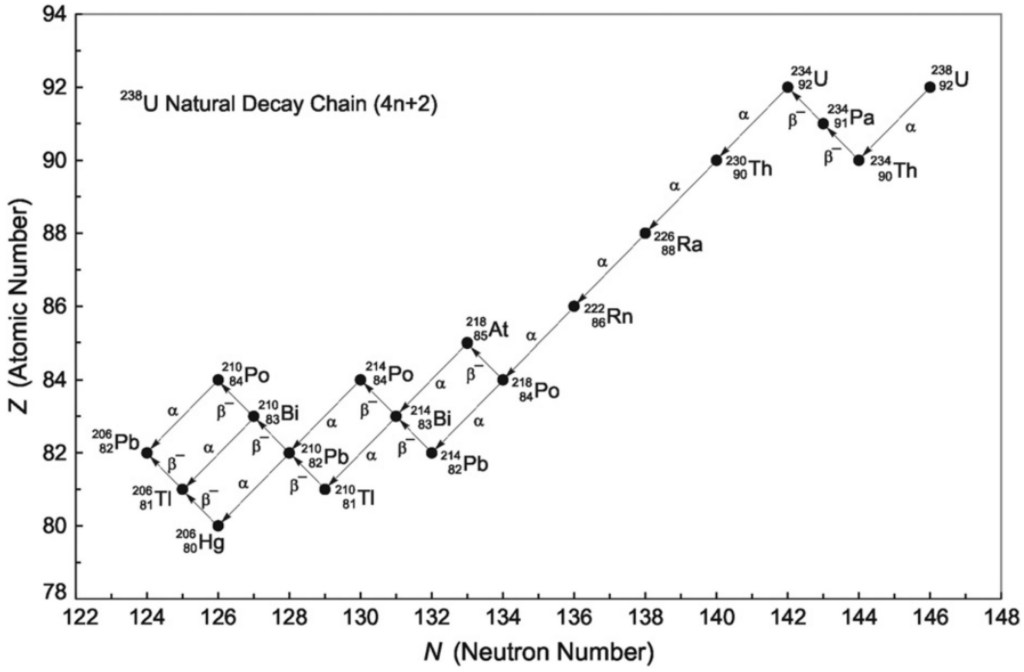

Figure 2.4: The ^{238}U natural decay chain [1].

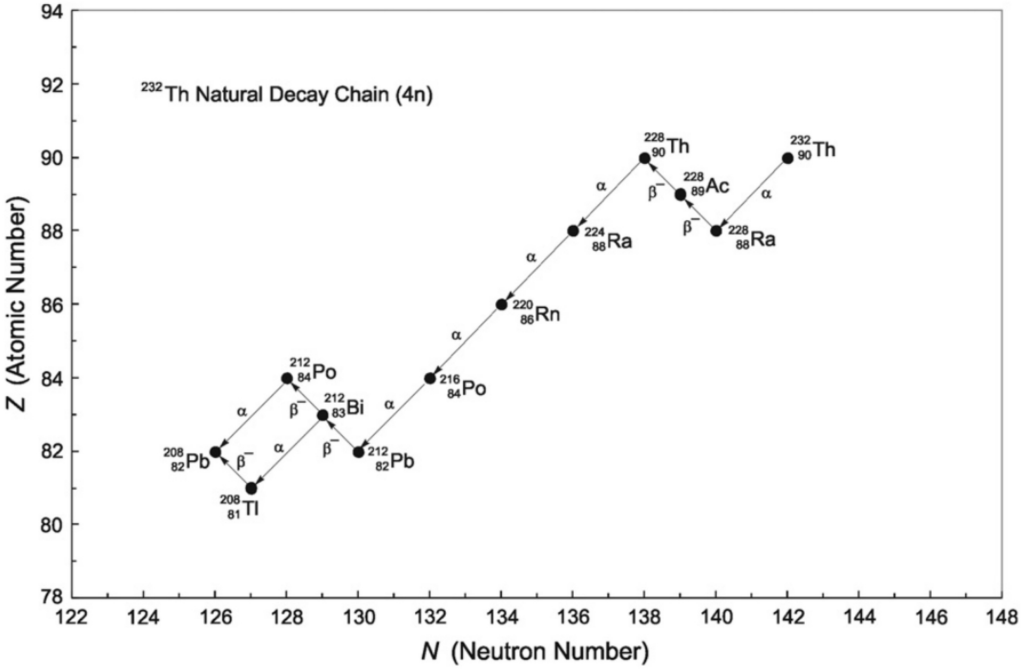

Figure 2.5: The ^{232}Th natural decay chain [1].

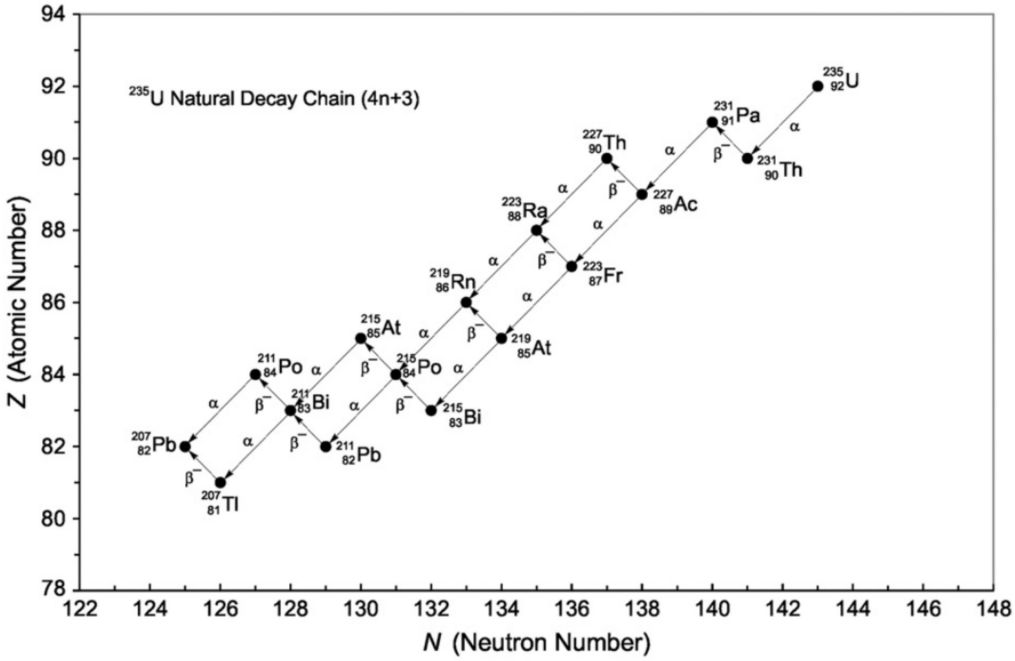

Figure 2.6: The ^{235}U natural decay chain [1].

2.4.1 The Bateman equations

In the case where the daughter of a radioactive nuclide is still unstable it continues to decay to other radioactive products until stability is reached. The evolution of a radioactive daughter is dependent on its decay rate as well as its rate of production from the radioactive parent [68]. The calculation of the decay rates of successive decays in a chain were first proposed by Bateman.

The Bateman equations applicable to radioactive decay can be written for parents and daughter products, respectively as [16].

$$\frac{dN}{dt} = -\lambda N, \tag{2.15}$$

$$\frac{dN_i}{dt} = -\lambda_i N_i + \lambda_{(i-1)} N_{(i-1)}, \tag{2.16}$$

where subscript $(i-1)$ denotes the next nuclide in the decay chain and λ is the decay constant as mentioned previously.

The solution of these equations leads to the expressions

$$N_1 = N_1^0 e^{-\lambda_1 t}, \tag{2.17}$$

$$N_2 = \frac{\lambda_1}{\lambda_2 - \lambda_1}\ N_1^0(e^{-\lambda_1 t} - e^{-\lambda_2 t}) + N_2^0 e^{-\lambda_2 t}, \tag{2.18}$$

where N_1^0 and N_2^0 are the parent and daughter nuclei at time t = 0, respectively. The first term on the right in Eq. 2.18 indicates the growth of N_2 by decay of N_1 and decay of N_2. The second term on the right reflects the contribution from any initially produced N_2 in the system [10]. This mathematical process can be extended to nth stage in the decay. For example, if there is a series of radionuclides N_1, N_2, N_3,., N_M, N_N and the corresponding decay constants λ_1,λ_2, λ_3,.., λ_M, λ_N, the evaluation of N_N will be given as [14].

$$N_N = N_1^0(C_1 e^{-\lambda_1 t} + C_2 e^{-\lambda_2 t} + C_3 e^{-\lambda_3 t} + \cdots + C_M e^{-\lambda_M t} + C_N e^{-\lambda_N t}) \tag{2.19}$$

in which the values for the coefficients will be written as

$$C_1 = \frac{\lambda_1}{\lambda_N - \lambda_1} \cdot \frac{\lambda_2}{\lambda_2 - \lambda_1} \cdot \frac{\lambda_3}{\lambda_3 - \lambda_1} \cdot \cdots \cdot \frac{\lambda_M}{\lambda_M - \lambda_1,} \tag{2.20}$$

$$C_2 = \frac{\lambda_1}{\lambda_1 - \lambda_2} \cdot \frac{\lambda_2}{\lambda_N - \lambda_2} \cdot \frac{\lambda_3}{\lambda_3 - \lambda_2} \cdot \cdots \cdot \frac{\lambda_M}{\lambda_M - \lambda_2,} \tag{2.21}$$

$$C_M = \frac{\lambda_1}{\lambda_1 - \lambda_M} \cdot \frac{\lambda_2}{\lambda_2 - \lambda_M} \cdot \frac{\lambda_3}{\lambda_3 - \lambda_M} \cdot \cdots \cdot \frac{\lambda_M}{\lambda_N - \lambda_M,} \tag{2.22}$$

$$C_N = \frac{\lambda_1}{\lambda_1 - \lambda_N} \cdot \frac{\lambda_2}{\lambda_2 - \lambda_N} \cdot \frac{\lambda_3}{\lambda_3 - \lambda_N} \cdot \cdots \cdot \frac{\lambda_M}{\lambda_M - \lambda_N.} \tag{2.23}$$

At time $t = 0$, $N_N = 0$ must be zero and so the value of coefficients is also required to be zero. Thus

$$C_N = C_1 + C_2 + C_3 \cdot \cdots + C_M + C_N = 0. \tag{2.24}$$

Using the mathematical solutions of the decay and growth of sequential decay of un-

stable radionuclides enables us to obtain a clear idea about the concept of equilibrium condition in a given system.

2.5 Radioactive equilibrium

Radioisotope decay equilibrium was first observed by Ernest Rutherford and Frederick Soddy in 1902 [1]. The phenomenon of radioactive equilibrium is the state when the members of the radioactive series decay at the same rate as they are produced [1]. Once the state of equilibrium has attained, the system will remain in secular equilibrium if there was not any process that occurs, leading to a fractionation of one or more of the daughter nuclides from their parents. However, after a sufficient time, depending on the half-lives of radionuclides, the system will return to the state equilibrium via the decay of excess daughter or ingrowth of daughter from the activity of a parent. In this section, the mathematical point of view of radioactive equilibrium will be considered with the three predominant cases of the state of equilibrium. For more detail about the mathematics governing parent-daughter abundances in a decay chain readers are directed to [1, 14]. There are three limiting cases for the decays of sequential radioactive decays involving the term equilibrium, these being (i) secular equilibrium; (ii) transient equilibrium and (iii) the state of no equilibrium [58, 60]. Each of these conditions is discussed in the following sections.

2.5.1 Secular equilibrium

Secular equilibrium is dependent on the mechanism of the decay and production of radionuclides in a decay chain. If the parent has a much longer half-life than the daughter, $\lambda_P \ll \lambda_D$, the daughter will eventually acquire the same activity as the parent in a closed system [69]. In this situation, it is said that a secular equilibrium was established between the two radionuclides and the activity of the daughter will decrease at the same rate as the parent [57]. Consequently, the daughter will behave as if it had the same half-life as its parent. In this case, secular equilibrium is likely to be established throughout the whole decay chain, as the radionuclides in the beginning of the natural decay chains always have

much longer half-lives than the rest. The time to reach secular equilibrium essentially depends on the half-life of the daughter as illustrated below. If the activity of the daughter is zero to begin with, it will take between approximately 7-9 half-lives of the daughter before it can be considered to be in secular equilibrium with its parent. Therefore, different time intervals are required to establish secular equilibrium between different radionuclides. Very short-lived radionuclides are expected to reach secular equilibrium with their parents or grandparents faster than long-lived radionuclides, which sometimes may have either higher or lower activity than their parent [58, 66, 69]. The decay of ^{238}U with half-life 4.5 billion years to ^{234}Th with half-life 24.1 days, i.e. $\lambda_{238} \ll \lambda_{234}$, has been selected as an example to explain the secular equilibrium condition in this section. According to the radioactive decay equations, the decay of ^{238}U is calculated using

$$A_1 = A_1^0 e^{-\lambda_1 t}, \tag{2.25}$$

where A_1^0 the amount of radioactive nuclide at time $t = 0$ and λ_1 is the decay constant based on the half-life of ^{238}U. However, the growth and decay of ^{234}Th can be given as

$$A_2 = \frac{\lambda_2}{\lambda_2 - \lambda_1} A_1^0 (e^{-\lambda_1 t} - e^{-\lambda_2 t}) + A_2^0 e^{-\lambda_2 t}, \tag{2.26}$$

where A_2^0 is the activity at time $t = 0$ and λ_2 is the decay constant of ^{234}Th. When $\lambda_1 \ll \lambda_2$, N_1 decays much slower than N_2 and the quantity $e^{-\lambda_1 t}$ is much larger than $e^{-\lambda_2 t}$ and Eq.2.26 can be written as follows

$$A_2 = A_1^0 (e^{-\lambda_1 t} - e^{-\lambda_2 t}). \tag{2.27}$$

For $\lambda_1 = 0$

$$A_2 = A_1^0 (1 - e^{-\lambda_2 t}). \tag{2.28}$$

When the time is infinite ($\lambda_2 t \approx \infty$), the decay rate of parent will be equal to daughter ($A_1 = A_2$). This is generally implied for any radioactive decay series provided that not

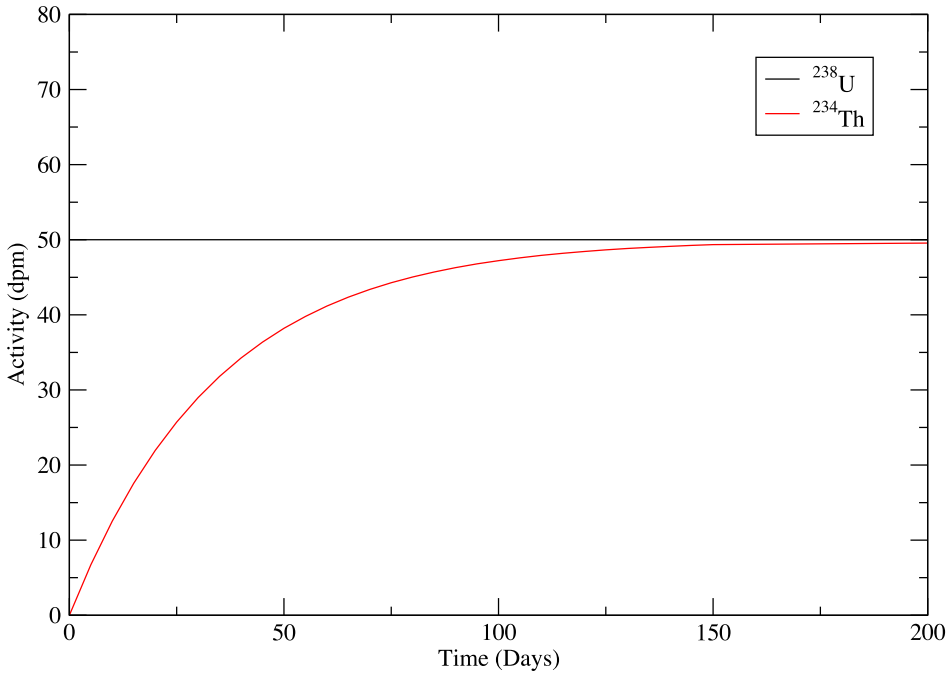

Figure 2.7: Growth of a short lived daughter ^{234}Th (24.1 d) from a much longer lived parent ^{238}U (4.5×10^9 y) until reaching Secular Equilibrium.

one or more of the daughter products have been removed from the system by a different process [14].

The results derived from these calculations are indicated in Fig. 2.7. As can be seen, the build-up and establishment of secular equilibrium of ^{234}Th from the extremely long-lived parent ^{238}U has been reached after about seven half-lives of ^{234}Th.

2.5.2 Transient Equilibrium

The state of transient equilibrium is similar to the the secular equilibrium state in which a steady-state condition occurs between the parent and daughter nuclides. This condition can occur if the half-life of the parent radionuclide is longer than that of the daughter but not significantly longer, i.e., where $\lambda_P \langle \lambda_D$ [1]. The approximation $\lambda_P = 0$ cannot be made in this condition [66]. When transient equilibrium state is established, the parente-daughter nuclides decay at the same half-life as that of the parent nuclide but they do not have the same activities [1].

As an example, Bateman equations have been applied on the decay of ^{234}U with half-life 2.5 M years to ^{230}Th with half-life 75000 years as shown in Fig. 2.8. As can be seen, the growth of the daughter, ^{230}Th, after zero activity at time (t = 0) occurs and a stationary state is reached after sufficient time, approximately three half-lives of the daughter, in which the daughter amount is larger than the parent amount. The activities of ^{234}U and ^{230}Th nuclei in this condition were calculated using Eq.2.25 and Eq.2.26, respectively. However, because the initial activities of ^{230}Th (t = 0) is zero, Eq.2.26 can be written as follows

$$A_2 = \frac{\lambda_2}{\lambda_2 - \lambda_1} A_1^0 (e^{-\lambda_1 t} - e^{-\lambda_2 t}), \tag{2.29}$$

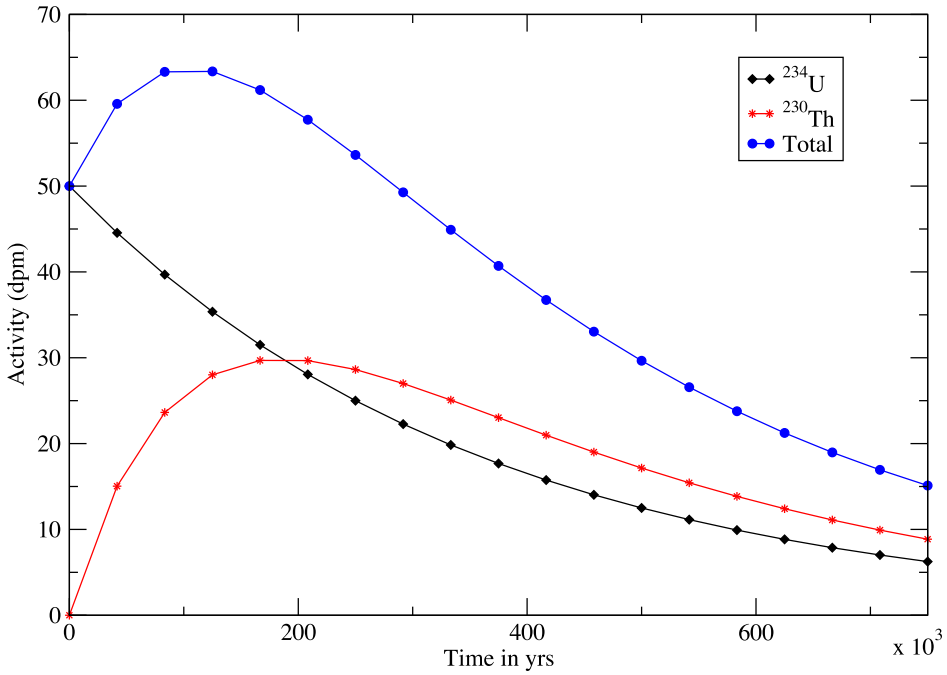

Figure 2.8: Growth and decay of a short lived daughter (^{230}Th) from a slightly longer lived parent (^{234}U) in Transient equilibrium.

2.5.3 No Equilibrium

When the half-life of the parent nuclide is shorter than that of the daughter product, the state of equilibrium will not be reached [57, 66]. Figure 2.9 illustrates the relation between the radioactivities of a parent and daughter when the half-life of the daughter (8 h) is larger than that of the parent (0.8 h). As can be seen, in the state of no equilibrium, the parent will decay away as a result of its shorter half-life, while the daughter product builds up to a maximum and then decreases eventually. The decay of parent nuclei is calculated from Eq.2.25 and the ingrowth of daughter is calculated from Eq.2.29.

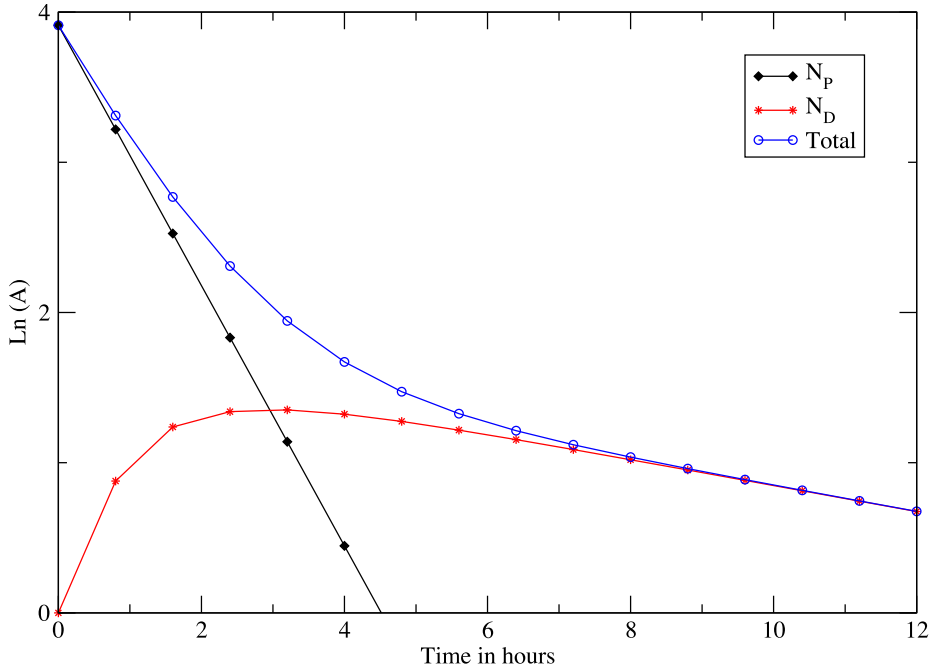

Figure 2.9: A logarithmic plot of the growth and decay of a longer lived daughter from a short lived parent in case of no equilibrium. Np and Nd indicate the amount of parent and daughter nuclei, respectively.

Chapter 3

Gamma-ray spectrometry technique

For accurate qualitative and quantitative analysis of U-series radionuclides in environmental samples, a variety of techniques have been applied and are constantly being developed for. However the only non-destructive technique, which requires a simple sample preparation (drying and weighing), is gamma-ray spectrometry. This system enables the simultaneous measurements of radionuclides from the natural decay chains [70, 71].

The technique of gamma-ray spectrometry using semiconductor detectors (particularly germanium detectors) will be discussed within this chapter. For other procedures, further information may be found in several textbooks and articles, see references [1, 27, 72, 73, 74, 75, 76, 77]. There are several types of germanium detectors available commercially; the most important for this work is hyper-pure germanium (HPGe) detector. The subject of this chapter is to introduce the principal methods and techniques employed to determine the activities of the radionuclides from the Uranium decay series. It discusses the prominent elements that can effect the reliability of the calculations.

3.1 Gamma-ray interactions in matter

The identification and quantification of radionuclides in this thesis is made through the detection and analysis of gamma-ray energy spectra using HPGe spectrometers. Gamma-

ray spectroscopy techniques are based on the detection of the gamma-ray photon energies originating from the decay of excited states in radioactive nuclides [27]. This emission is a characteristic for each radioactive isotope [27]. The precise measurement of these characteristic energies from gamma-ray spectra allows the identification of radionuclides.

The interactions of gamma-ray photons with matter give us an insight into the basic concepts underpinning gamma-ray spectroscopy because they explain the process by which photon energy is transferred either partially or completely to atoms. There are a number of processes by which gamma-ray photons and matter interact. However, the most important ones at typical gamma-ray energies for the decay series are the photoelectric effect, Compton scattering and pair production as explained in the following sections [78, 79, 80].

3.1.1 Photoelectric effect

In this interaction a gamma-ray photon transfers all of its energy to a tightly bound electron and completely disappears in the absorber (detector). An energetic photoelectron from a K-shell of the atom is ejected to conserve energy [12, 79, 80]. The photoelectron appears with an energy equal to

$$E_e = h\nu - E_b, \tag{3.1}$$

where E_b is the binding energy of the electron to an atom and $h\nu$ is the incident γ-ray energy. The probability of this interaction is dependant on the gamma-ray energy, the binding energy of the electron, and the atomic number of the atoms [81, 79, 80]. The absorbent atom is ionized with the interaction leaving a vacancy or a hole in the bound shell. The hole is afterwards filled up with any free electron in the medium or simply filled by rearrangement of the electrons from other shells. The latter may result in generation of characteristic X-rays or Auger electrons [12, 82]. This type of interaction is the most important one for gamma-ray spectrometry because the full-energy peaks (photopeaks) can be obtained when all the gamma-ray energy has been lost to the detector material in a single exchange [79, 80, 82].

3.1.2 Compton scattering

Compton scattering occurs between an incident gamma-ray photon and a weakly bound or free electron in the absorbing material. Here the interaction differs from photoelectric effect in such a way that the incident gamma photon loses only part of its energy and deflects through a given angle θ (scattering angle) from its original direction [81]. This scattering results in a free electron with energy equal to the difference between the energies of the incident and scattered gamma-ray photon. Equation 3.2 expresses the relationship between energy of the scattered gamma ray and the electron (Compton electron) [79, 80, 82]

$$E_c = hv - hv', \tag{3.2}$$

where E_c is Compton electron energy and

$$h\nu' = \frac{h\nu}{1 + \alpha(1 - cos\theta)}, \tag{3.3}$$

where hν and hν' are the energies of the incident and scattered gamma rays, respectively, θ is the scattering angle (in the range of 0 to 180) and $\alpha = h\nu/m_0c^2$ (where m_0c^2 is the rest mass of the electron). During this process, all scattering angles from 0° to 180° are possible in the detector resulting in a continuum of energies for the scattered photon [82]. Compton scattering is the dominant process for low-Z materials and in the energy range of 200 keV $\sim$ 1.2 MeV [12, 78].

3.1.3 Pair production

This process can only take place if the gamma-ray energy exceeds twice the rest mass energy of the electron (1.02 MeV), that is $h\nu \geq m_0c^2$ (where m_0c^2 is the rest mass of the electron). The photon energy is converted into an electron-positron pair within the field of an atomic nucleus. During pair production, a gamma-ray photon energy $h\nu$ is converted into $2m_0c^2$ with any excess being translated into the kinetic energies of the electron-positron pair [82]. This excess energy is always distributed between those partners (electron and positron) in range of zero to the maximum of h$\nu - 2m_0c^2$. The positron

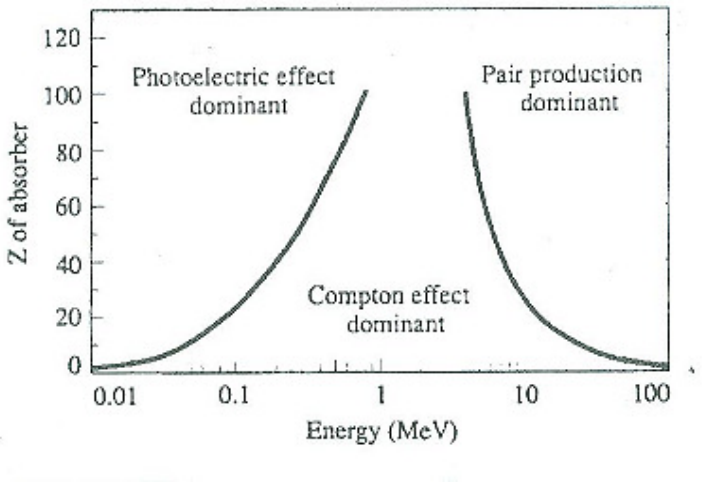

Figure 3.1: The relative important of the three major type of gamma-ray interaction [59, 81].

will thermalise and subsequently annihilate with an electron resulting in the release of two 0.511 MeV photons [82].

Figure. 3.1 indicates how the three interaction processes depend on the gamma-ray energy. It can clearly be seen that the effect of photoelectric absorption is most important at low energies and for high-Z materials. However, the importance of pair production rises with gamma-ray energy [81].

3.2 Gamma-ray interactions in a Ge spectrometer

There are many features relating to the geometry of the gamma-ray spectrometer that can influence the appearance of the gamma-ray spectrum e.g. the detector size [82]. Consider, a beam of gamma rays of exactly the same energy, which is greater than 1022 keV incident on a very large detector. As can be seen from Fig. 3.2, various successive Photoelectric Absorption, Compton Scattering and Pair Production interactions are possible that will result ultimately in the complete absorption of the gamma-ray energy resulting in a spectrum of the form shown in Fig. 3.2. This single gamma-ray peak signifies the full-energy peak and represents one extreme of the influence of detector size [12, 59].

If the same conditions occur in a small detector (Fig. 3.3) where only one interaction

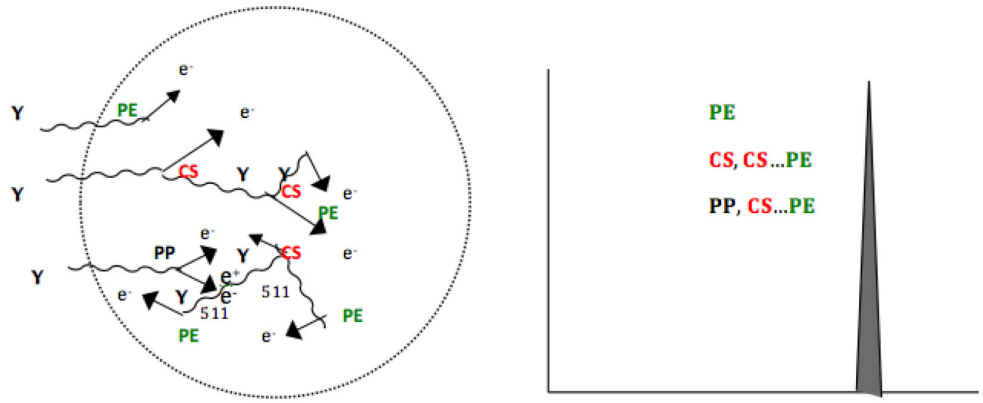

Figure 3.2: Interactions of gamma rays in a large detector and the resulting spectrum. Photoelectric, Compton and pair production interations are labeled as PE, CS and PP, respectively.

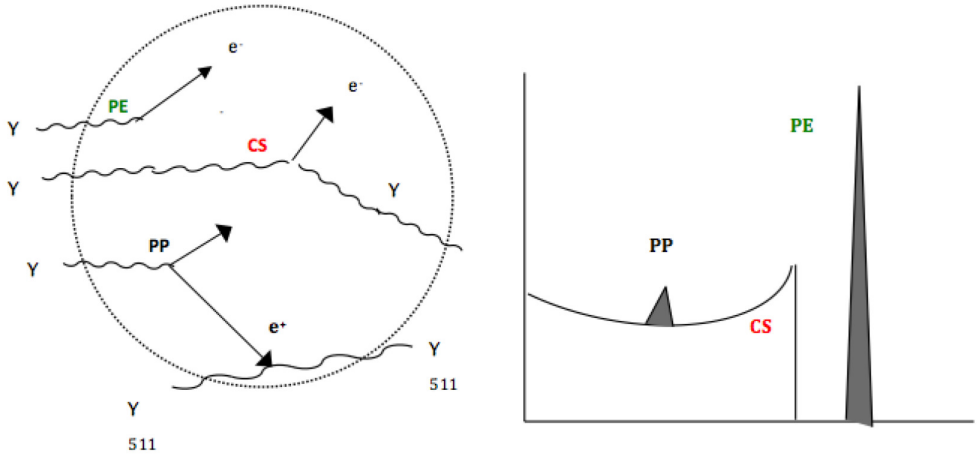

Figure 3.3: Interactions of gamma rays in a small detector and the resulting spectrum. Photoelectric, Compton and pair production interations are labeled as PE, CS and PP, respectively.

can take place, only photoelectric absorption will produce a full-energy absorption. Compton scattering events will produce a background continuum depending on the scattering angle and pair production may give rise to a double escape peak because both 511 keV annihilation gamma rays escape the detector volume [59].

In any real detector there will be other possibilities. Multiple Compton scatters may follow an initial scattering event before the gamma ray is lost from the detector volume. In

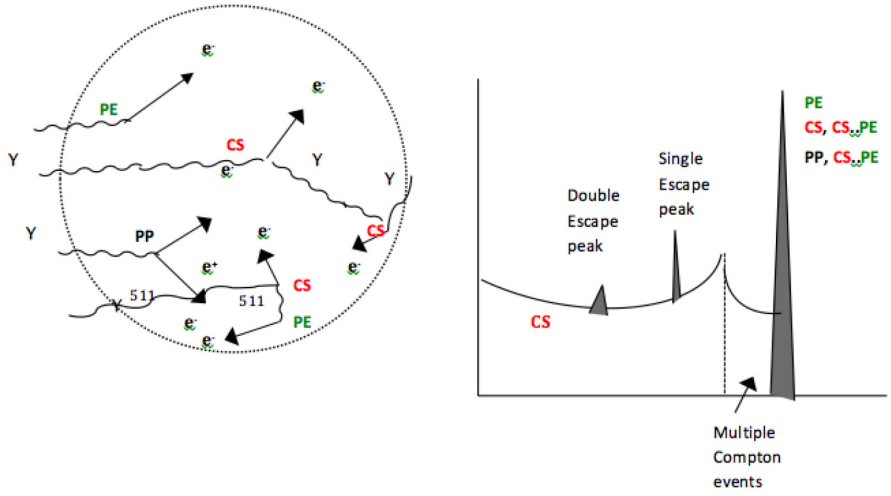

Figure 3.4: Interactions of gamma rays in a real detector and the resulting spectrum. Photoelectric, Compton and pair production interations are labeled as PE, CS and PP, respectively.

these cases this will result in events which appear in the spectrum between the Compton edge and the full-energy peak. Pair production may be followed, after annihilation of the positron, by the loss of one or both annihilation gamma rays resulting in separate peaks in the spectrum representing $E-511$ keV and $E-1022$ keV, respectively. These features are shown schematically in Fig. 3.4 [59]. For more understanding, a typical spectrum for ^{60}Co was acquired from BEGe detector with a counting time of 600 s is also shown in Fig. 3.5. In addition to the two characterised photopeaks, the Compton continuum created from each of the two gammas can be seen on the spectrum. The Compton edges can also be seen on the spectrum, however it is difficult to see the single escape (SE) and double escape (DE) peaks from pair production interactions due to the gamma-ray energy of 1332 keV is slightly above the threshold for pair production [59].

3.3 Gamma-ray spectrometer system

In general, there are two types of detectors that can be used for gamma-ray spectrometry; scintillation detectors and semiconductor detectors. Semiconductor detectors have several advantages over scintillation detectors. Although semiconductor detectors are not as efficient as scintillators such as NaI(Tl) they readily detect photons and produce fast pulses

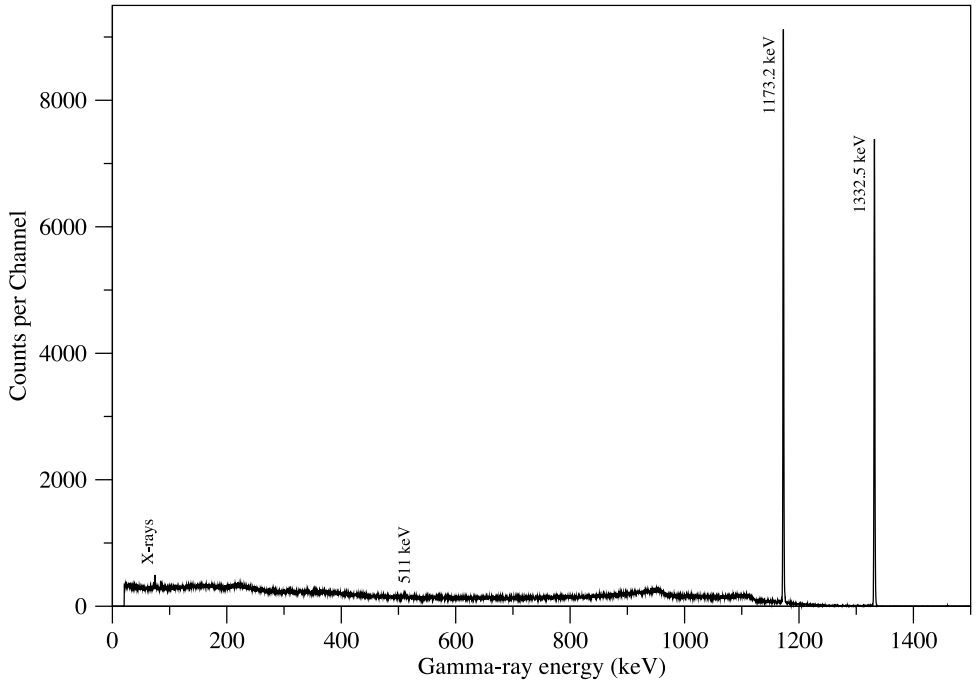

Figure 3.5: The ^{60}Co gamma-ray spectrum acquired from BEGe-2825 detector with the two characterised peaks labeled.

with excellent energy resolution [59].

It is important to know the structural composition of the semiconductor material in terms of the atomic structure of these materials. Fundamentally, there are three types of material with respect to conductivity, insulators, conductors and semiconductors. Solids are characterized in terms of two energy bands in which electrons may reside; the valence band and the conduction band, which are separated by an energy difference called the band gap. Understanding the electronic structure in terms of how these bands are filled and the gap between them is important to understand their conductive properties. In the valence band (lower layer) electrons are bound to specific sites and cannot easily migrate. These materials are known as insulators and significant energy (> 5 eV) is needed to promote electrons from the valence band to the conduction band. In insulators, all the

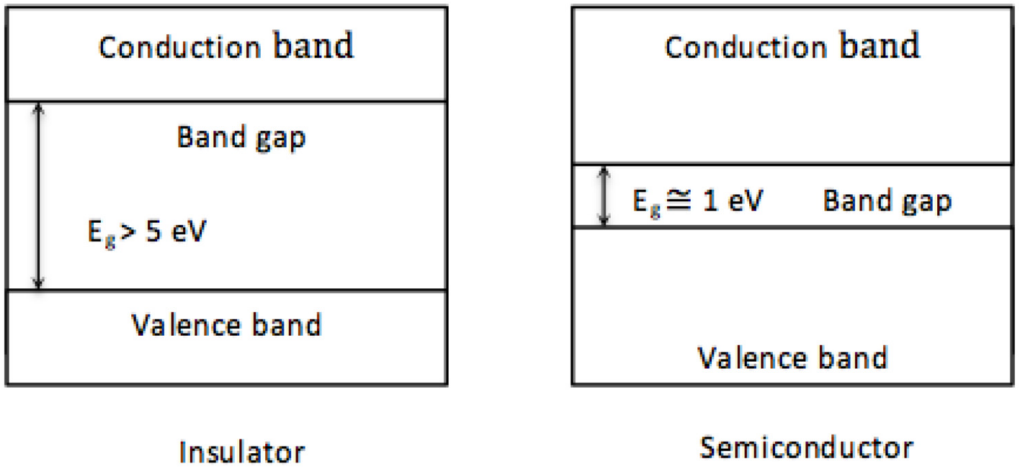

Figure 3.6: Band structure for electron energies in insulators and semiconductors modified from.

electrons fill the valence band and there is a large gap (forbidden band) between the two bands, see Fig. 3.6. Conductors are materials such as Copper that have a partially filled conduction band. Copper is an excellent conductor since each atom has a free electron that moves easily between atoms in a bulk material. An electric current is produced when the electrons are free to move through the material under the action of an external field. Semiconductors are materials such as Germanium, where the band gap is smaller as shown in Fig. 3.6 and less energy is required in order for electrons migrate between the two energy bands [59].

3.3.1 Germanium and silicon crystals

Semiconductors used in detectors are typically elements that have four electrons in the valence gap. Silicon and Germanium are tetravalent elements. In any solid substance that is composed of silicon or germanium atoms, the two energy bands are separated by a narrow gap. To get an electric current in semiconductor, an external energy must be applied to make electrons migrate through the band gap into conduction band although a number of electrons (perhaps 1 in 10^9) is thermally excited at room temperature. This results in a valence-band vacancy known as a hole. An electron from a neighbouring atom subsequently fills the hole creating in the process a new hole. Under the action of an

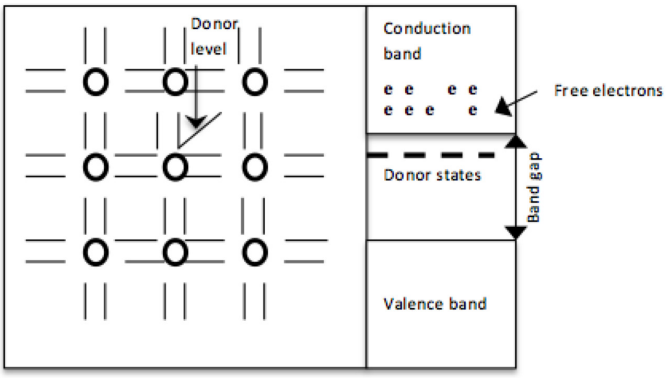

Figure 3.7: N-type semicondutor.

external field, the hole appears to migrate through the crystal but of course the positively charged atoms do not move [57].

N-type and p-type material

In the crystal, atoms are distributed in the form of identical unit cells. In silicon and germanium crystals, each atom forms a covalent bond with four neighbouring atoms since the outer shell that can accommodate up to eight electrons. The conduction properties of the semiconductor can be modified by introducing new materials into the lattice. For example, n-type semiconductors can be constructed by introducing a small dopant concentration of valence-5 (pentavalent) atoms, which introduces a donor electron. For this reason they are called n-type semiconductors. Whereas, the process of of using trivalent (valence-3) atoms introduces acceptors resulting in a p-type semiconductors. In this case the dominant charge carriers are holes [57]. A schematic illustration of both types can be seen in Fig. 3.7 and Fig. 3.8.

When p-type and n-type materials are put into contact with each other, the diffusion of electrons across the junction from the n-type material into the p-type material can take place and combine with the holes. The charge carriers are neutralized in the vicinity of the junction, creating a region called the depletion region. Ionized fixed donor sites are created after the diffusion of electrons from the n-type region, whereas negatively

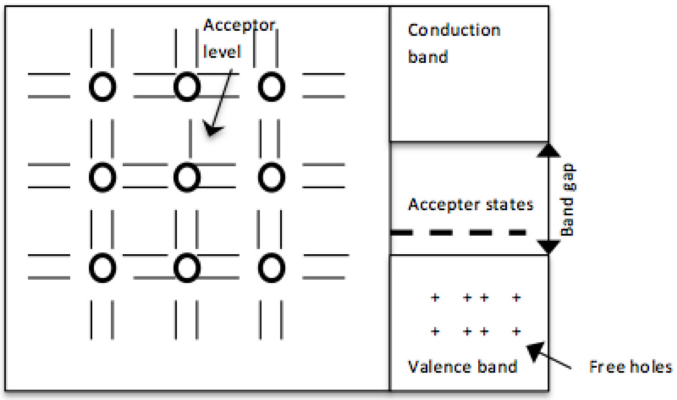

Figure 3.8: P-type semicondutor.

charged fixed acceptor sites are left as a result of the similar diffusion of holes from the p-type region. An electric field is created from the space charge from the fixed sites, which ultimately stops further migration [57]. Electron-hole pairs are created when radiation interacts within the depletion region that flow in opposite directions. Thus, an electronic pulse can be generated from the total number of electrons and the amplitude of this pulse is proportional to the energy of incident radiation [57]. Hyperpure Germanium detectors are the favoured instruments for high-energy resolution gamma-ray studies since they were introduced in the early 1960 [81, 78, 83, 84]. The components of a Germanium spectrometer are described below.

3.3.2 Detector and processing electronics

In order for the detector and the system components to operate, a high voltage power supply has to be applied, which is typically about 3000 V for HPGe detector [81, 83, 84]. The bias voltage has two functions. Firstly, the increase of the electrical field magnitude in the depletion region. Secondly, it works to increase the sensitive volume of the detector by increasing the the dimension of the depletion region. In both cases, this results in generating more charge carriers [57].

The next component, which is normally attached to the detector, is the preamplifier. The function of the preamplifier is to collect the charge generated after the interaction of

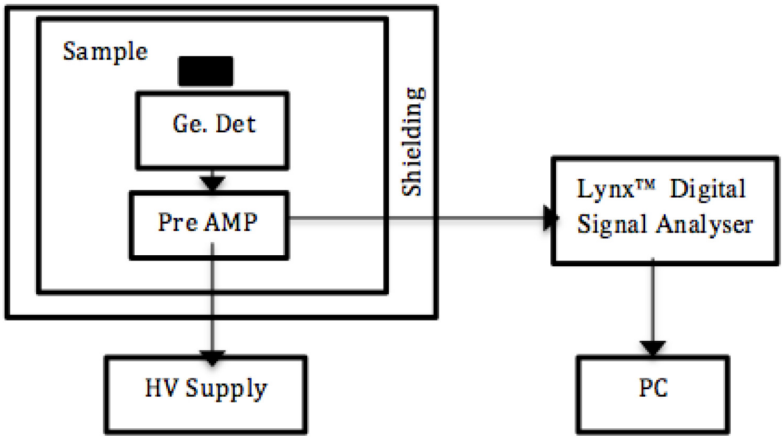

Figure 3.9: Main components of a system for gamma-ray spectroscopy.

the gamma-ray photons within the detector crystal. Also it matches the high impedance of the detector and low impedance of coaxial cables to the amplifier [81, 83, 84, 85]. In a modern system, the detector signal is digitized directly from the preamplifier with only some minor preconditioning (Lynx Digital Signal Analyzer) [85]. Fig. 3.9 demonstrates a schematic block diagram for gamma-ray spectrometry system used in this work.

The flow chart in Fig. 3.10 indicates the basic process of gamma-ray photon detection by a germanium detector. When a radiation interaction occurs within the depletion region, electrons from the initial generate secondary electrons that are swept towards the electrodes by the applied electric fields, which generates an electrical signal [81, 83, 84]. The height of the signal is proportional to the energy dissipated in the detector.

High-resolution gamma-spectrometry is a powerful tool for analysing low-level activity measurements for environmental samples with different matrix compositions. This technique is widely used in such measurements due to the simplicity of technique and sample preparation [68]. Depending on the purpose of measurements and the energy range of interest, HPGe detectors are available in various sizes, geometries (coaxial and planar) and etc. In this study, the activities of radionuclides in sediment samples were determined by using an existing high-resolution gamma-ray spectrometry system. This consists of a shielded hyper-pure germanium detector, electronic signal processing instrumentation and digital data readout devices. The broad energy germanium detector, BEGe-2825 model,

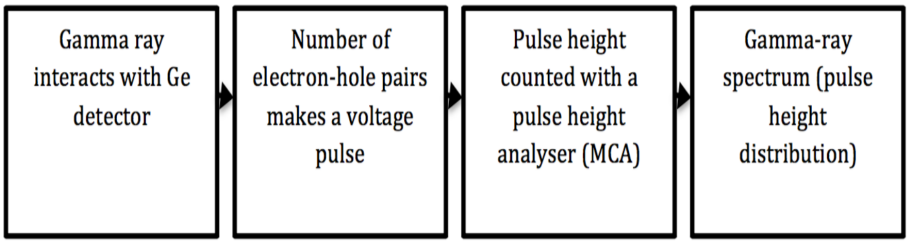

Figure 3.10: The flow chart for the detection of gamma rays in a Germanium spectrometer.

was chosen for two reasons. Firstly, this detector has the ability to cover a wide energy range of 3 keV to 3 MeV [86, 87] with reasonable efficiency across the energy range of interest in this study. Secondly, it is characterised with an excellent efficiency and high resolution for low-energy gamma rays [86, 88]. These characteristics make the BEGe detector ideal for the measurement of environmental samples that involves the analysis of complex spectra with many low-energy transitions [68, 88]. The dimensions of this detector are displayed in Fig. 3.11 [89]. Table 3.1 lists the characteristics of this detector, which were obtained from the manufacturer's data sheet and Refs. [86, 89]. The BEGe detector system used a Canberra Lynx data acquisition system with a 14-bit 80 MHz flash ADC with an internal trigger. The digital electronics give excellent spectra with good energy resolution with long term stability. This stability was important as measurements took up to seven days.

3.3.3 Shielding

The measurement system for this work mounts the Germanium detector in a shielded castle to lower the detection of the ambient gamma-ray background [79, 80]. There are many sources from the background that can contribute to the measured spectra. Radionuclides from the decay chains of ^{232}Th and ^{238}U, and ^{40}K are the most significant sources for background radiation because of their relatively long half-lives [59]. Another contribution

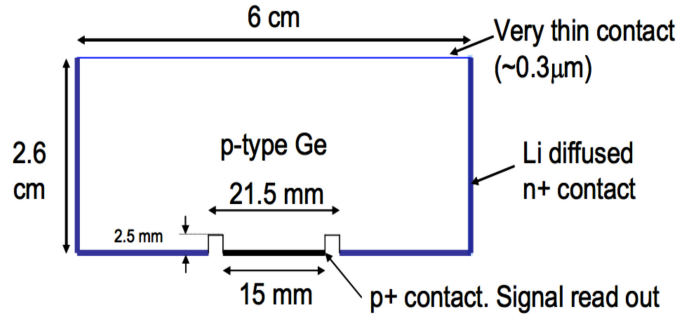

Figure 3.11: Broad Energy Germanium Detector Dimisions [89].

Table 3.1: Specification of the system used.

Type	Planar (BEGe)
Model	BE2825
Manufacturer	Canberra
Relative Efficiency (%) at 1332.5 keV	18
FWHM at 122 keV	0.633 keV
FWHM at 1332.5 keV	1.717 keV
Crystal type	P
Diameter (cm)	6.1
Thickness (cm)	2.6
Area $(cm)^2$	28
Window material	Carbon Epoxy
Window thickness (mm)	0.6
Distance from window (mm)	5
Depletion voltage	+3500V
Recommended bias	+4000V

to the background radiation is cosmic radiation. In order to analyse an accurate gamma spectrum originating from a sample, a proper shielding must be used. This is made using high-density materials that have high atomic numbers, to maximise a high photoelectric absorption probability and a high linear attenuation coefficient for background gamma rays [79, 80]. Lead and steel are the materials of choice for this purpose. However, lead is prefered because of its high atomic number (Z=82) and high density (11.35 g/cm^3) [79, 80]. Moreover, backscattered gamma radiation within the shield decreases with increasing the atomic number [90].

Figure. 3.12 shows a detector that is enclosed with a 5 cm thick cylindrical lead shield to reduce the background radiation from various natural radiation sources. A graded shield

Figure 3.12: BEGe detector, shielding system and cryostat.

with tin and copper layers is used to attenuate X-rays. This detector window is made from carbon because it allows excellent transmission for very low gamma-ray energies [91].

3.3.4 Dewar and cryostat

In addition to shielding arrangements, these detectors must be cooled in order to reduce the thermal generation of charge carriers to an acceptable level since germanium has a relatively low band gap (0.7 eV) [59, 81]. In the absence of cooling, leakage current induced noise causes the energy resolution of the germanium detector to deteriorate. Liquid nitrogen (77 K temperature) is the commonly used liquid for this purpose although electro-mechanical coolers are becoming standard [1, 85]. Liquid nitrogen is stored in a dewar and a thermal contact is made with the semiconductor crystal via a copper cold finger [59, 91, 81, 85, 83, 84] . The cryostat houses the detector crystal. Typically it is preferable for the detector to be placed within a short distance (5mm) from the cryostat endcap window. This is particularly necessary for the samples to be as close as possible to the detector crystal [90]. These two parts are shown in Fig. 3.12. The Dewar, the cryostat and the preamplifier are generally supplied with the detector.

Chapter 4

System calibration

The sensitivity of a detector is defined in terms of its photopeak efficiency and resolution. Generally, all detectors come with specifications from the manufacturer, which state the detector efficiency, energy resolution and peak-to-total ratio. This chapter discusses concepts related to the operational characteristics of a semiconductor spectrometer. It deals with the first part of the conceptual methodology applied and the procedures followed in this study. Energy calibration, resolution and efficiency calibration are discussed. The typical approach for efficiency calibration based on standard or reference materials is also highlighted though was not employed for the final efficiency and activity calculations. The calculation of detection efficiency based on the LabSOCS software (Laboratory Sourceless Object Calibration Software) is discussed involving the parameters that influence the detection efficiency and introduce uncertainties to calculations. The validation of these calculations is presented.

4.1 Energy calibration

To analyse and identify unknown samples using a HPGe detector, the counting system should be calibrated in order to convert the channel scale into an energy scale. Normally, the gamma energy follows a linear relationship with the channel number as,

$$y = Bx + C, \tag{4.1}$$

where y is the energy of the source, x is the channel number and B and C are the calibration coefficients corresponding to the gradient and intercept, respectively. The PC-based multi-channel analyser (MCA) within the Prospect software was used to perform a calibration to provide a linear energy scale.

The system was calibrated using a calibrated source (NPRL-604) in a Marinelli beaker geometry. This source emits gamma rays originating from a variety of radionuclides across a wide energy range as shown in Table 4.1. The gamma-ray spectrum obtained for the NPRL-604 source can be seen in Appendix A (A.4.1). The energy calibration line was also obtained from the experimental results as shown in Fig. 4.1.

Table 4.1: Decay data for radionuclides in the NPRL-604 Marinelli source used in the energy calibration. The gamma-ray energies and channel numbers measured after the calibration are shown to the right-hand side of the vertical line.

Radionuclide	Half-life	Tabulated γ-ray energy (keV)	Measured γ-ray energy (keV)	Channel number
^{241}Am	432.6 y	59.5	59.5	230.1
^{109}Cd	461.4 d	88.0	88.0	339.9
^{57}Co	271.7 d	122.1	122.0	471.1
^{139}Ce	137.6 d	165.9	165.8	639.7
^{51}Cr	27.7 d	320.1	320.0	1233.7
^{113}Sn	115.1 d	391.7	391.8	1510.0
^{85}Sr	64.9 d	514.0	514.1	1981.0
^{137}Cs	30.1 y	661.7	661.6	2549.5
^{88}Y	106.6 d	898.0	898.0	3460.0
^{60}Co	1925.3 d	1173.2	1173.2	4519.7
^{60}Co	1925.3 d	1332.5	1332.3	5133.0
^{88}Y	106.6 d	1836.1	1835.9	7072.2

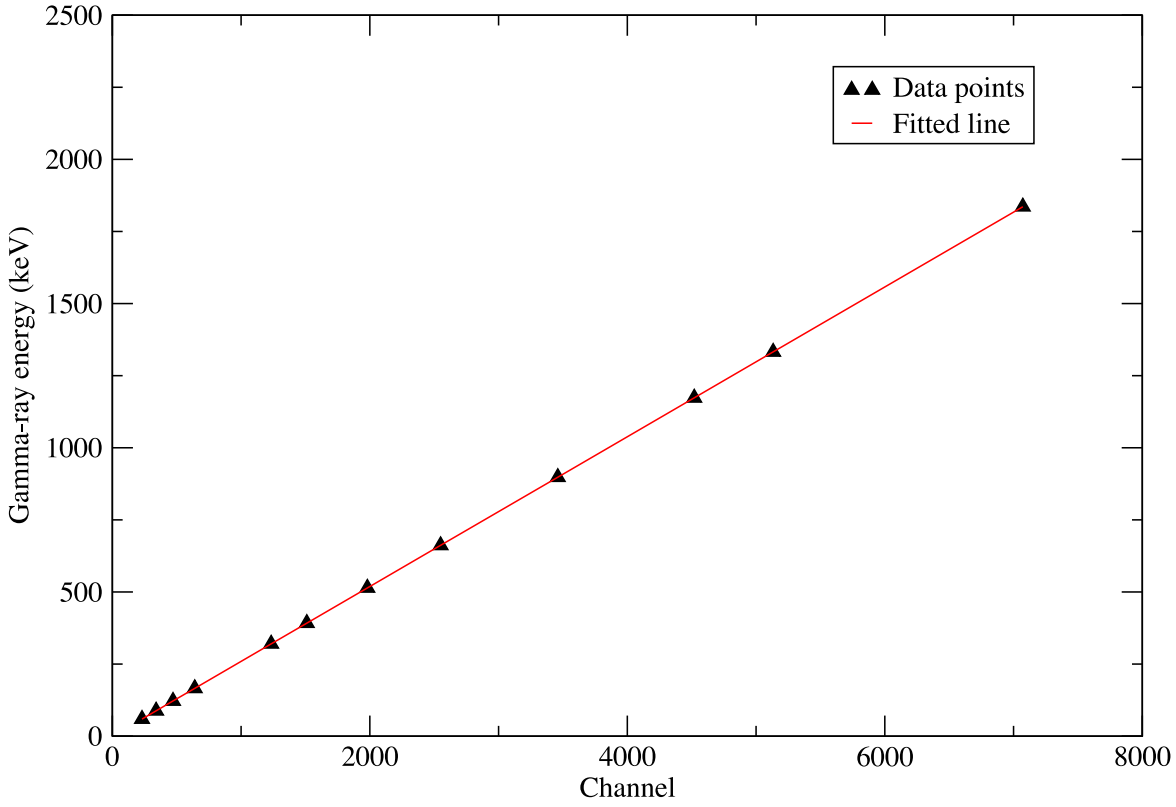

Figure 4.1: The energy calibration line for the BEGe-2825 detector. Regression coefficient is 1.

The calibration is checked every two to three counted samples by the same source to ensure that there are no gain drifts and that the calibration remains constant over time.

4.2 Resolution

The resolution is a measure of the full width at half maximum (FWHM) as shown in Fig. 4.2 and is expressed in term of energy spread for a specific gamma-ray energy [59]. A Gaussian distribution is often a good representation of the shape of a peak in a gamma-ray spectrum. The FWHM for a Gaussian peak is related to the standard deviation σ as

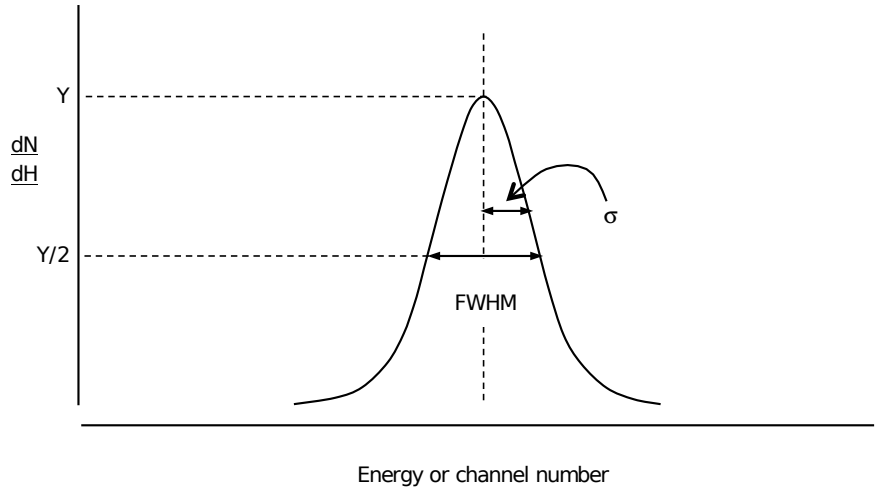

Figure 4.2: Full Width at Half Maximum [59].

$$FWHM = 2.35 \times \sigma. \tag{4.2}$$

The resolution can be deduced by measuring the narrowness of the peaks in a spectrum. For semiconductor spectrometers with high resolutions, such as Ge, it is possible to resolve between adjacent peaks and therefore it is easier to discriminate between close energy levels [81].

A plot of measured FWHM against energy is shown for the BEGe detector in Fig. 4.3(a). It is shown that the FWHM increases from 0.5 keV at 59.5 keV to 1.9 keV at 1836.1 keV. Compared to the manufacturer's specification, the energy resolution is slightly improved, which was 0.7 keV at 122.0 keV and 1.7 keV at 1332.5 keV, whereas in the present work is 0.6 keV and 1.6 keV at 122.0 keV and 1332.5 keV, respectively.

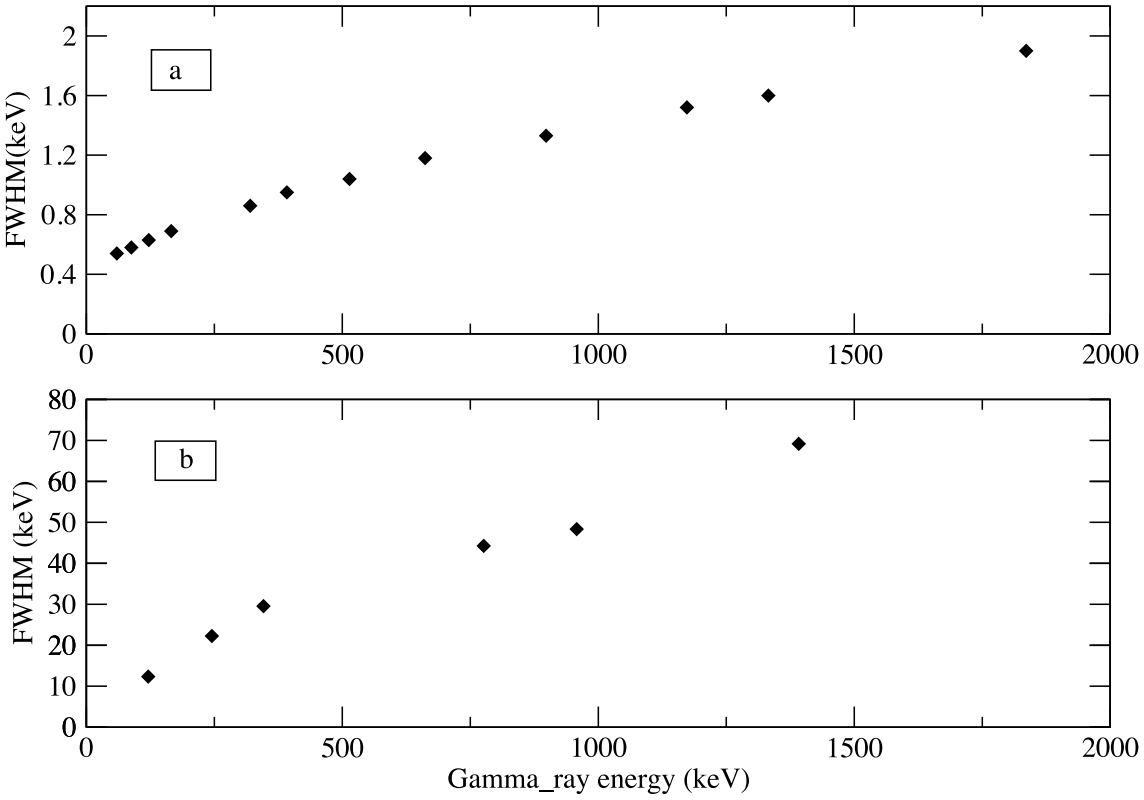

Figure 4.3: A plot of Full-Width Half-Maximum (FWHM) as a function of gamma-ray energy for a Broad-Energy Ge (BEGe) detector (a) and NaI(Tl) detector (b).

It can also be seen from Fig. 4.3(a) that the full-width half-maximum across the full-energy range up to 2 MeV for BEGe detector is less than 2 keV. Figure. 4.3(b) shows the corresponding variation in FWHM for a NaI(Tl) scintillator detector. This comparison indicates that the energy resolution of the BEGe detector is a factor of $\sim$35 times better than the NaI(Tl) detector in Fig. 4.3(b).

The resolution of BEGe detector was also plotted against a Coaxial type germanium detector as indicated in Fig. 4.4. It can be seen clearly that the BEGe detector has a superior resolution especially at low energy gamma-ray, where it is increased by more than 40%, compared to Coaxial type germanium detector, which has the same diameter

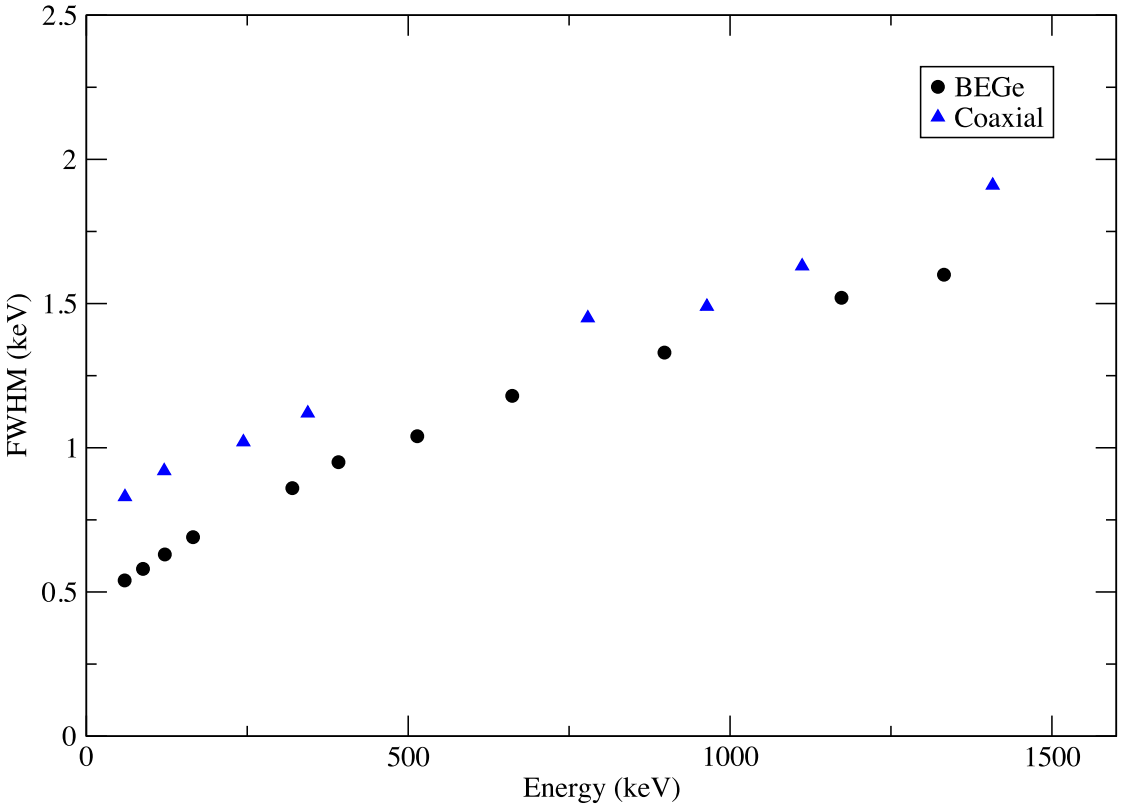

Figure 4.4: A plot of Full-Width Half-Maximum (FWHM) as a function of gamma-ray energy for a Broad-Energy Ge (BEGe) detector and Coaxial Ge detector of the same diameter. The same data presented in Table. 4.2 and Table. 4.3.

of 60 mm. This makes the BEGe detector better to be used for the analysis where the gamma-ray lines of 46 keV, 63 keV and 92 keV from the U-series decay to be used. The spectrum of low energy gamma rays from a standard calibration source is shown in Fig. 4.5.

Table 4.2: Data for FWHM against gamma-ray energy for BEGe detector.

γ-ray energy (keV)	FWHM
60	0.54
88	0.58
121	0.63
166	0.69
320	0.86
392	0.95
514	1.04
662	1.18
898	1.33
1173	1.52
1332	1.60

Table 4.3: Data for FWHM against gamma-ray energy for Coaxial detector.

γ-ray energy (keV)	FWHM
60	0.83
121	0.92
244	1.02
344	1.12
443	1.20
779	1.45
964	1.49
1112	1.63
1408	1.91

4.3 Efficiency calibration

The precise determination of the detector efficiency is an important issue in terms of the reliability of the results under analysis. There are several definitions of efficiency:

- **Absolute efficiency** The absolute efficiency is defined as the ratio of the number of counts detected to the number of gamma rays emitted by the source [59]

$$\text{Absolute efficiency} = \frac{N_c}{N_s}, \tag{4.3}$$

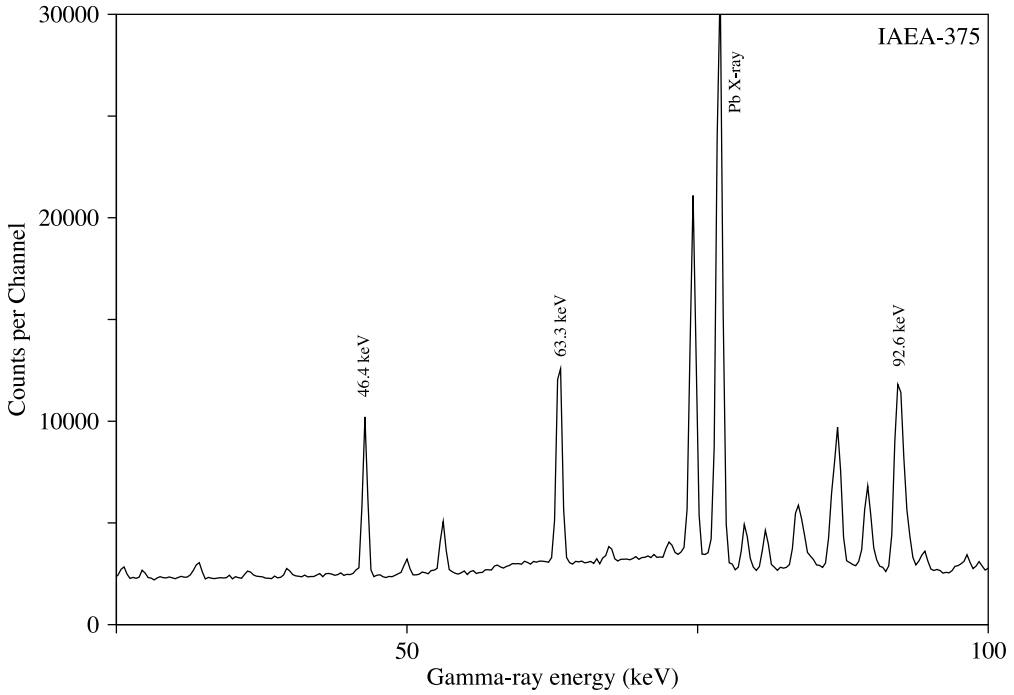

Figure 4.5: A plot of the IAEA-375 standard source spectrum from the Broad-Energy Ge (BEGe) detector.

where N_c is the number of counts and N_s is the number of photons emitted by the source.

- **Relative efficiency** The relative efficiency is defined relative to a 75 mm × 75 mm sodium iodide NaI(Tl) detector detecting 1332 keV photons from a ^{60}Co point source of known activity at a position of 25 cm from the front of the crystal.

- **Intrinsic efficiency** The intrinsic efficiency is defined as the ratio of the number of counts recorded by the detector to the number of gamma rays striking the detector [59]

$$\text{Intrinsic efficiency} = \frac{N_c}{N_p}, \tag{4.4}$$

where N_c is the number of counts and N_p is the number of photons incident on the detector.

- **Full-Energy Peak Efficiency** The FEP Efficiency is the ratio of the number of counts in full-energy peak corresponding to energy E, by the number of photons with energy E emited by the source (F(E)).

$$\text{FEP efficiency} = \frac{N_p(E)}{F(E)}, \tag{4.5}$$

where N_P(E) is the number of counts in full-energy peak corresponding to energy E and F(E) is the number of photons with energy E emitted by the source.

Among the various types of efficiencies listed previously, we are only interested in the Full-Energy Peak (FEP) efficiency. The efficiency calibration determines a function describing the full-energy peak detection efficiency as a function of the γ-ray energy. The main procedure for efficiency calibration in this thesis is based on modeling using a specific software (LabSOCS). However the experimental determination for the detection efficiency was also carried out using different sources and geometries in order to validate the detector characterizations and the procedure adopted. The following sections will present and discuss the conventional method used for efficiency calibration where the standard sources or material that have identical chemical and physical parameters to the measured samples. The effects that influence the detection efficiency, for example the self-absorption effect, are also explained.

4.3.1 Experimental efficiency calibration

To produce an experimental efficiency calibration of a detector, the typical approach involving a standard or reference mixed gamma source with multiple energy transitions, in a similar geometry to the measured samples, should be used [92, 93]. These reference materials should be traceable to well known international reference materials manufacturing organization e.g. NIST and IAEA. By counting the standard source or material and recording the net peak area from the spectrum for each nuclide, the efficiency (ε) can be calculated using this equation

$$\varepsilon(\%) = \frac{NA}{T \times A_\gamma} \times 100, \tag{4.6}$$

where NA is the net peak area, T is the live time, A_γ is gamma activity, which is equal to (source activity $\times$ gamma branching ratio). Also the source activity is calculated with the decay equation

$$A = A_0 e^{-\lambda t}, \tag{4.7}$$

where A_0 is the initial activity, t is the time since A_0 until the time of measurement and λ equals

$$\lambda = \frac{ln(2)}{t_{1/2}}, \tag{4.8}$$

where $t_{1/2}$ is the half-life.

The measured efficiency plots for the BEGe detector have been constructed using various standards and are shown in Fig. 4.6. These include solid samples (soil) pressed pellets, LDP1, LDP3, UO_3 and the certified material of IAEA-312 provided by the International Atomic Energy Agency. IAEA material has similar container dimensions as the actual samples and it contains a mixture of gamma-emitting nuclides. These produce γ-rays over a wide range of energies (46 - 2000 keV). LD planar standards (LDP1 and LDP3) are samples from the Lake District in 1986 shortly after the Chernobyl accident [94]. These samples contain three gamma-ray energies of 46.5 keV from ^{210}Pb, 604 keV from ^{134}Cs and 662 keV from ^{137}Cs (P. Appleby, pers. comm). However the peak for ^{134}Cs was not identified since a long time has elapsed since the sources were calibrated (3rd May 1986) compared to its half-life ($t_{1/2}$ = 2.1 y). The sample of UO_3 contains a 1.61 g of Uranium trioxide that has been mixed with a 8.31 g of flour [94].

The characteristics of the standards used for experimental efficiency calibration are given in Table. 4.4. All these standards are with cylindrical geometry but different sizes. All the calibration measurements were made with standards placed directly on the cap of the detector. As can be seen from Fig. 4.6, variations in sample density and dimensions

play an important role for the efficiency mainly at lower energies (<100 keV). The effects of these parameters on the detection efficiency will be discussed in more detail in the later sections within this chapter.

Table 4.4: Radionuclides, activties and geometries used for comparing the experimental detection efficiency; [1] recommended values obtained from the reference sheet for the material(IAEA, 2000) with 95% Confidence interval of 15.7-17.4 and 81.3-101.5 for ^{238}U and ^{232}Th, respectively.

Standard	Radionuclide	Activity (Bq/kg)	Dimensions (Diameter, Thickness, Weight, Density)
LDP1	^{210}Pb	3386 ± 61	(4.4 cm, 0.5 cm, 4.38 g, 0.58 g/cm^3)
	^{137}Cs	3812 ± 111	
LDP3	^{210}Pb	3329 ± 60	(4.4 cm, 2.5 cm, 20.14 g, 0.53 g/cm^3)
	^{137}Cs	3856 ± 113	
UO_3	^{238}U	16656 ± 832	(4.4 cm, 0.65 cm, 9.92 g, 1.00 g/cm^3)
	^{235}U	771 ± 39	
IAEA-312[1]	^{238}U	16.5	(6.9 cm, 2.3 cm, 77.40 g, 0.90 g/cm^3)
	^{232}Th	91.4	

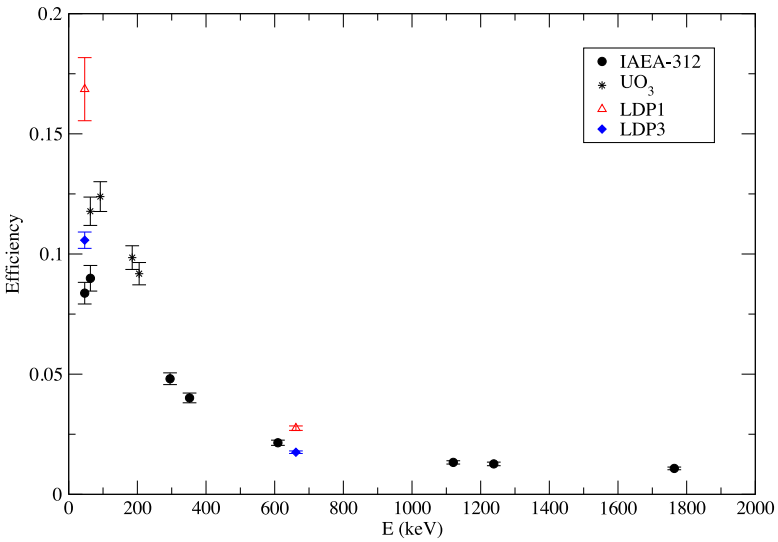

Figure 4.6: Experimental efficiency plots for BEGe detector from different standards (as described in the text).

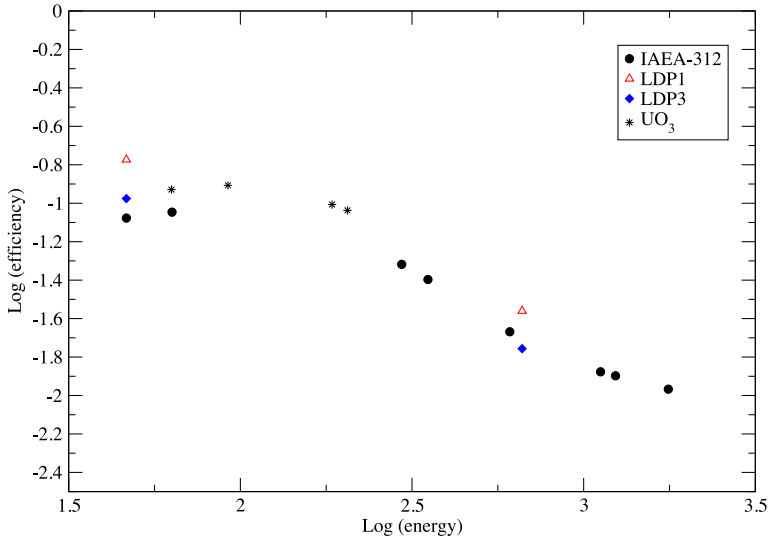

Figure 4.7: The same as Fig. 4.6 using log log scales.

4.3.2 Self-absorption corrections and low-energy efficiency

The accurate determination of the detector efficiency at low gamma-ray energies is crucial when investigating disequilibrium in environmental samples using gamma rays (46.5 keV from ^{210}Pb and 63.3 keV and 92.6 keV from ^{234}Th) that occur in the natural decay series [38]. These low-energy gamma rays are susceptible to the effects of self-absorption within the samples. The importance of the attenuation of photons has prompted many researchers to measure the attenuation coefficients using different methods [95, 96, 97]. This is particularly significant in measurements of composite materials such as soil and sediments where self-absorption corrections may vary due to density and compositional differences between the samples and the standard materials used for calibration [98]. The influence of gamma-ray self-absorption within a sample will impact on the efficiency calibration at low gamma-ray energy and corrections must be made. In this work a computational procedure for self-absorption correction was performed utilising the LabSOCS, which is discussed later. However, the experimental method described below was applied only to test the influence of self-absorption.

In order to carry out transmission measurements for standard and unknown samples, a set of four gamma-ray emitting point sources was used over an energy range of 32-121 keV.

For example to measure the transmission differences due to the lowest gamma-ray transitions in the decay series (46.5 keV and 63.3 keV), gamma-ray lines of 32 keV, 39 keV and 59.5 keV from ^{137}Cs, ^{152}Eu and ^{241}Am, respectively, were used. The point sources were positioned at a fixed distance from the detector window (10 cm). A lead collimator was positioned just under each source to get a nearly parallel photons beam. The sources used and their energy transitions used for these measurements are listed in Table 4.5. The measurements were accomplished by measuring the peak count rates due to these sources with and without the samples placed directly on the detector. This is illustrated schematically in Fig. 4.8. This procedure was developed initially by Los Alamos National Laboratory [99] and is widely used.

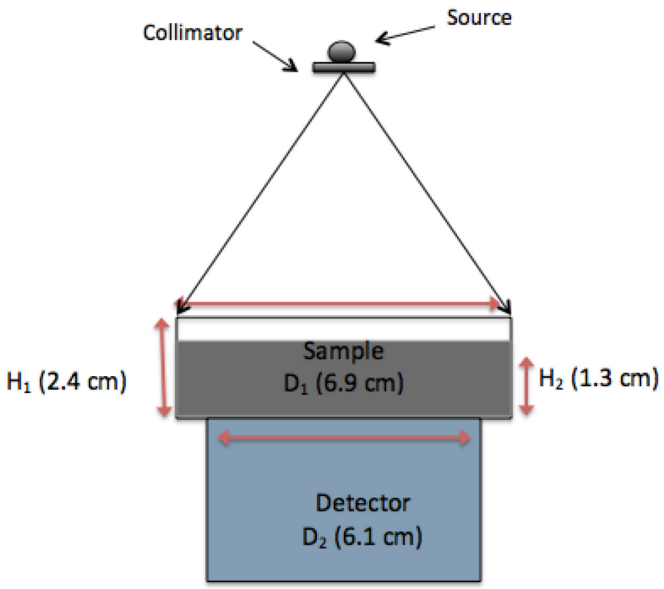

Figure 4.8: A schematic view of the measurement arrangment; D_1 the container diameter, D_2 the detector diameter, H_1 the container thickness and H_2 the sample thickness. Typical values are shown.

Table 4.5: List of sources and their gamma-ray energies used to correct for samples attenuation.

Source	E_γ(keV)
^{137}Cs	32
^{152}Eu	39
	121
^{241}Am	59
^{133}Ba	80

In general, the attenuation of γ-rays in a medium is given by

$$I = I_0 \exp(-\mu x), \tag{4.9}$$

where I_0 is the initial intensity of γ ray and I is the attenuated γ-ray intensity after passing through a medium of thickness x, and μ is the linear attenuation coefficient of the material [12]. The linear attenuation coefficient can be expressed in terms of the physical

Table 4.6: Gamma-ray transitions (I/I_0) for set of samples with different chemical compositions, densities and thickness for different photon energies.

Sample	Density (g/cm^3)	E_γ (keV)				
		32	39	59	80	121
Namibia(LV393)	1.47	0.13 ±0.02	0.27 ±0.01	0.50 ± 0.02	0.61 ± 0.02	0.69 ± 0.03
Kimberly(LV519)	1.49	0.13 ± 0.02	0.29 ± 0.01	0.52 ± 0.02	0.63 ± 0.02	0.70 ± 0.03
Czech Republic(LV390)	1.51	0.20 ± 0.02	0.32 ± 0.02	0.55 ± 0.02	0.65 ± 0.02	0.67 ± 0.03
Kimberly(LV520)	1.66	0.10 ± 0.02	0.26 ± 0.01	0.52 ± 0.02	0.65 ± 0.02	0.68 ± 0.03
Namibia(LV396)	1.81	0.09 ±0.02	0.23 ± 0.01	0.51 ± 0.02	0.61 ± 0.02	0.68 ± 0.03

density (ρ) of the medium by

$$\mu = \frac{\mu}{\rho} \cdot \rho = \mu_m \rho, \tag{4.10}$$

where μ_m is known as the mass attenuation coefficient, which is a constant value for particular element or compound. The units of linear and mass attenuation coefficients are cm^{-1} and $cm^2.g^{-1}$, respectively. The transmission of gamma-ray photons is measured from the intensity ratios (I/I_0).

The experimental results were validated by comparing with LabSOCS computed values for the same gamma-ray photons and the same experimental setup. This is presented later in Section. 4.4.

Table 4.6 and Fig. 4.9 show the values obtained for transmitted intensities for gamma-ray photons for different samples with different thickness, densities and chemical compositions. As can be seen, the variations are not negligible. This emphasizes the need to use the same matrix for the samples under measurement rather than replacing with standard materials which may have different densities and compositions. Note that these are the same samples to be used for the measurements described later in chapter4.

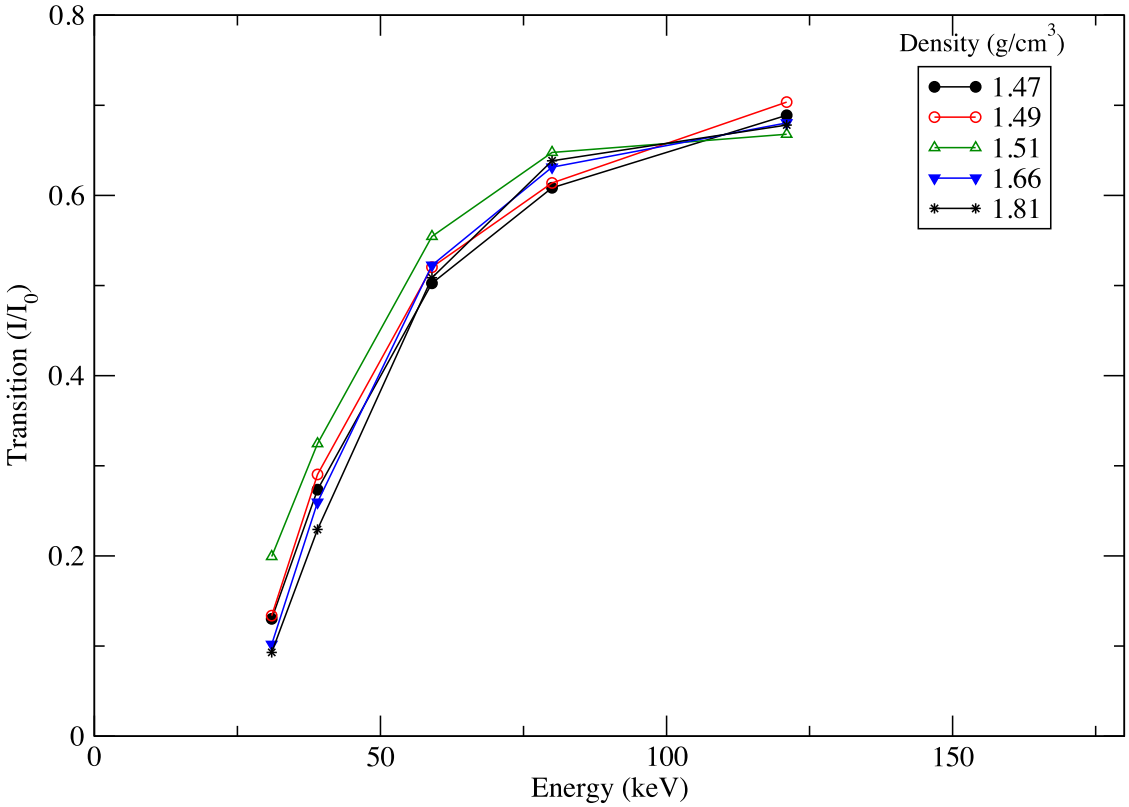

Figure 4.9: A plot for gamma-ray transition data presented in Table 4.6.

4.3.3 Determination of the sample's chemical compositions

In order to compute the efficiency of the detector at each gamma-ray energy using LabSOCS software, the chemical composition for the measured samples has to be determined. For this purpose the system of X-ray fluorescence (XRF), which is located in the School of Environmental Science at the University of Liverpool was utilized. Fig. 4.11 shows this system and containers prepared for some of measured samples. Prior to XRF measurements, the samples were powdered finer than 50 μm using the Planetary Ball Mill Instrument (Fig. 4.10). The description of XRF technique will not be discussed in this work, however it has been explained in detail in several references [100, 101, 102]. The only elements

that were entered into LabSOCS for efficiency calculations are those with a percentage larger than 0.01 in the samples. The chemical compositions for all the measured samples are listed in the tables below.

Figure 4.10: Planetary Ball Mill Instrument used to prepare the samples for XRF analysis.

Figure 4.11: The X-ray fluorescence system and some of the analysed samples.

Table 4.7: The chemical compositions for the samples from Namibia.

Elements (%)	LV393	LV395	LV396	LV398	LV523	LV524
O+C (calc)	54.29	54.66	53.25	53.36	56.19	56.00
Si	20.13	20.49	20.37	20.39	22.48	18.92
Al	2.28	2.26	2.50	2.50	1.54	2.13
P	0.03	0.04	0.05	0.05	0.05	0.04
S	0.09	0.09	0.10	0.10	0.00	0.00
Ca	16.88	16.90	15.88	15.94	17.49	19.34
Mg	2.71	2.63	2.61	2.59	2.48	3.21
Cl	0.39	0.44	0.38	0.40	0.07	0.00
Na	3.71	3.65	3.89	3.88	2.42	2.24
K	1.50	1.49	1.40	1.38	0.76	0.91
Fe	0.69	0.63	0.61	0.63	0.52	0.75
Mn	0.02	0.04	0.03	0.03	0.02	0.02
Ba	0.16	0.16	0.16	0.16	0.11	0.12
Sr	0.22	0.22	0.22	0.22	0.20	0.18
Zr	0.01	0.01	0.01	0.01	0.01	0.01

4.3.4 Efficiency calibration with LabSOCS

Standard sources with the same geometry and composition as the measured samples might not be available for every laboratory. As a result, the development of an alternative cal-

Table 4.8: The chemical compositions for the samples from Australia.

Elements (%)	LV519	LV520	LV521	LV522
O+C (calc)	48.88	51.51	51.53	51.63
Si	32.97	39.69	39.69	39.77
Al	5.81	5.44	5.43	5.43
P	0.03	0.00	0.00	0.00
S	0.01	0.00	0.00	0.00
Ca	1.50	0.18	0.18	0.19
Mg	1.37	0.60	0.62	0.62
Cl	0.03	0.05	0.05	0.04
Na	1.00	0.07	0.06	0.06
K	1.95	0.91	0.91	0.93
Fe	4.19	1.21	1.23	1.23
Mn	0.04	0.01	0.01	0.01
Ba	0.03	0.01	0.01	0.01
Cr	0.01	0.00	0.00	0.00
V	0.01	0.00	0.00	0.00
Rb	0.01	0.00	0.00	0.00
Sr	0.01	0.00	0.00	0.00
Zn	0.01	0.00	0.00	0.00
Zr	0.03	0.01	0.01	0.01

Table 4.9: The chemical compositions for the samples from Czech Republic.

Elements (%)	LV389	LV390	LV391
O+C (calc)	51.90	51.72	51.77
Si	41.54	40.81	40.89
Al	3.27	3.73	3.79
P	0.01	0.03	0.03
S	0.01	0.02	0.01
Ca	0.28	0.30	0.27
Mg	0.45	0.48	0.48
Cl	0.04	0.04	0.03
Na	0.50	0.69	0.53
K	1.30	1.32	1.32
Fe	0.85	0.99	1.03
Mn	0.02	0.02	0.02
Ba	0.03	0.02	0.03
Rb	0.01	0.01	0.01
Sr	0.01	0.01	0.01
Zr	0.02	0.02	0.02

ibration procedure is of importance. This innovative method for constructing efficiency curves uses Canberra Genie 2000 module LabSOCS (Laboratory Sourceless Object Calibration Software). This software calculates the gamma-ray efficiency for a characterized detector and particular geometry based on input parameters, which are provided by the user (e.g., sample dimensions, densities, distance to detector, etc). All input parameters for the sample and detector are stored and a report for efficiency calibration is performed once the user runs the software.

Once the chemical compositions and physical dimensions for the measured samples have been determined, LabSOCS has been the primary method for efficiency calculation used within this thesis. Although the detector characterizations were defined and validated by the manufacturer, validation of LabSOCS has been performed within this project (section 4.4) in order to ensure that the results of this analysis is reliable. The detector manufacturer, Canberra, performed a set of measurements using test sources in very well-defined geometries to characterize the Ge detectors response and validate the accuracy of the mathematical calibration [103]. These characterizations allow efficiencies to be extracted for a known sample container, sample and absorber matrix, and a specific source-to-detector geometry using the Genie 2000 Geometry composer [103]. In the next two sections I will discuss the effects of density, elemental compositions, sample thickness and diameter on the detection efficiency.

4.3.5 Density and elemental composition effects

The self absorption of low gamma-ray energies varies as a function of the physical and chemical properties of the sample. To show the effects of density and composition on detection efficiency, the full-energy peak efficiencies were modelled using LabSOCS software for the characterized BEGe-2825 detector for some different environmental samples. Two of the measured samples are presented here to show the effects of density variation on the detection efficiency. The actual density for these samples was calculated using the total weight of each sample (without the container). The variation of the density of each sample was within the range of the actual density for all the measured samples. The aim

of the hypothetical variation in the sample density in LabSOCS input was to examine the influence of the sample density on the detection efficiency. As can be seen from Fig. 4.12 and Fig. 4.13, the absorption of low-energy gamma rays (<100 keV) is greater for higher densities of material leading to a lower detection efficiency over this range. It can be shown also that a variation in the sample density by an interval of 0.13 g/cm^3 can vary the efficiency by up to 3% at low-energy gamma rays (<100 keV). However, this decreases for the intermediate gamma-ray energies (>200 keV) to less than 1.5% depending on the sample chemical compositions.

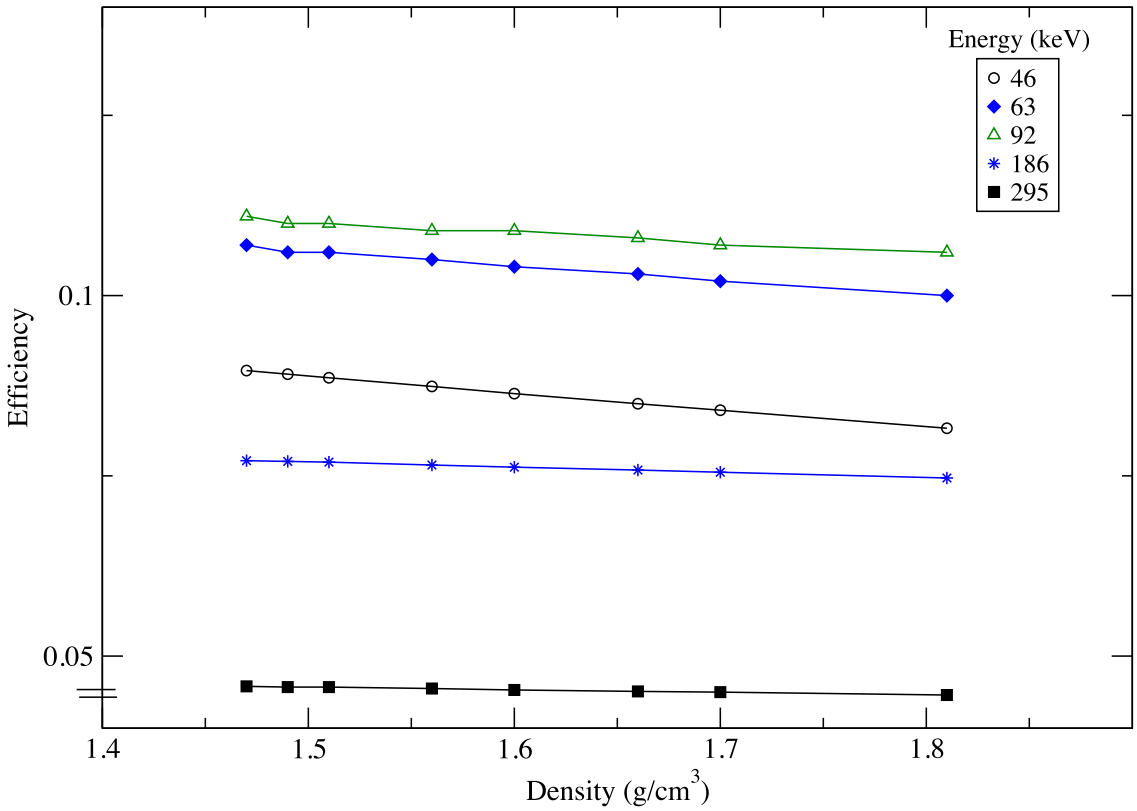

Figure 4.12: Modelled efficiencies for one of the realistic samples (LV396) with varied density and constant thickness and chemical compositions.

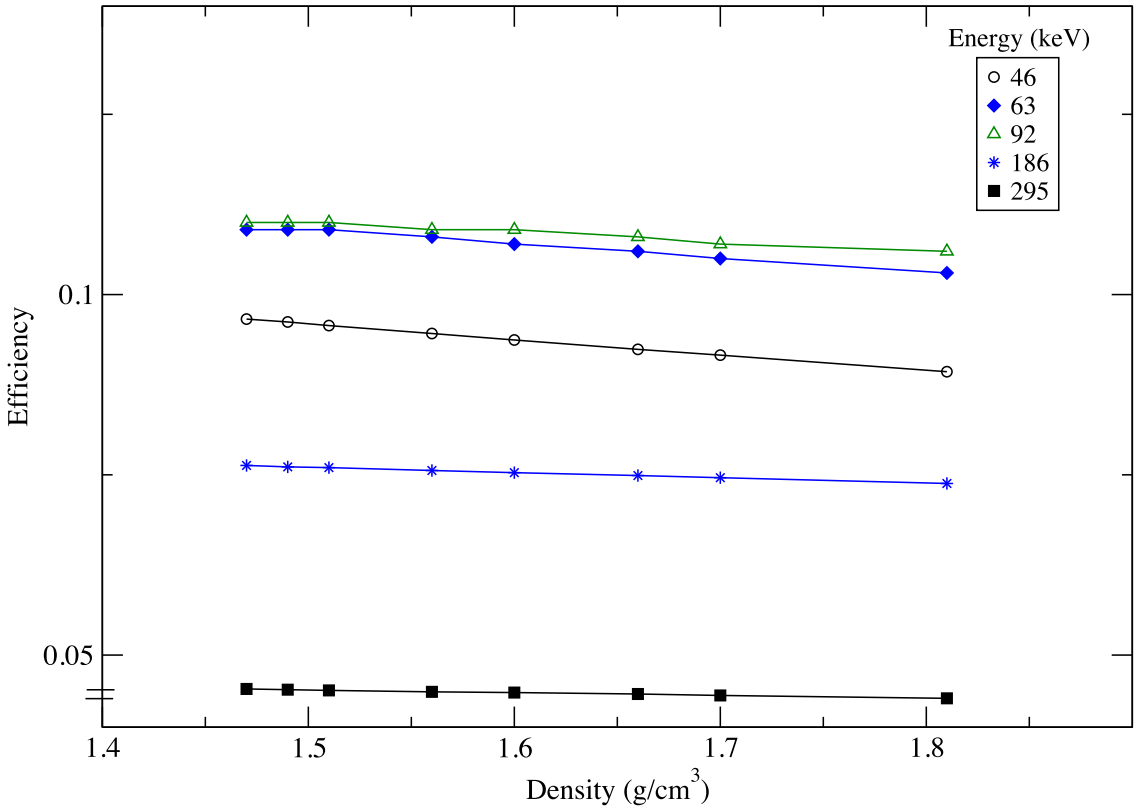

Figure 4.13: Modelled efficiencies for one of the realistic samples (LV389) with varied density and constant thickness and chemical compositions..

For the investigations of the influence of composition effects, a container similar to the measured sample's geometry, with a diameter of 69.1 mm and a height of 14.6 mm was used. This container was filled with the actual samples compared with different material labelled as Dirt1, Dirt2 and Drydirt (Fig. 4.14 and Fig. 4.15). These material are soil type stored as default in LabSOCS software and their chemical compositions are described in Table 4.10.

Table 4.10: Chemical compositions (%) for LabSOCS default material used in Fig. **??** and Fig. 4.14.

Material	Chemical elements	(%)
Dirt1	H	2.20
	O	57.50
	Al	8.50
	Si	26.20
	Fe	5.60
Dirt2	H	1.10
	O	55.80
	Al	7.20
	Si	31.10
	C	1.20
Drydirt	H	0.36
	O	49.62
	Al	7.10
	Si	27.38
	Fe	4.04
	C	2.14
	Na	0.84
	Mg	1.60
	K	2.37
	Ca	4.21
	Ti	0.34

The presence of Calcium and other elements (Mg and Fe) has a strong effect especially on the attenuation of lower-energy gamma rays. This can be seen from the plots of the detection efficiency variation with the chemical compositions for two of the actual samples (LV396 and LV389) which are indicated in Fig. 4.14 and Fig. 4.15. These show the effects of the variation in chemical composition in the energy range of <150 keV. As can be seen from the plots, the efficiency is mostly influenced by the variation in the sample chemical compositions at low energy gamma rays (<100 keV) and in Fig. 4.14 the presence of heavier elements in the samples (Dirt1 and Drydirt) decreased the detection efficiency at 46 keV and 63 keV gamma rays by about 9% relative to the material of Dirt2. A similar picture is shown in Fig. 4.15. Therefore, performing the efficiency calibration for the measurements of environmental samples requires the chemical compositions for the measured samples to be known.

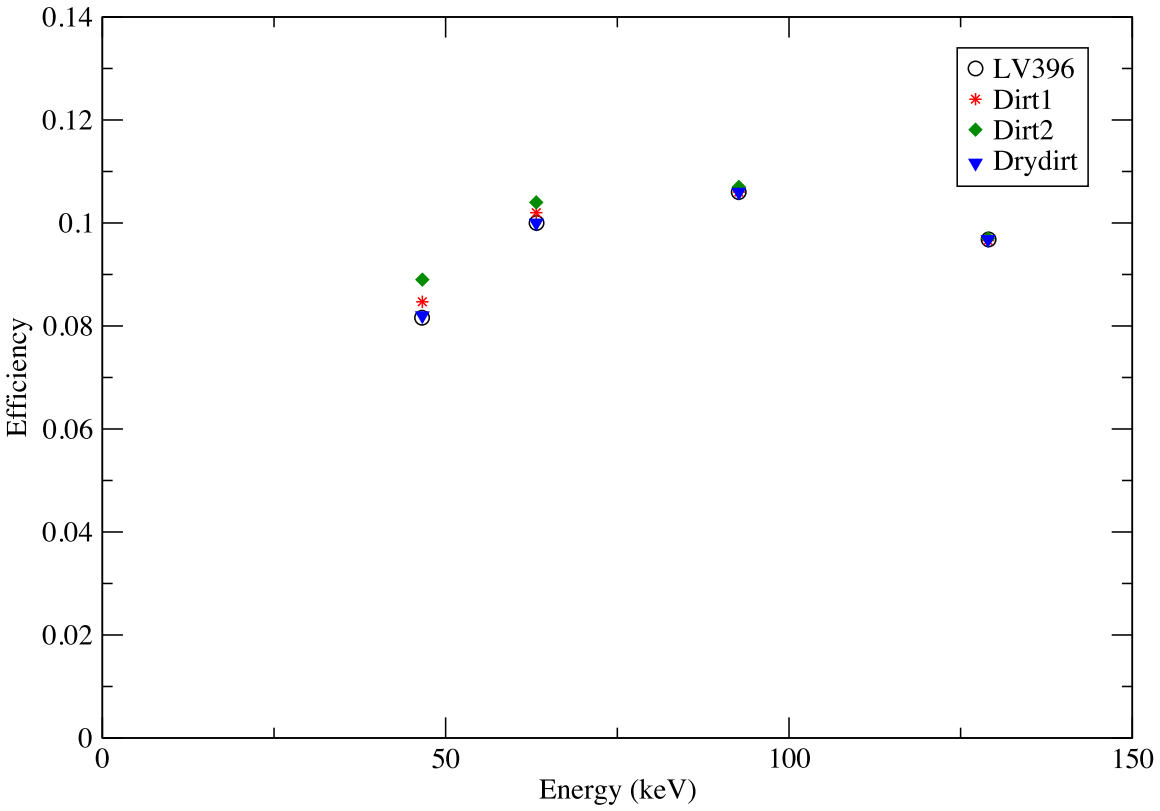

Figure 4.14: Modelled efficiencies with varied chemical compositions and constant thickness and density compared with LV396 sample (Table. 4.6), which is used for measurements in the present work.

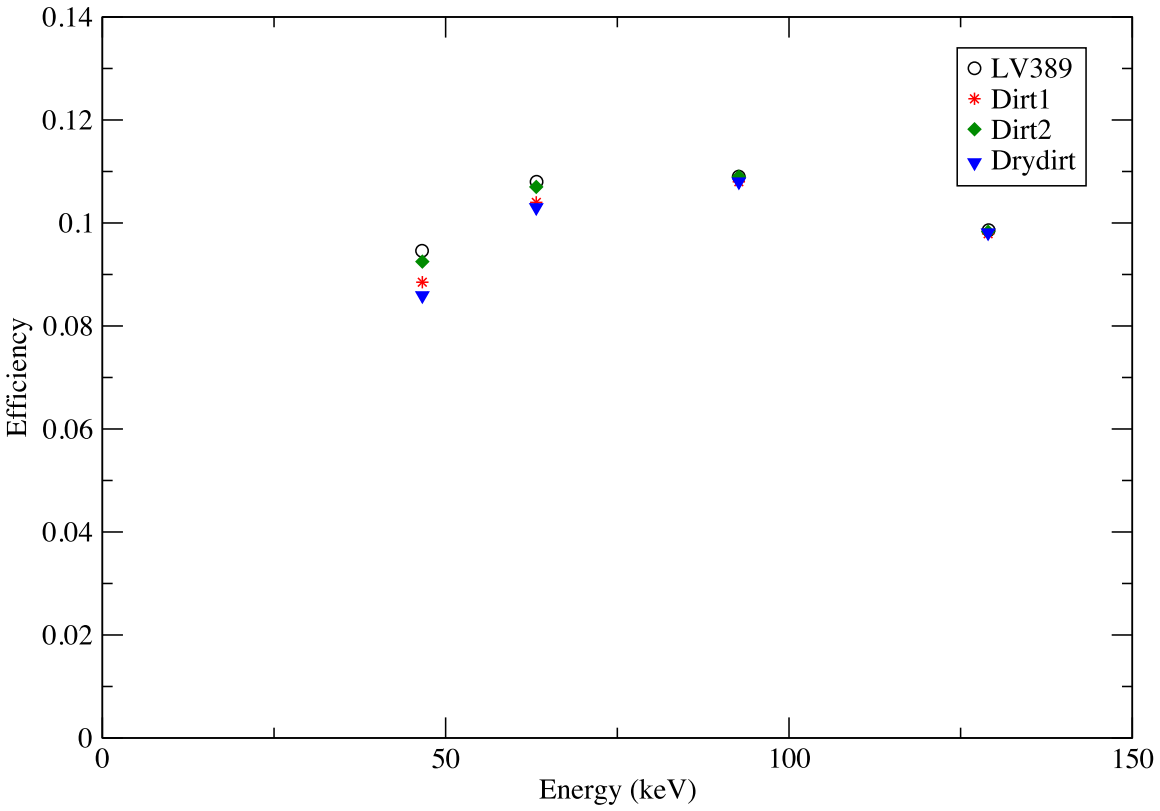

Figure 4.15: Modelled efficiencies with varied chemical compositions and constant thickness and density compared with LV389 sample, which is used for measurements in the present work..

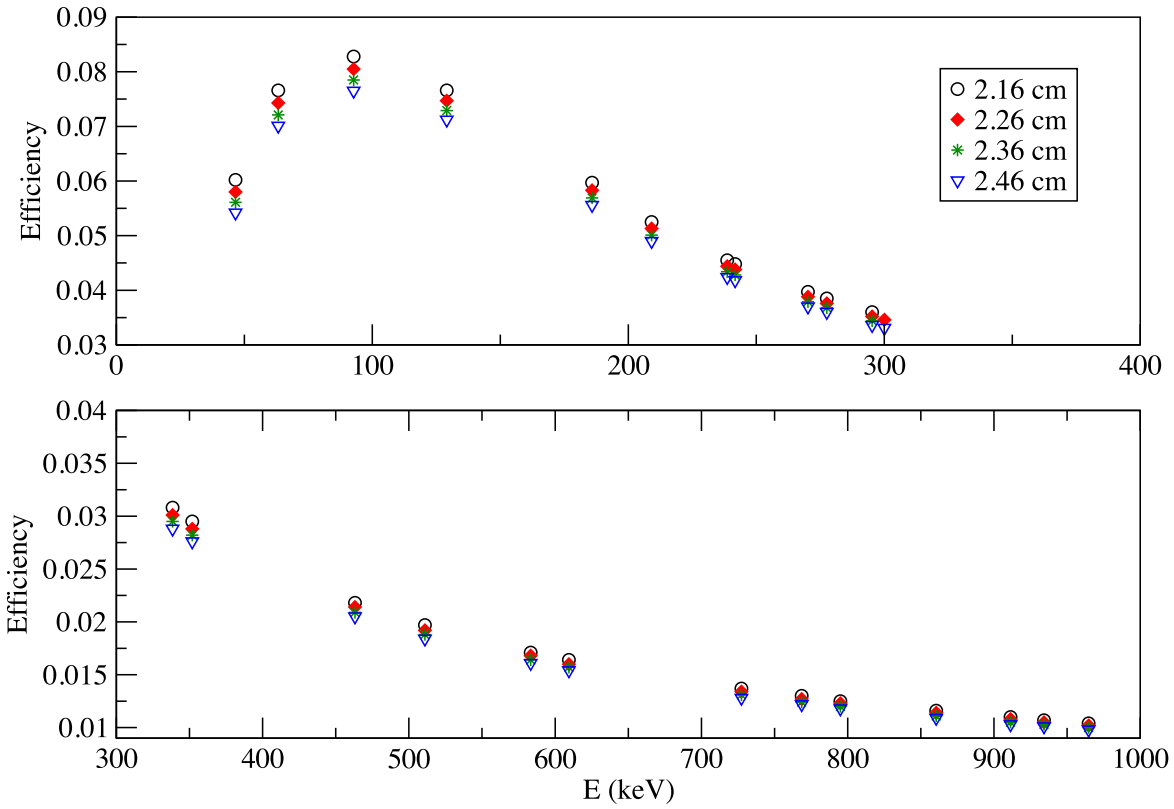

Figure 4.16: Varying the efficiency with the sample thickness in the energy range from 46 -1000 keV.

4.3.6 Thickness and diameter effects

Variations in sample thickness also have a significant influence and can contribute to uncertainty in the detection efficiency. To investigate the effect of this parameter, the full-energy peak efficiencies were modelled using LabSOCS software for a geometry by varying the sample height in 1 mm intervals. This geometry includes a realistic sample in a plastic container of 69.1 mm diameter and 1.05 g.cm^{-3} density. Fig. 4.16 shows up the efficiency plots for varying the efficiency with the sample thickness in the energy range from 46 -1000 keV.

Repeated measurements for the actual sample thicknesses (6 readings) have been taken

to deduce the mean and standard deviation for each sample and subsequently the uncertainties on the detection efficiency. The LabSOCS software was used to produced efficiency calibrations using the mean thickness and the thicknesses corresponding to the upper and lower uncertainty values about the mean. These calculations provide an estimate of the uncertainty in detection efficiency as a function of gamma-ray energy. Table 4.11 indicates some of the sample's thicknesses and the parameters used to determine the uncertanties on the detection efficiency. Using this procedure, the efficiency uvariation on low-energy gamma rays (<100 keV) due to sample thickness variations was around 7% and decreased for the intermediate energy gamma rays (5%) and less for higher gamma-ray energies. Figure. 4.17 shows the efficiency plots for one of the measured samples (LV396) for each thickness value.

Table 4.11: Parameters in bold entered to LabSOCS for uncertainty estimates.

Sample	LV393	LV395	LV396	LV398
Thickness (cm)	1.34	1.375	1.42	1.27
	1.44	1.15	1.26	1.58
	1.62	1.47	1.59	1.18
	1.25	1.26	1.15	1.41
	1.42	1.31	1.09	1.28
Average	**1.45**	**1.29**	**1.32**	**1.31**
STD	0.16	0.11	0.17	0.16
Average + STD	**1.61**	**1.41**	**1.50**	**1.47**
Average - STD	**1.30**	**1.19**	**1.13**	**1.15**

Although the diameter can be determined more accurately compared with the sample's height, the effects of the sample diameter were also investigated following the same procedure described above. As can be seen from Fig. 4.18, there is less than 3% variation for the detection efficiency of low-energy gamma rays as a function of the sample diameter whereas, negligible differences can be seen on intermediate and high gamma-ray energies. This indicates that the sample diameter is less influential on the efficiency uncertainty than other parameters.

Using LabSOCS modelled efficiencies provides a very promising approach for the measurement of environmental samples such as sediments originating from different envi-

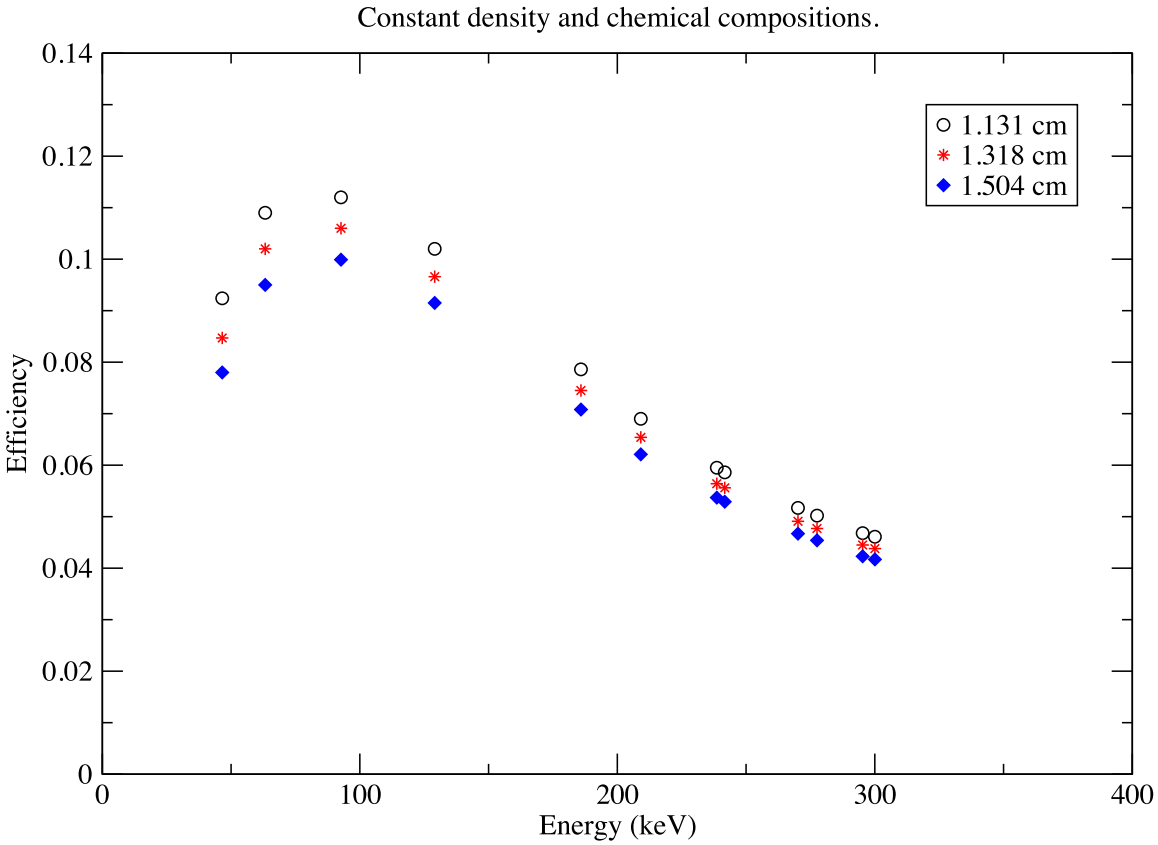

Figure 4.17: Varying the efficiency with the sample thickness in the energy range from 46 - 300 keV for LV396 sample.

ronments and different sources with variable compositions and densities. Moreover, the amount of sample available sometimes varies even within a single core, depending on core section length, water content or previous consumption of part of the sample for different analyses. The lack of standard sources that have similar physical parameters and chemical compositions to the measured samples can also be a challenge to perform specific analysis in the absence of this software.

In general, the uncertainty in the efficiency calculation is given in the LabSOCS Validation and Verification Manual based on comparison of a number of tests with different geometries [104]. The recommended values are given in [103]. The results obtained in

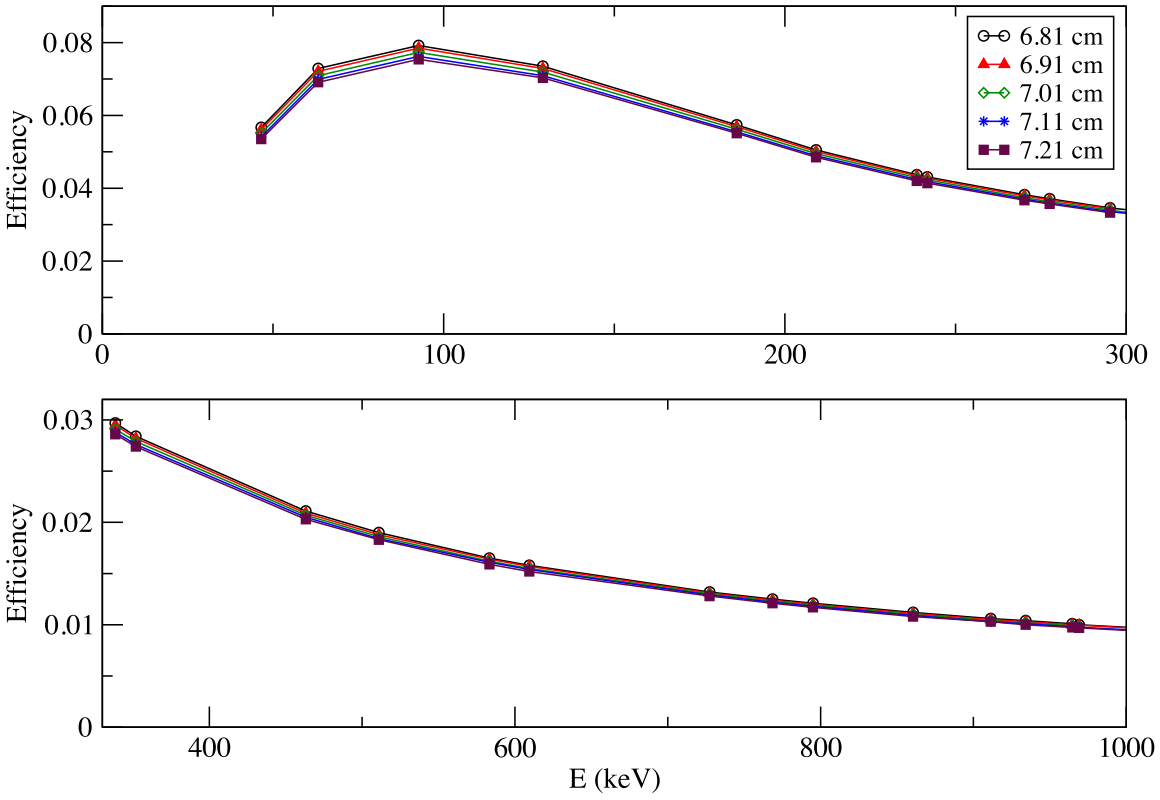

Figure 4.18: Varying the efficiency with the sample diameter in the energy range from 46 -1000 keV.

this work by varying the physical properties and chemical compositions for the measured samples were within the range of the recommended values and used for all the activity calculations. As an example Figure. 4.19 shows the efficiency plots for two of the measured samples as indicated.

Table 4.12: Recommended uncertainties for LabSOCS efficiencies [103].

Energy range (keV)	Rel. Std. Dev %
< 150	7.1
150-400	6.0
400-7000	4.3

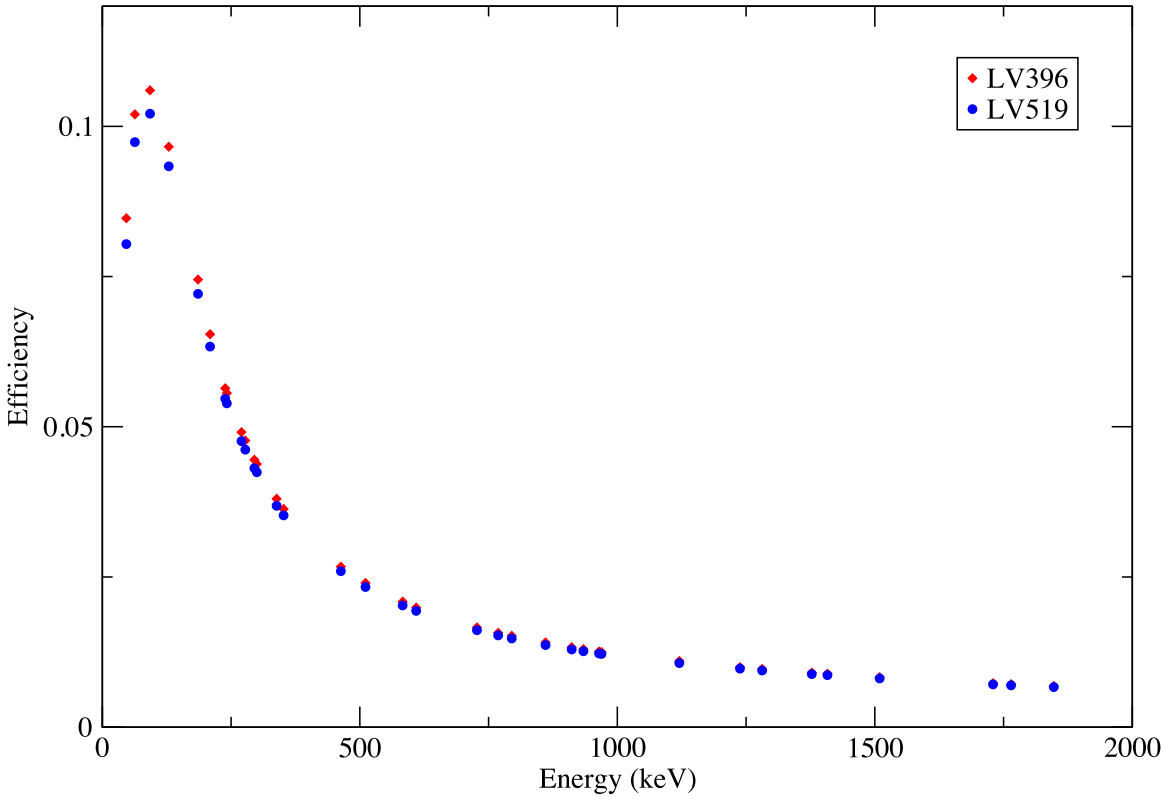

Figure 4.19: Modelled efficiency plots for two of the measured sample.

4.4 Validation of LabSOCS

The accuracy of the calibration method using LabSOCS software has been validated by other users using a variety of methods. Several procedures and data comparison tests have been proposed [103] by which LabSOCS proved to be consistent and better than source-based methods. To validate the present results obtained for the detection efficiency from the LabSOCS software and test how they are consistent with the experimental results, two measurements were carried out. The first one is based on comparing the modelled and experimental efficiency for the LDP1 standard described in Table 4.4. The second one was done by transmission experiments based on different point sources with a range

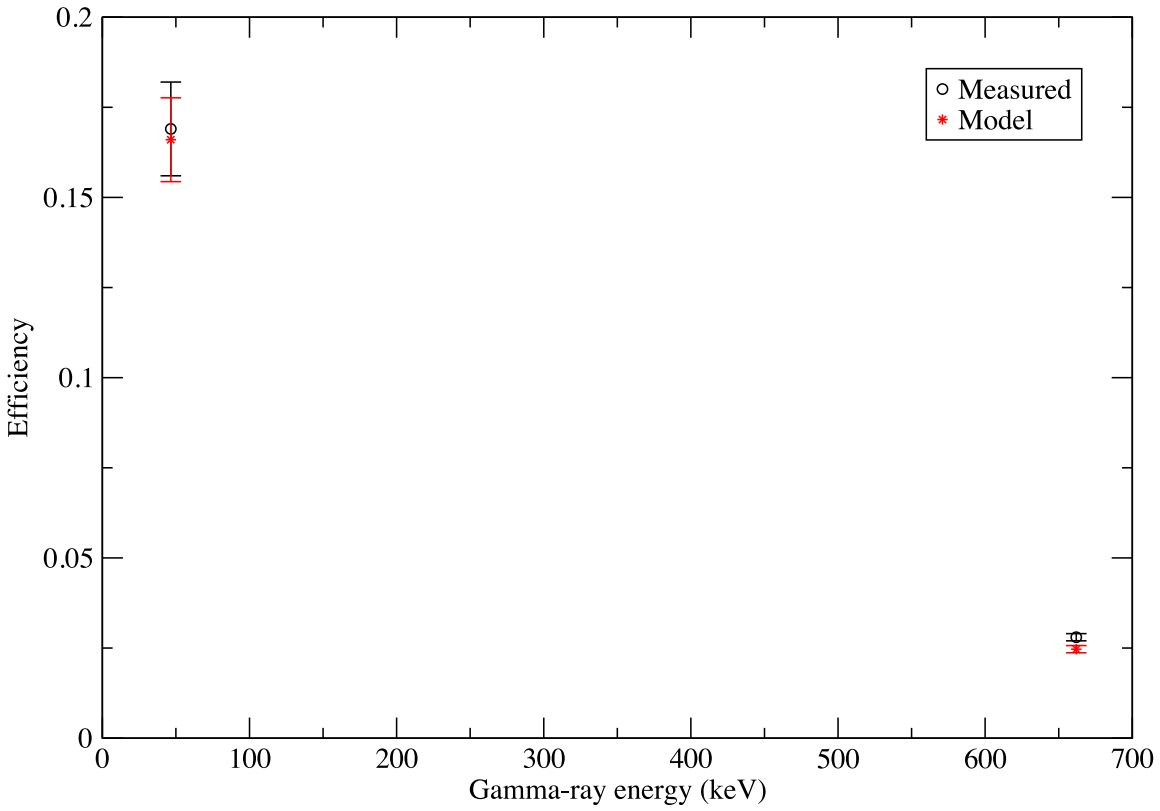

Figure 4.20: Measured and model efficiency data points from ^{210}Pb and ^{137}Cs from the calibrated source LDP1.

of gamma-ray energies of 32 to 121 keV (see Table 4.5). These sources were placed on a fixed distance from the detector using the actual samples as absorbers in the experiment arrangements.

Figure. 4.20 and Table 4.13 present the modelled and measured efficiency values for the two radionuclides of ^{210}Pb and ^{137}Cs, where a good agreement can be seen between the two efficiency values for both low and high energies.

Fig. 4.20 shows a plot for the efficiency results in Table 4.13. The error values applied on the modelled efficiency were deduced from the results above (7% for 46.5 keV and 4% for 661.7 keV).

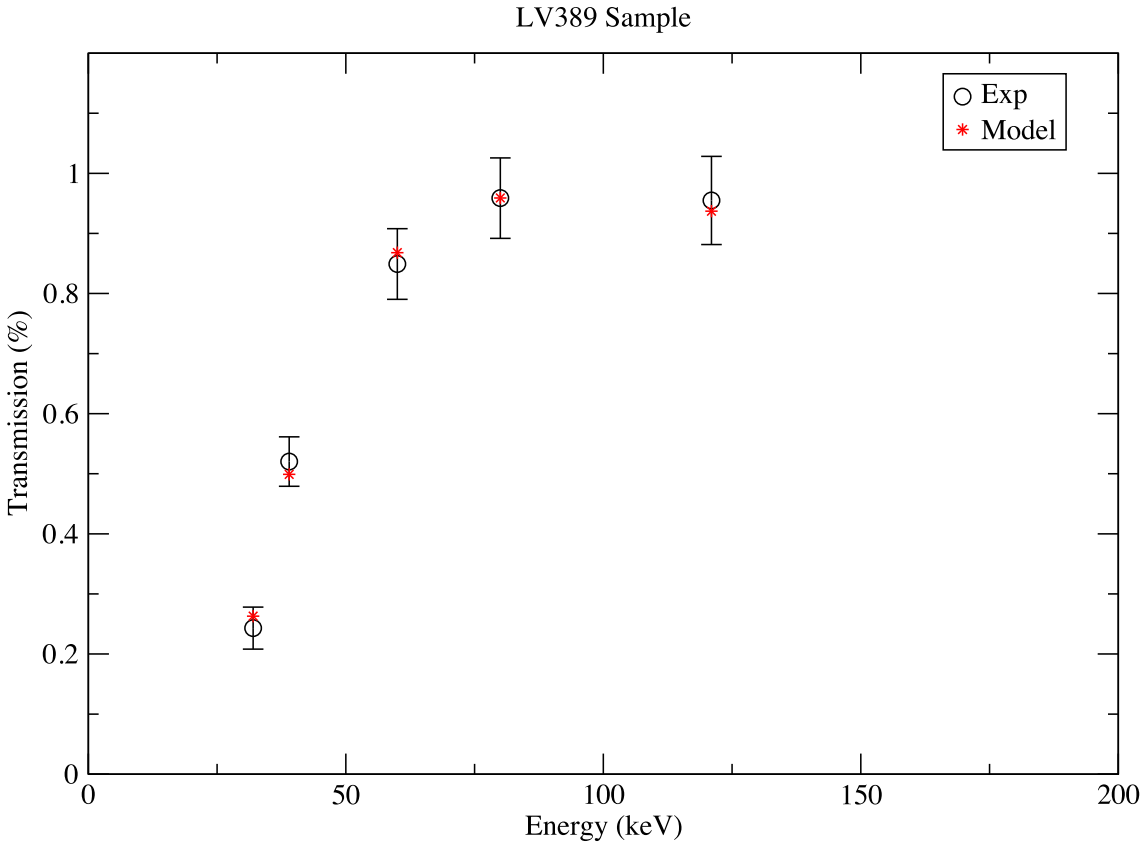

Figure 4.21: A comparison between experimental attenuation measurements normalised to modelled results for LV389 sample; the presented errors are due to the experimental results.

The transmission experiment was carried out using the point sources indicated in Table. 4.5. This includes placing each point source at a fixed distance of 10 cm from the

Table 4.13: Modelled and measured efficiency for 46.5 keV and 662 keV gamma energies from LDP1 standard source described in Table 4.4. Uncertainty on the model is based on the variation results discussed above.

E_γ (keV)	Experimental	Model
46.5	0.168 ±0.013	0.166±0.012
661.7	0.028 ± 0.001	0.025± 0.001

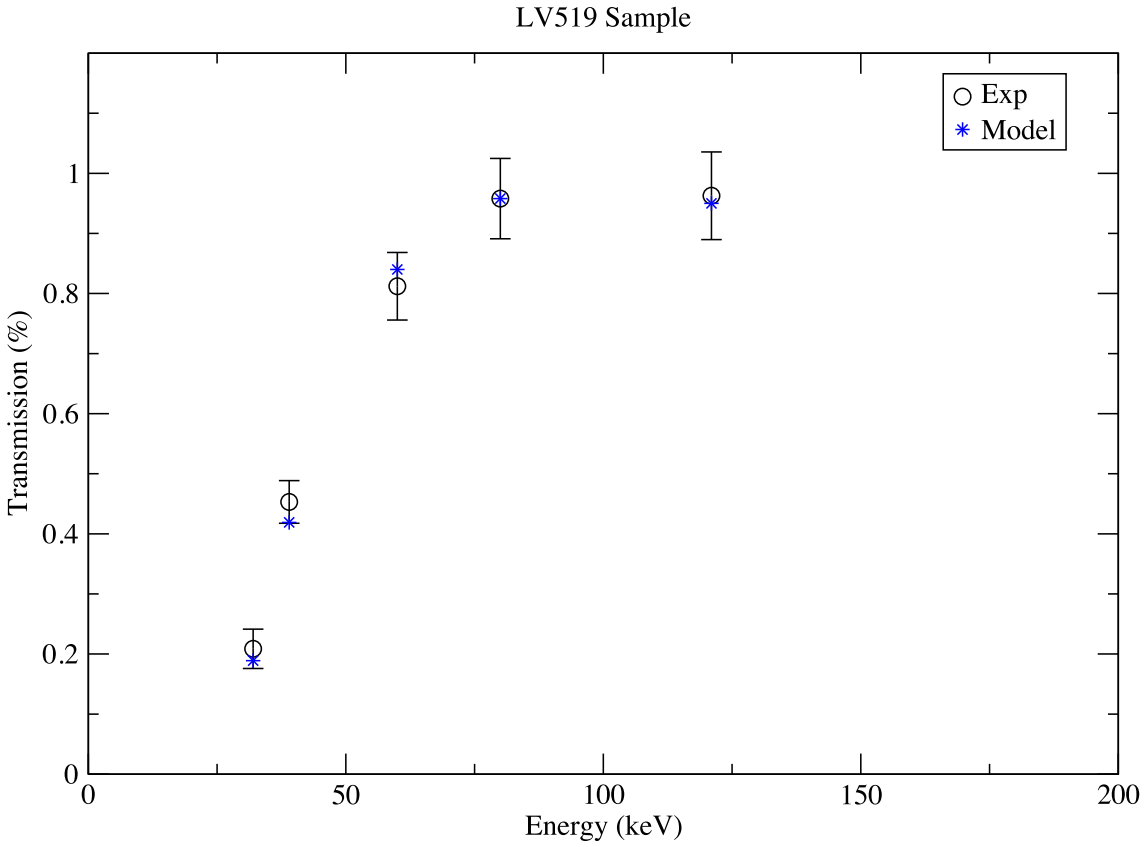

Figure 4.22: A comparison between experimental attenuation measurements normalised to modelled results for LV519 sample; the presented errors are due to the experimental results.

detector cap and measuring the transmission with and without the actual samples (as an absorber). These measurements were then performed with the same settings with LabSOCS software. Fig. 4.21 and Fig. 4.22 demonstrate that there is a good agreement between the experimental and modelled results within the uncertainty.

The comparison of the detection efficiency calculated using LabSOCS to the source base method was also performed by other researchers. Figure. 4.23, for example shows the efficiency curves from their work generated for sources with identical chemical compositions and different thicknesses. As can be seen from Fig. 4.23, the efficiency curves obtained from

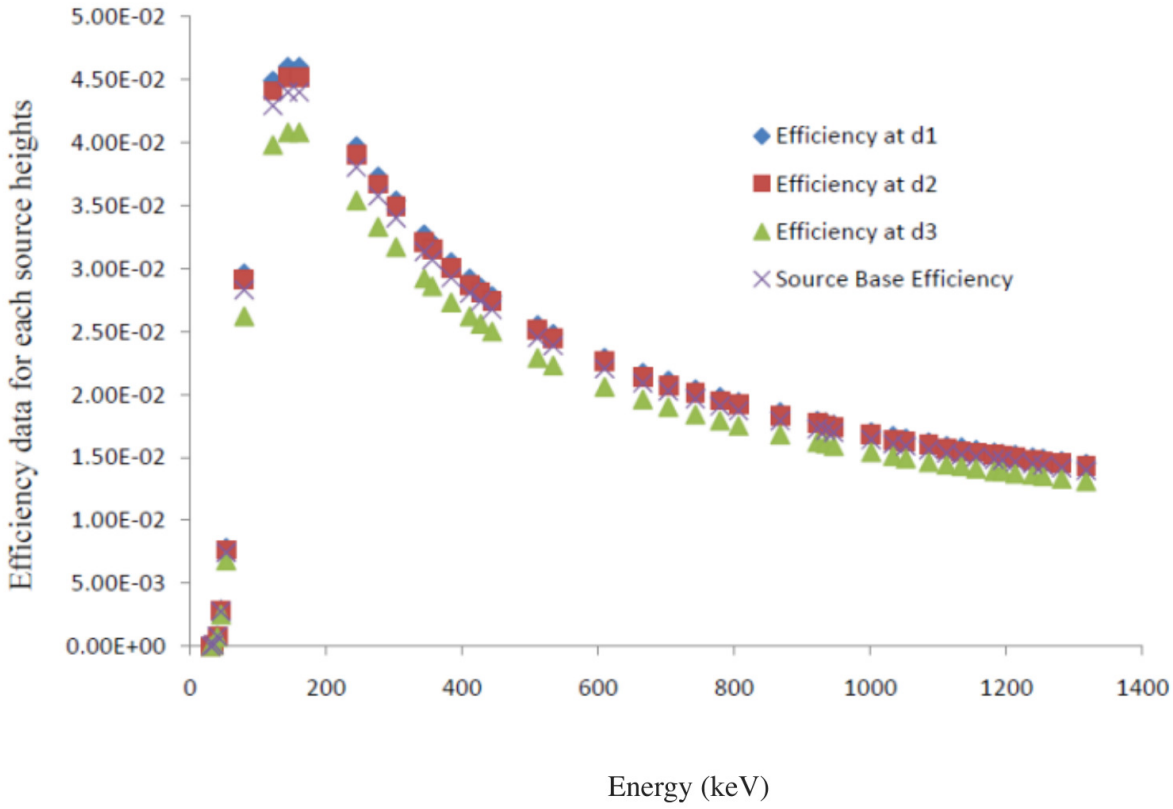

Figure 4.23: Modelled efficiency data points for standard material with different thicknesses (d1=10.04 cm, d2=10.22 cm and d3=11.25 cm) compared to measured effieincy (source base efficiency) [105].

the LabSOCS and the source base shows that all the data points approximately agreed with +96.3% confidence intervals relative to the source height of 10.22 cm (d2) [105].

4.5 Conclusion

Although the uncertainties for the efficiency calibrations can be high for low energies, the modelled efficiency calibration using LabSOCS has the advantage of greater freedom in modelling the efficiency for samples of varied matrices and geometries. This method is better than conventional procedures based on source calibrations even with the availability of carefully manufactured sources [103].

The series of measurements performed during the LabSOCS validation showed that the mathematical procedure is accurate and can be adapted for efficiency calibration for samples with different matrices and geometries. This can be seen clearly from the results obtained with the validation test for the actual samples and the small volumetric standards containing ^{137}Cs and ^{210}Pb radionuclides, where the measured values are in an excellent agreement with the modelled values. To conclude, the errors associated with the detection efficiency are up to 7% for low-energy gamma rays from all the parameters. However, these errors decrease with increasing gamma-ray energies to as low as only 3%. These are the values that will be assigned to the efficiency element used for calculating the radionuclides activities within this work.

Chapter 5

Environmental aspects and activity determinations

5.1 Sample collection and preparation

In order to identify radioactive disequilibrium in uranium-series decay, geological samples should be measured. For this purpose, samples from the following locations were selected: the Cambridge Gulf in Western Australia, the Etosha Pan in Namibia (South Africa), the Martinick Potok in the Czech Republic (Central Europe) and South Germany. Fourteen samples in total were analysed in these measurements. Four of these samples originate from river deposits from Northwest Australia (Cambridge Gulf region) (Fig. 5.1). This site is characterised by tropical climate with high temperatures and pronounced wet and dry seasons. Six samples originate from the Etosha Pan and shoreline deposits, which are dry lakes, situated in Namibia, in South-Western Africa (Fig. 5.2). Three samples were collected from the Czech Republic in central Europe and one from South Germany (Fig. 5.3). Each sample from the mentioned sites was collected from a single location. The details and geographical areas of the samples are listed in a table in Appendix A (Table. A.1). The reason for selecting theses sites is to investigate potential climate change. Samples from Namibia, for examples have been studied by other researchers to investigate the link between lake-level change and records of late Pleistocene and Holocene climate

change [106].

Sample preparation was carried out by placing each sample in an oven for drying at a temperature of 105 ^{0}C until a constant weight was reached, thus ensuring complete removal of any residual moisture. The samples were packed in containers with a cylindrical geometry with 6.9 cm diameter and varied height. Containers were then sealed with an electrical tape after spreading a small amount of silicon grease around the top edge of the container to prevent the escape of radon. The container then labeled with the weight and ID code of the sample and stored for at least one month prior to measurements in order to attain radioactive secular equilibrium between ^{226}Ra and its short-lived progeny ($>$ 7 half-lives of ^{222}Rn). Fig. 5.4 illustrates an example for one of the prepared samples (LV398). Care must be taken in the sample preparation in terms of the sealing procedure in order to obtain accurate results (particularly for ^{226}Ra). One must ensure that ^{222}Rn, the gaseous daughter of ^{226}Ra does not escape from the container. Any migration of ^{222}Rn gas will lead to spurious results since the ^{214}Bi and ^{214}Pb daughters will be in a state of disequilibrium [31]. Based on this work it is expected that the Namibia samples may not be in secular equilibrium. These samples are discussed in more detail in chapter6. The samples from the Czech Republic, South Germany and Northwest Australia are expected to be in secular equilibrium.

5.2 Calculation of the minimum detectable level

Evaluating the detection limit of an analytical system is the first step in data analysis. If low counting statistics have been recorded from low-level gamma-ray measurements, it is difficult to decide they are significant. The Minimum Detectable Activity (MDA) is the level of activity may be detected with a specified confidence level [81]. There are two limits that are significant to be introduced for the activity measurements. The critical limit (L_c) which is defined as the count above which we can state, with a certain level of confidence, that the net counts measured from the sample is significant and not consistent with zero and can be obtained in terms of the standard deviation in the background (σ_B) by the equation [81].

Figure 5.1: The locations of the four samples of LV519, LV520, LV521 and LV522 on the map of Australia. This map was created using Google Earth.

Figure 5.2: The locations of six samples that were found in disequilibrium on the map of Namibia in South Africa. This map was created using Google Earth.

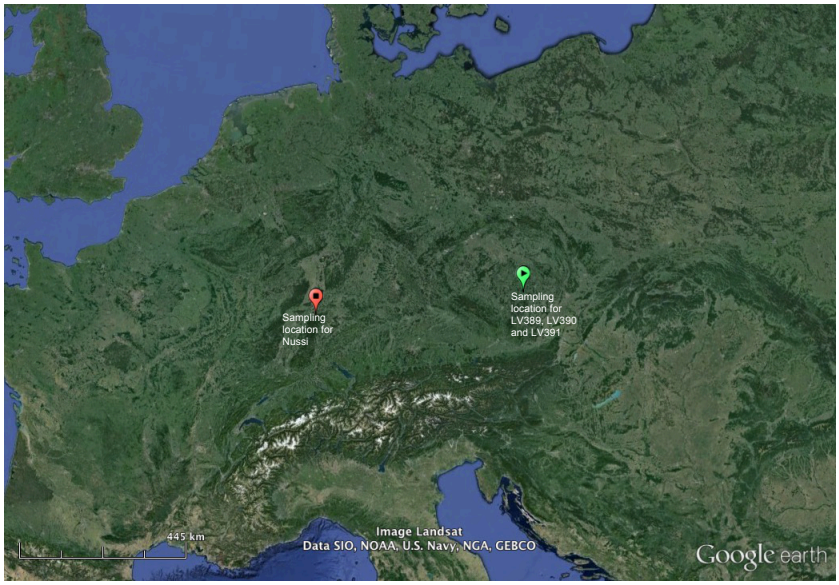

Figure 5.3: The locations of four samples of LV389, LV390, LV391 and Nussi on the map of Czech Republic and south Germany in Europe. This map was created using Google Earth.

Figure 5.4: A prepared sample filling in a cylindrical container and sealed.

$$L_c(cps) = 2.33\sigma_B \tag{5.1}$$

The second limit that it is necessary to determine is the detection limit (L_D), which is defined as the expected net count from the sample at which we can state with a certain level of confidence, that we will record as a significant count, i.e. a count above the critical limit. The detection limit for a measurement of a sample can be obtained by [59, 81, 107]

$$L_D(counts) = 2.71 + 4.65\sigma_B \tag{5.2}$$

These two limits are with a confidence level of 95 % by means of the statistical definition and with recording these two limits from the spectrum for the radionuclides of interest, the MDA can be determined by

$$MDA(Bq) = \frac{L_D}{tB\varepsilon} \tag{5.3}$$

where L_D is the detection limit, t is the counting time for the collected spectrum, B is gamma-ray branching ratio and ϵ is the gamma-ray detector efficiency. The minimum detectable activity is units of Becquerels (Bq) [81].

The detection limit of the gamma-ray spectrometry system was determined from the background measurement by counting some of the measured samples with a counting time of one week (604800 s). Table 5.1 represents the Minimum Detectable Activities calculated (in Bq) for the radionuclides of importance from ^{238}U and ^{232}Th decay chains that were identified in the sample of LV389.

Table 5.1: MDA (Bq) of radionuclides in based on one of the analysed samples (LV389) for a counting time of one week (604800 s).

Radionuclide	Energy (keV)	Critical level (Lc) (counts)	Detection limit (Ld) (counts)	Minimum detectable activity (MDA) (Bq)
^{234}Th	63.3	30.6 ± 1.2	63.7 ± 7.9	0.03
^{226}Ra	186.2	17.5 ± 0.6	37.5 ± 7.6	0.02
^{214}Pb	351.9	50.2 ± 0.3	102.9 ± 7.5	0.01
^{212}Pb	238.6	36.8 ± 0.2	76.1 ± 7.4	0.01
^{208}Tl	583.2	59.5 ± 0.5	121.4 ± 7.6	0.03

It should be noted that all the parts of the system are standard components bought for use in a general laboratory. From these MDA values it can be concluded that the system is capable of detecting low activity values.

5.3 Background subtraction and nuclides identification

Gamma-ray backgrounds in spectra originate from many components. For instance, radionuclides in the detector materials, radionuclides in the environment and radionuclides in the atmosphere can be significant sources of background [59]. Although lead shielding can isolate some of the level of background, the interaction of radiation within the lead shielding itself can give rise to the background due to radioactive contaminants in lead [12]. Once the system has been calibrated, it should be counted without any source in the detector and the recorded spectrum should be analysed in order to subtract the background counts from the actual samples to obtain the net counts for the radionuclides of interest. An example of a background spectrum from the BEGe detector and radionuclides identified is shown in Fig. 5.5. The environmental samples were placed directly on the endcap of the detector and counted. The duration of measurements of different samples varied according to the strength of the sources; in each case a background spectrum was collected for the same duration. The spectra observed from background and sample measurement were acquired via the prospect software associated with the system. The spectra analysed in order to identify the radionuclides for each gamma-ray energy and their intensities to be used in further calculations.

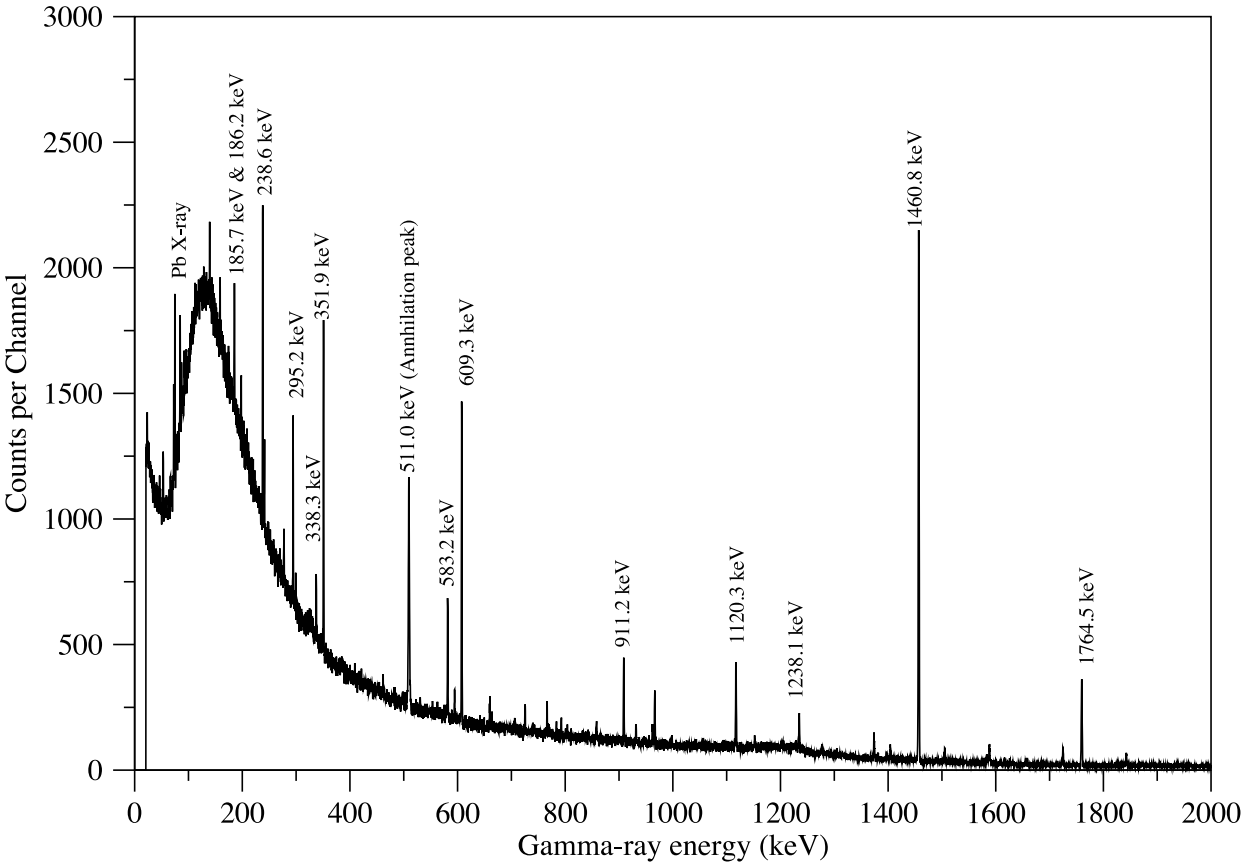

Figure 5.5: A background spectrum from BEGe detector for a time of 257697.6 s. The gamma-ray energies from uranium and thorium identified are labeled.

5.4 Photopeak determination

Radionuclides were identified by visual inspection of the photopeaks in a calibrated spectrum and comparisons of gamma-ray energies with the *Table of Isotopes*. The software provided with this detector can give the area for the peak and its associated uncertainty by selecting the region of interest. However, analysing environmental samples using gamma-ray spectrometry there are often situations where two adjacent peaks overlap to some extent even with high resolution detectors. In such situations, the lines are so close together that cannot be resolved and so the analyst cannot be sure how many peaks are present under this region. However, overlapping peaks may be identified by measuring the FWHM values and comparing with measurements of well resolved peaks. The software associated with the present detector, Prospect, does not identify multiple peaks at a single region of interest for some of gamma-ray lines. For example the peak of 92.6

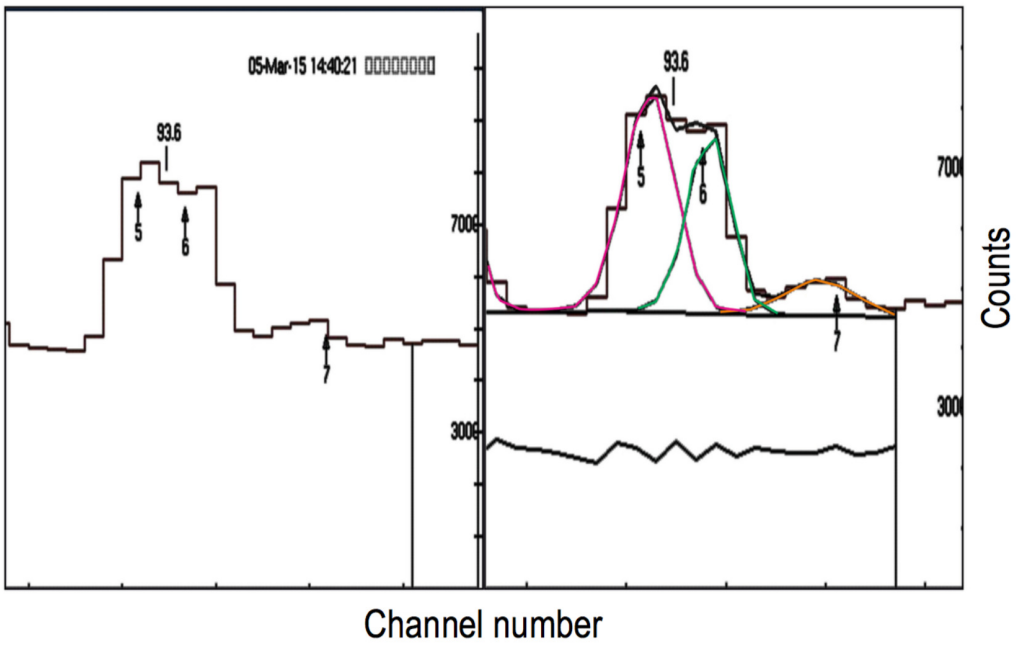

Figure 5.6: Example of fitting the 92-93 keV energy region using Gf3 software. Left panel: typical spectrum before fitting. Right panel: the same spectrum showing fitted peak shapes. Numbers are labels of fits.

keV from ^{234}Th overlaps with other photopeaks from members of the three natural decay series including X-rays (^{214}Bi, Kβ_1 at 89.8 keV (0.21%) and Kβ_1 at 92.3 keV (0.08%), ^{219}Rn, Kβ_1 at 89.8 keV (0.21%) and Kβ_2 at 92.3 keV (0.08%) and ^{228}Ac Kα_1 at 93.3 keV (3.1%)) [7, 38, 96, 108, 109]. This interference makes the peak of 92.6 keV less reliable than 63.3 keV peak for decay series measurements. For this reason another fitting program, GF3, was used to resolve this problem and identify the peak areas for convoluted peaks. This is a least-squares peak-fitting program, which is designed mainly to be used in analyzing gamma-ray spectra from Germanium detectors [110]

As can be seen from Fig. 5.6, this software can fit complex peak shapes and attribute energies and intensities to the components that contribute to the overall lineshape. Using this program has enabled us to resolve the 92.6 keV gamma-ray peak for ^{234}Th from the overlapping X-rays and has improved the agreement between the results for the two peaks of 63.3 keV and 92.6 keV from ^{234}Th.

5.5 Activity calculations

Once the radionuclides have been identified and the efficiency of the detector has been accurately established, calculations of the specific activity is the final step in nuclide analysis. The net area of the peak, the efficiency of the detector, the sample mass and the branching ratio of the source are directly related to the specific activity (in Bq·kg^1) as shown in the following

$$A = \frac{N}{t\varepsilon Bm} \tag{5.4}$$

where N is net area of the photopeak, t is the counting time of measurements (s), m is the mass of the sample (kg), ε is the counting efficiency at a specific energy and B is the gamma-ray transition probability [81]. If there is more than one peak for the same radioisotope, then the peak activities are averaged and weighted according to their relative uncertainties. Let us consider a radionuclide with two peaks that have activities A_1 and A_2, and the uncertainties associated with them are u_1 and u_2. The weighted activities thus can be calculated as

$$\text{Weighted activity} = \frac{(A_1 \text{wi}_1 + A_2 \text{wi}_2)}{(\text{wi}_1 + \text{wi}_2)}, \tag{5.5}$$

where wi_1 and wi_2 are the weights on A_1 and A_2, respectively, which can be calculated by

$$\text{wi} = \frac{1}{(u)^2} \tag{5.6}$$

The total weighted uncertainty then was calculated as

$$\text{Weighted error} = \frac{1}{\sqrt{(\text{wi}_1 + \text{wi}_2)}} \tag{5.7}$$

5.6 Uncertainty calculation

In any quantitative radioisotope analysis, the overall uncertainty of an analytical result depends on the combination of errors [59] introduced mainly by the measurement of peak

and background intensities, the efficiency calibration and the corrections for matrix effects. For example, the uncertainty expressed on a quantity of X, which is a function of other independent quantities Y_1, Y_2,.....Y_n can be calculated with the rules of error propagation as expressed in the equation below

$$\left(\frac{\sigma(X)}{X}\right)^2 = \left(\frac{\sigma(Y_1)}{Y_1}\right)^2 + \left(\frac{\sigma(Y_2)}{Y_2}\right)^2 + ... + \left(\frac{\sigma(Y_n)}{Y_n}\right)^2 \tag{5.8}$$

The combined uncertainty in these measurements can be grouped in two main categories. First, errors are generated by small changes in the initial conditions and affect the precision. For example, the repeated measurements of the peak area for a gamma-ray transition will produce a spread of results about the mean value. Second, errors affect the accuracy of a measurement and could arise from different sources including, uncertainty of efficiency, uncertainty of nuclide decay parameters. The uncertainty of nuclide decay emissions were not negligible especially for low-energy gamma rays from ^{234}Th nuclide as can be seen from Table 5.2.

The total uncertainty, (σ_{tot}), of the calculated activity values (A) is estimated by the following formula

$$\sigma_{tot} = A\sqrt{({\sigma_1}^2 + {\sigma_2}^2 + {\sigma_3}^2)}, \tag{5.9}$$

where σ_1 is the uncertainty on the net counts estimated from the errors on the peak intensity from the sample and subtracted background, σ_2 is the uncertainty on the efficiency including the physical parameters of the investigated sample, for example the density, thickness and chemical compositions and σ_3 is the uncertainty on gamma-ray emissions.

5.7 Determination of ^{238}U and ^{232}Th

Evaluation of radionuclides arising from natural sources can provide detailed information for understanding different issues in environmental sciences. Many radionuclides were present in the observed spectra from the measured samples. The significant radionuclides identified in the spectra were used for identifying disequilibrium in the ^{238}U and ^{232}Th

Table 5.2: Gamma-ray energy from uranium and thourium decay series and associated uncertainty on their gamma-ray emissions [7].

Radionuclide	E_γ (keV)	Error on branches (%)
Radionuclides from ^{238}U		
^{234}Th	63.3	10.8
	92.6	7.1
^{226}Ra	186.2	1.1
^{214}Pb	295.2	0.2
	351.9	0.2
^{214}Bi	609.3	0.3
	1120.2	0.2
	1764.4	0.2
^{210}Pb	46.5	0.9
Radionuclides from ^{232}Th		
^{228}Ac	338.3	0.02
	911.2	0.01
^{212}Pb	238.6	0.01
^{208}Tl	583.2	0.003

decay series. The gamma-ray energies and decay branching to check the identification were obtained from The National Nuclear Data Centre evaluation [7] and other nuclear data [41, 111]. Table 5.3 indicates gamma-ray energies and intensities for the most significant radionuclides from ^{238}U and ^{232}Th decay chains, which were used to obtain the activity concentrations of these nuclei and their daughters.

Since the ^{238}U nuclide emits a weak gamma-ray line (0.064 %) at 49.55 keV [7], which cannot be detected using gamma-spectrometry techniques [112], the activity of ^{238}U was estimated from gamma-ray emissions of its immediate daughter ^{234}Th at (63.3 and 92.6 keV). This is possible since a secular equilibrium is established between them in a short time because the half-life of the ^{234}Th daughter is 24.1 days [14, 59]. There are other contributions to the gamma-ray line of 63.3 keV from ^{234}Th, 63.9 keV (0.023%) from ^{231}Th and 63.8 keV (0.263%) from ^{232}Th but they were ignored due to the weak probabilities of the corresponding energy [95, 96, 113]

The granddaughter of ^{226}Ra was identified by its 186.2 keV gamma-ray emission after taking into account the interference with 185 keV gamma ray originating from ^{235}U.The

Table 5.3: Gamma-ray energies and associated emission probability per decay used for activity concentration determination; [1] The emission probability is the sum of the double gamma-ray at 62.9 keV and 63.3 keV (0.016, 3.7), [2] the emission probability is the sum of the double gamma-ray at 92.4 keV and 92.8 keV (2.13, 2.10), [3] the gamma-ray emissions corrected for the fraction of beta emission to ^{212}Po nuclide (64.1%).

Radionuclide	E_γ (keV)	Emission probability (%)
Radionuclides from ^{238}U		
^{234}Th	63.3	3.72[1]
	92.6	4.23[2]
^{226}Ra	186.2	3.64
^{214}Pb	295.2	18.42
	351.9	35.60
^{214}Bi	609.3	45.49
	1120.2	14.92
	1764.4	15.30
^{210}Pb	46.5	4.25
Radionuclides from ^{232}Th		
^{228}Ac	338.3	11.27
	911.2	25.80
^{212}Pb	238.6	43.60
^{208}Tl	583.2	30.6[3]

correction procedure is discussed later in Section 5.8.

The nuclides ^{214}Pb and ^{214}Bi are recommended for quantifying ^{226}Ra by many authors [10, 114, 115] and therefore they were estimated via their gamma-ray emissions indicated previously, and to quantify the state of disequilibrium in this chain. These two radionuclides are the most intense emissions in the spectra and because of their short half-lives, equilibrium is soon established. These radionuclides reach secular equilibrium with their parent ^{226}Ra within one month in a closed system. The most intensive lines for ^{214}Pb are 351.9 keV, 295.2 keV and 242 keV, however, the 242 keV gamma ray will not be considered here because it contaminated by the gamma-ray emission of other nuclides [116]. There is another gamma-ray emission at 351.1 keV from ^{211}Bi, from ^{235}U. However, this overlaps negligibly since the activity of ^{235}U is low in the measured samples. Gamma-ray lines of 609 keV, 1120 keV and 1764 keV were used to determine the activity ^{214}Bi. The lines of 609 keV and 1120 keV have been found to suffer from coincidence summing in other studies as indicated in ref [116]. However, in this work the effect of

coincidence summing was found to be less than 2% (see Section. 5.9).

Gamma-ray energy peaks arising from ^{235}U at 143.8 keV (11%), 163.4 keV (5%) and 205.3 keV (5%) were not detected in the spectra, however, there is a peak at 185.7 keV from this isotope, which is very close in energy to the 186.2 keV transition of ^{226}Ra from ^{238}U. Therefore, corrections must be applied in order to resolve these two gamma-ray lines from different sources [113]. The natural abundance of ^{238}U and ^{235}U are 99.27 % and 0.725 % and the half-lives are 4.47 $\times$ 10^9 years and 7.04 $\times$ 10^8 years, respectively.

The situation is similar for ^{232}Th since there is a weak gamma ray of 63.8 keV (0.26%) arising from this nucleus [7] and it cannot to be detected using gamma-ray spectroscopy. In this case, the activity of ^{232}Th is determined from its grandaughter ^{228}Ac, which has a half-life of 6 h. The activities from ^{212}Pb and ^{208}Tl from this decay-series were also measured in order to check the state of secular equilibrium and the reliability of the results obtained [68].

5.8 Correction for ^{226}Ra from ^{235}U

The only gamma-ray line for ^{226}Ra that has a sufficient intensity is the 186.2 keV (3.6%) transition. However, this line is significantly disturbed by the ^{235}U emission at 185.7 keV with an intensity 57%. These gamma rays cannot be resolved using a fitting procedure due to the small energy difference between the two components. In the present study no a special attention has been paid to the ^{235}U due to the low activities for this nuclide in the investigated samples. However, a correction for ^{226}Ra from ^{235}U at gamma emission of 186.2 keV was performed based on the assumption of the natural abundance as indicated in the calculations below.

5.8.1 Calculation of ^{238}U decay rate

The natural abundance and the half-life of ^{238}U are 99.3 % and 4.47 x 10^9 years, respectively. This half-life corresponds to 1.411 x 10^{17} seconds. The mean lifetime of a radioactive isotope, τ, can be obtained by [57]

$$\tau = t_{1/2}/ln(2), \tag{5.10}$$

which results in a mean lifetime of 2.035×10^{17} seconds. The decay constant, λ, is equal to the inverse of the mean lifetime

$$\lambda = \frac{1}{\tau}, \tag{5.11}$$

which corresponds to $\lambda = 4.914 \times 10^{-18}$ per second. This is the fraction of the ^{238}U that decays in one second. Therefore a mass of 0.993 gram of uranium decays at a rate of $0.993 \times 4.914 \times 10^{-18} = 4.88 \times 10^{-18}$ gram per second. The atomic mass of ^{238}U (238 gram/mole) and Avogadro constant (6.022×10^{23} atoms/mole) are used to convert this decay rate from grams per second to atoms per second as
$(4.88 \times 10^{-18}$ g/s) $\times$ (1.0 mole / 238 g) (6.022×10^{23} atoms / mole) $= 1.23 \times 10^{4}$ atoms/s.

5.8.2 Calculation of ^{235}U decay rate

The same steps above are followed with taking into account that the abundance of ^{235}U in natural uranium is 0.72 % and the half-life of ^{235}U is 7.04×10^{8} years. This will give a value of 570 atoms/s for the decay rate for ^{235}U.

5.8.3 Calculation of gamma fraction

The gamma ratio is calculated by multiplying gamma-ray intensity by the decay rate, which is 3.64 % and 57 % for ^{226}Ra and ^{235}U, respectively. From the calculations of the ratio of ^{238}U to ^{235}U based on their natural abundances, it is deduced that ^{226}Ra counts for 58% of the 186.2 keV peak, whereas 42 % from ^{235}U. Thus the contribution from ^{226}Ra at 186.2 keV can be calculated by multiplying the total count at this line by 0.58 ± 0.01.

5.9 Correction for coincidence summing

In cases where multiple gamma-ray cascades are emitted in a nuclide's decay, additional peaks can appear in the spectrum due to the coincidence summing of two or more gamma-ray photons [59]. This effect can decrease the number of counts in the full-energy peak.

Therefore, the correction for this effect should be taken into account especially in low-level measurements due to the close source-detector geometry [117, 118].

The correction for coincidence summing depends upon the total detection efficiency ε_t(E) at gamma-ray energy E and the gamma-ray transition probability. The total efficiency was calculated from the equation [118, 119]

$$\varepsilon_t(E) = \frac{\varepsilon_p(E)}{PT(E)}, \tag{5.12}$$

where ε_p(E) is the full-peak efficiency and PT(E) is the peak-to-total ratio, which is defined as the the number of counts in the full-energy peak and the total number of events in the spectrum [59]. The full-peak efficiency value was taken from the efficiency curve, but the peak-to-total efficiency was computed using the source of ^{137}Cs for the intermediate gamma-ray energy and ^{60}Co for the high gamma-ray energy, treating the volume source as a point source.

To demonstrate the correction method, the 609 keV gamma ray from ^{214}Bi is considered as an example for the photopeaks that are under the influence of coincidence summing. Let us consider the probabilities for the emission of two gamma rays are I_1 and I_2, the coincidence summing correction factor (C) was then calculated as the following formula

$$C = I_1 I_2 \varepsilon_t(E). \tag{5.13}$$

If we take two cases from the decay scheme of ^{214}Bi and substitute in the previous equation, we will get the following results

- C = 0.076 × 0.55 × 0.07 = 0.003
- C = 0.18 × 0.82 × 0.05 = 0.0074

where 0.076 and 0.18 are the probability of beta decay of ^{214}Bi resulting in a 609 keV gamma-ray and 0.55 and 0.82 are the probability of transitions of gamma-ray emissions for 768 keV and 1120 keV gamma-ray energies, respectively and 0.07 and 0.05 are the total efficiencies. Figure. 5.7 shows the diagram for the two decay schemes and the full

decay scheme for ^{214}Bi can be found in [120]. The values for the full-energy efficiency used above are based on the model efficiency for one of the measured samples (LV519). As can be seen from the deduced values, the effect of coincidence summing is negligible and when all of the possible branches are taken into account it is approximately 2%.

Figure 5.7: Selected paths in the decay scheme of ^{214}Bi to 0.768 MeV and 1.120 MeV gamma-ray emissions [120].

Chapter 6

Results and discussion

In this study a total of 14 samples were investigated in order to quantify possible disequilibrium in the uranium series decay. They were collected from different locations across the globe. The samples of LV393, LV395, LV396, LV398, LV523 and LV524 were from Etosha Pan in Namibia, the samples of LV519, LV520, LV521 and LV522 were from the Cambridge Gulf in Western Australia, the samples of LV389, LV390 and LV391were from Czech Republic and finally Nussi sample was from Germany. The specifications of these samples can be found in in Appendix A (Table. A.1). The following sections will present and discuss the results obtained for the relevant radioactive nuclides identified in the acquired spectrum for each measured sample.

6.1 Specific activities of the radionuclides from the ^{238}U and ^{232}Th decay chains

The experimental results for the specific activities for the radionuclides from ^{238}U decay series and from ^{232}Th are collected in Table 6.1 and Table 6.2, respectively (more details about the results for all the measured samples and their spectra can be found in Appendix A (A.3) and Appendix A (A.4), respectively). All the radionuclides have been measured by gamma-ray spectrometry using a Broad Energy Germanium Detector (BEGe-2825). As shown in Table 6.1, the specific activities of ^{234}Th ranged from 16.8 $\pm$ 2.3 to 80.2

± 4.8 Bq/kg, of ^{226}Ra from 13.9 ± 3.1 to 97.9 ± 6.0 Bq/kg , of ^{214}Pb from 16.8 ± 0.6 to 116.2 ± 3.4 Bq/kg, of ^{214}Bi from 16.6 ± 0.7 to 112.2 ± 2.6 and of ^{210}Pb from 15.9 ± 2.6 to 114.2 ± 8.2 Bq/kg. Of all the fourteen samples measured in this study, the sample of LV523 has the highest activities of ^{234}Th and ^{226}Ra. Equilibrium is established between ^{234}Th and its parent ^{238}U very quickly (168 days) due to the short half-life for ^{234}Th (24.1 days) compared to ^{238}U (4.47×10^9 years) [37]. Therefore, ^{234}Th is the only nuclide that contributed to the quantification of ^{238}U. The two peaks of 63.3 keV and 92.6 keV contributed to the determination of ^{234}Th. Fig. 6.1 shows the specific activities (Bq/kg) obtained for ^{234}Th using its 63.3 keV peak versus the 92.6 keV peak. The values of the 63.3 keV peak correspond to the analysis of gamma-ray spectra using the software associated with the detector (Prospect). However the values of the 92.6 keV peak was obtained from fitting gamma-ray spectra using Gf3 software. As can be observed, the values obtained from the two peaks of 63.3 keV and 92.6 keV are in a good agreement in all the measured samples suggesting the reliability of the peak correction of 92.6 keV from other contributions.

Table 6.1: Specific activities of the relevant radionuclides from ^{238}U decay series.

Sample region	Sample ID	Specific activity (Bq/kg)				
		^{234}Th	^{226}Ra	^{214}Pb	^{214}Bi	^{210}Pb
Namibia	LV393	44.1 ± 1.5	65.5 ±4.0	75.3 ± 2.2	70.6 ±1.9	68.5 ± 5.0
Namibia	LV395	52.5 ± 3.1	92.9 ± 5.3	116.2 ± 3.4	108.6 ± 2.5	114.2 ± 8.2
Namibia	LV396	45.4 ± 2.7	70.2 ± 4.2	79.7 ±2.4	75.1 ± 1.9	76.4 ± 5.6
Namibia	LV398	62.1 ± 4.4	83.3 ± 4.8	88.8 ± 2.6	81.7 ± 2.1	80.4 ± 5.6
Australia	LV519	34.3 ± 3.0	37.3 ± 3.5	28.7 ± 1.1	25.9 ± 1.1	28.3 ± 3.5
Australia	LV520	36.1 ± 2.9	38.0 ± 3.5	29.60± 1.1	27.5 ± 1.2	26.3 ± 3.4
Australia	LV521	32.7 ± 2.9	33.6 ± 3.5	32.2 ± 1.2	31.4 ± 1.2	32.2 ± 3.7
Australia	LV522	33.1 ± 2.1	36.4 ± 3.5	28.1 ± 1.1	26.6 ± 1.2	25.6 ± 3.1
Namibia	LV523	80.2 ± 4.8	97.9 ± 6.0	113.2 ± 3.3	112.2 ± 2.6	96.7 ± 7.5
Namibia	LV524	62.3 ± 4.8	82.4 ± 5.3	97.4 ± 2.9	87.1 ± 2.2	80.5 ± 6.4
Czech Republic	LV389	18.4 ± 2.4	13.9 ± 3.1	16.8 ± 0.6	16.6 ± 0.7	15.9 ± 2.6
Czech Republic	LV390	16.8 ± 2.3	17.9 ± 3.1	19.5 ± 0.8	17.6 ± 0.8	16.6 ± 2.4
Czech Republic	LV391	23.5 ± 2.4	20.2 ± 3.2	20.3 ± 0.7	18.3 ± 0.7	18.0±2.5
Germany	Nussi	30.6 ± 2.8	28.7± 3.1	34.5± 1.1	32.4 ± 1.0	30.9 ±3.5

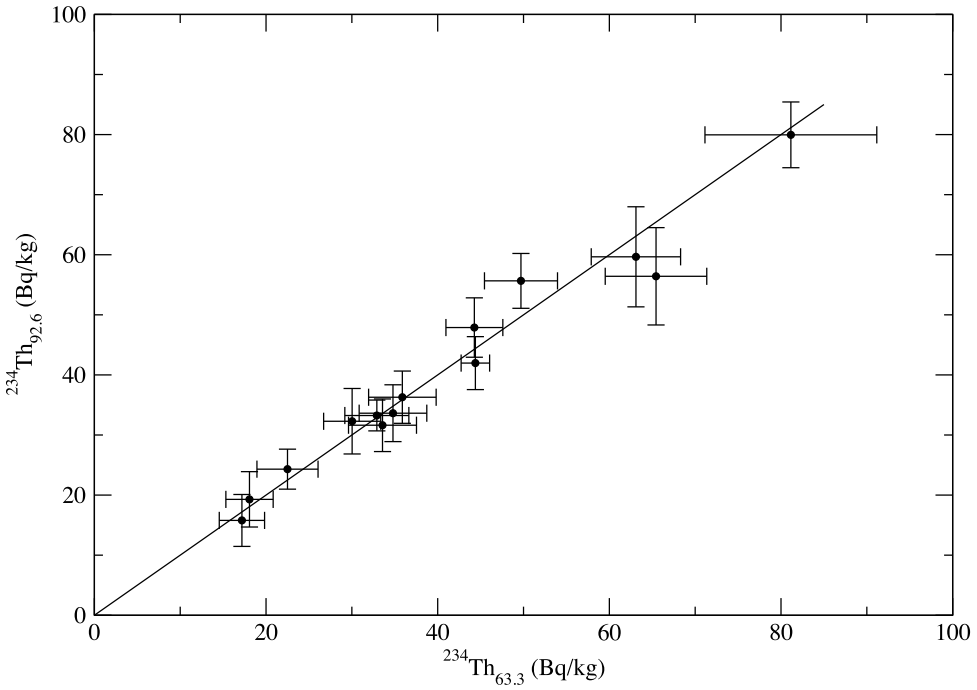

Figure 6.1: Comparison of the results of the ^{234}Th specific activities using its peaks at 63.3 keV and 92.6 keV in the all measured samples. The line represents the 1 : 1 agreement.

The experimental findings show that the ^{238}U activities (^{234}Th) compared to those of ^{226}Ra are small, this shows the state of disequilibrium. The determination of ^{226}Ra activities were obtained by measuring the intensity of the 186.2 keV energy line and using its daughters ^{214}Pb and ^{214}Bi. The direct determination for ^{226}Ra has the disadvantage that its most intensive line (186.2 keV, 3.6%) overlaps with ^{235}U (185.7 keV, 57%). Therefore, the ^{226}Ra results were corrected to account for the contribution from ^{235}U. The correction factor of 0.58 was obtained from calculations discussed previously within this thesis assuming that the natural abundance for ^{235}U is 0.7%. Thus the ^{226}Ra activity obtained from measurement of the gamma-ray signal at 186.2 keV was corrected by multiplying by 0.58.

The activity of the ^{226}Ra nuclide obtained from the 186.2 keV peak is consistent with the respective daughter nuclei of ^{214}Pb, ^{214}Bi and ^{210}Pb in all the measured samples.

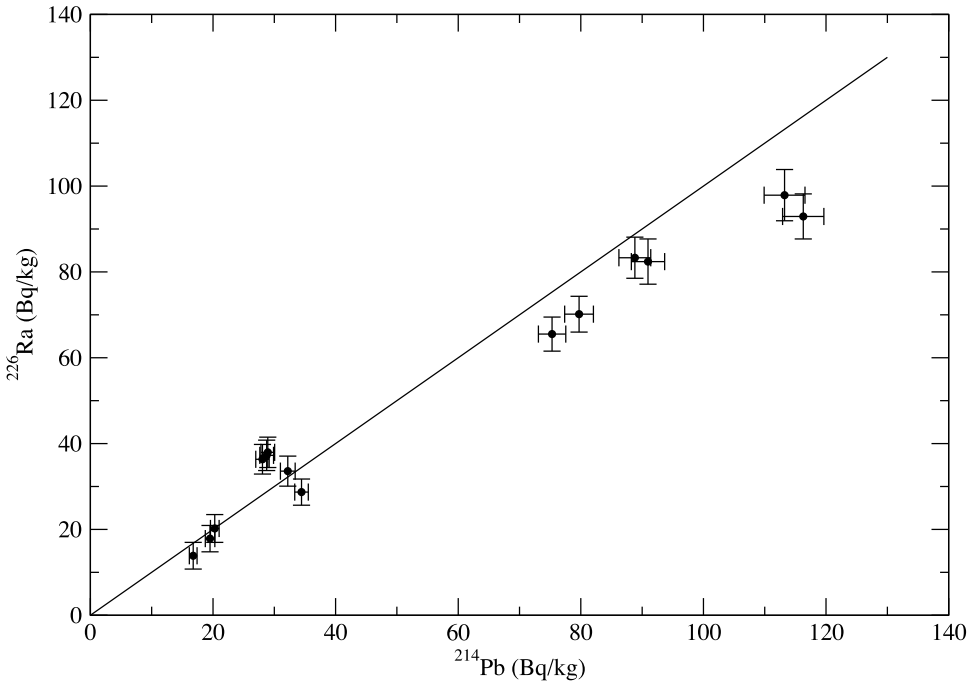

Figure 6.2: ^{214}Pb and ^{226}Ra diagram of samples. The equilibrium line is displayed.

The ^{214}Pb activity concentrations follow very closely those of ^{214}Bi as illustrated by the results in Fig. 6.2 and Fig. 6.3. This shows that the ^{214}Pb and ^{214}Bi activities agree with each other and are in equilibrium with their parent ^{226}Ra and the situation is the same for ^{210}Pb daughter as indicated in Fig. 6.4. In some cases, the deviations from the correlation line are covered by the uncertainty of the measurement, especially if one considers 2σ uncertainties.

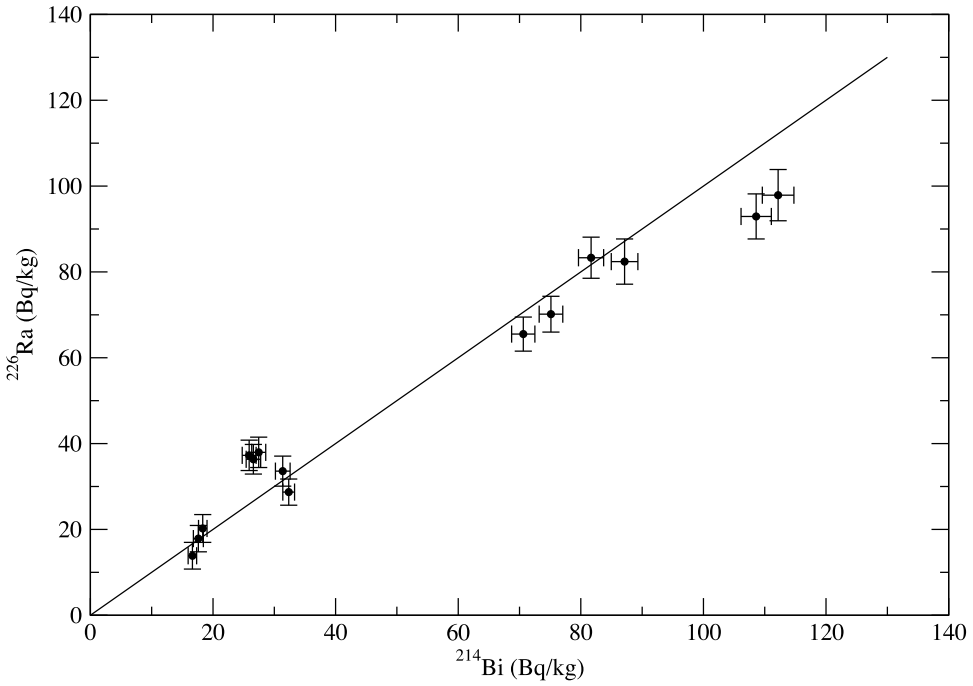

Figure 6.3: ^{214}Bi and ^{226}Ra diagram of samples. The equilibrium line is displayed.

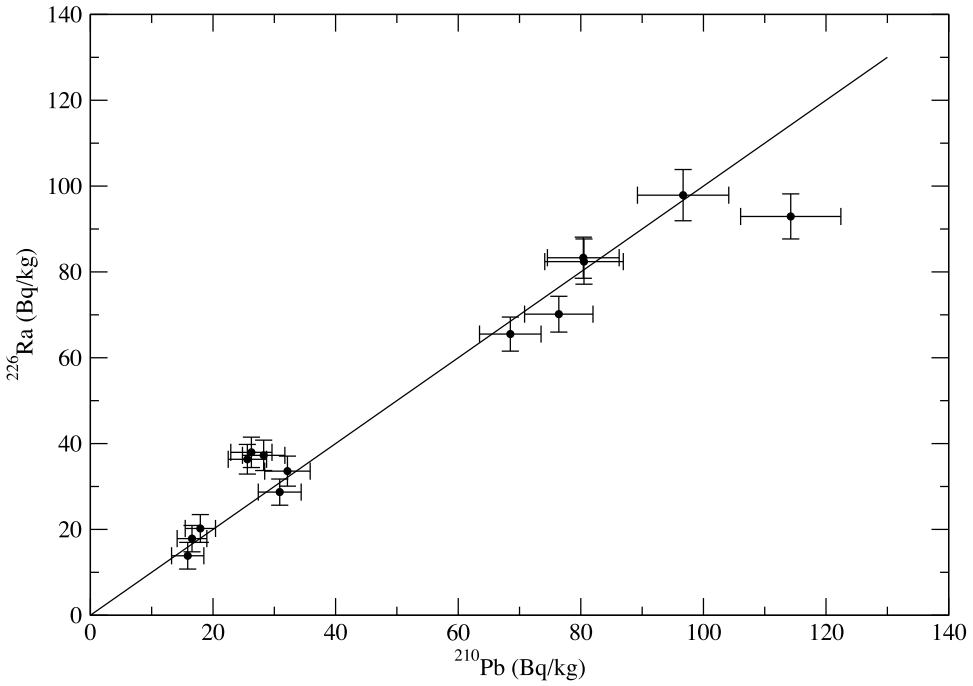

Figure 6.4: ^{214}Bi and ^{226}Ra diagram of samples. The equilibrium line is displayed.

The quantification of ^{232}Th activity by gamma-ray spectrometry was by its significant progenies of ^{228}Ac, ^{212}Pb and ^{208}Tl. The obtained results of the activity concentrations of radionuclides from ^{232}Th ranged from 20.6 ±1.0 to 60.6 ± 2.0 Bq/kg of ^{228}Ac, from 20.0 ± 0.9 to 59.7 ± 2.5 Bq/kg of ^{212}Pb and from 21.1 ± 1.0 to 58.6 ± 2.4 Bq/kg of ^{208}Tl. As can be observed from Table 6.2, the LV521 sample presented the highest activities for all the radionuclides from ^{232}Th decay series. It is also shown from Fig. 6.5 and Fig. 6.6 and Table 6.2 that radionuclides from the decay series of ^{232}Th are always found to be in equilibrium in all the samples investigated. This implies that the decay series of ^{232}Th is found in equilibrium because thorium is an immobile element and less fractionated compared to uranium and radium.

The activity concentrations of ^{238}U presented in Table 6.1 revealed that in three samples (LV398, LV523 and LV524) there is an elevated level of ^{238}U (^{234}Th) activity. Suggested reference activity concentration of uranium and its progeny vary from 11.3 Bq/kg

Table 6.2: Specific activities of the relevant radionuclides from ^{232}Th decay series.

Sample region	Sample ID	Specific activity (Bq/kg)		
		^{228}Ac	^{212}Pb	^{208}Tl
Namibia	LV393	28.5±1.3	24.0±1.3	27.7±1.5
Namibia	LV395	37.4±1.4	37.0±1.8	37.1±1.8
Namibia	LV396	33.0±1.4	32.9±1.6	32.3±2.0
Namibia	LV398	28.3±1.2	25.8±1.4	28.7±1.6
Australia	LV519	54.3±1.9	52.8±2.2	49.7±2.1
Australia	LV520	59.2±2.0	56.8±2.3	54.8±2.3
Australia	LV521	60.6±2.0	59.7±2.5	58.6±2.4
Australia	LV522	53.0±1.9	51.5±2.1	52.5±1.9
Namibia	LV523	35.4±1.5	35.3±1.5	34.3±1.5
Namibia	LV524	34.3±1.5	32.0±1.4	34.4±1.6
Czech Republic	LV389	20.6±1.0	20.0±0.9	22.0±1.0
Czech Republic	LV390	21.9±1.2	22.4±1.0	21.1±1.0
Czech Republic	LV391	24.7±1.1	23.5±1.0	22.4±1.1
Germany	Nussi	32.7±1.2	32.1±1.3	33.4±1.5

to 56.6 Bq/kg for ^{234}Th and 14.0 Bq/kg to 63.7 for ^{226}Ra and 27.2 Bq/kg to 93.0 Bq/kg for ^{214}Pb and ^{214}Bi [50]. The same reference suggest that ^{232}Th varies 1.49 Bq/kg to 44.7 Bq/kg in some locations that are situated in Namibia. This indicates that the activity concentration of thorium (^{232}Th) presented in Table 6.2 is normal for the measured samples from Namibia.

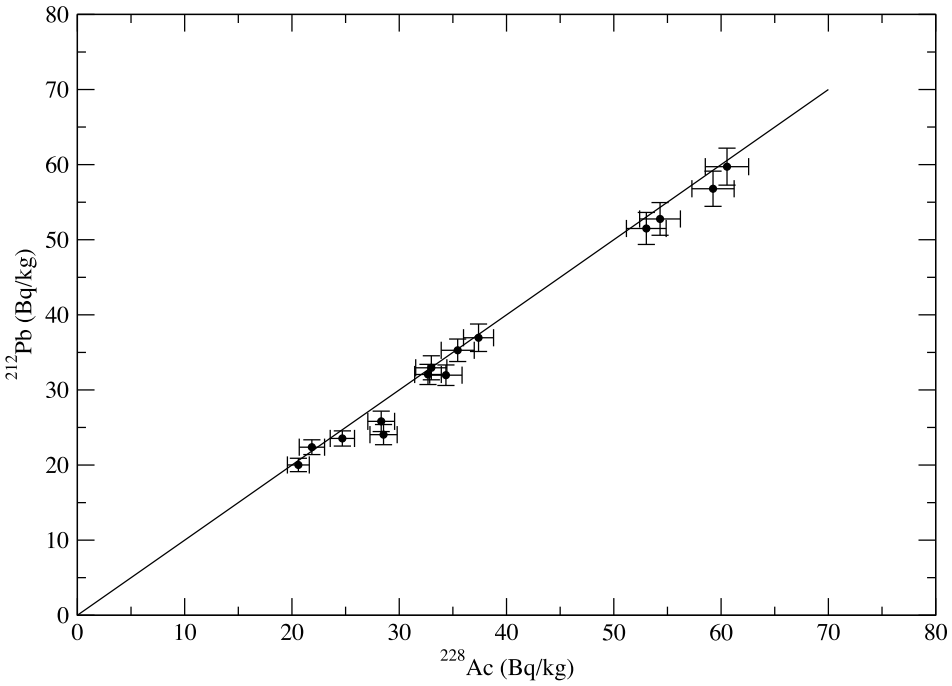

Figure 6.5: ^{228}Ac and ^{212}Pb diagram of samples. The equilibrium line is displayed.

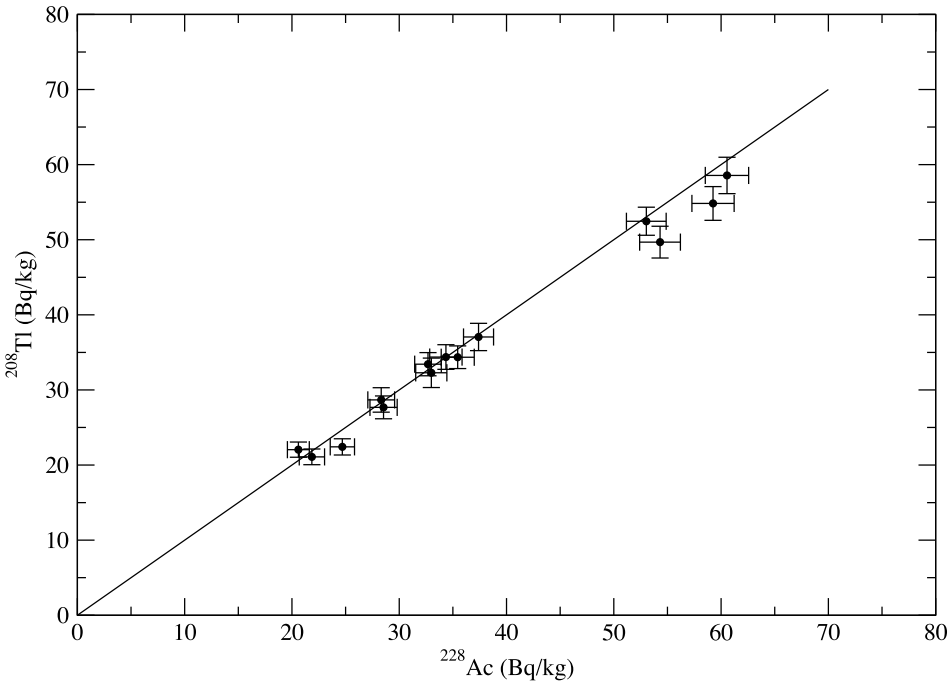

Figure 6.6: ^{228}Ac and ^{208}Tl diagram of samples. The equilibrium line is displayed.

6.2 Concentration of ^{238}U and ^{232}Th

The elemental concentration of ^{238}U and ^{232}Th in part per millions (ppm) can be obtained by converting the specific activities in Bq.kg^{-1} using the conversion factors of 12.4 and 4.06 for ^{238}U and ^{232}Th, respectively [121, 122]. Since the ^{234}Th radionuclide was used to determine ^{238}U, the activity concentrations of this radionuclide were used to calculate the concentration of ^{238}U. For ^{232}Th, the activity of the radionuclides of ^{228}Ac, ^{212}Pb and ^{208}Tl were used. In the current study, the ranges of the calculated elemental concentrations in all sediment samples are found to be 1.4 ± 0.2 to 6.5 ± 0.4 ppm for uranium, and 5.1± 0.1 to 14.7 ± 0.3 ppm for thorium. Sediments from Australia presented the highest concentration from ^{232}Th (12.9±0.3 to 14.7±0.3 ppm). This is may be indicative of enrichment of thorium due to natural processes in this region. The relationship between uranium and thorium can be considered in terms of the Th/U ratio. According to [14], the theoretical

values of the elemental ratios of Th/U are expected to range from 3.5 to 6.3 in igneous rocks, 2.0 to 4.3 in metamorphic rocks and 1.6 to 3.8 in sedimentary rocks [123]. In the current study, the obtained results of the elemental ratios for Th/U varies from 1.3 ± 0.1 to 5.6 ± 0.5, which are consistent with the theoretical values. Samples from Czech Republic presented elemental concentrations for uranium and thorium consistent with the Earth's crust average. Whereas sediments from Namibia presented an elevated level for uranium approaching the average value in granite rocks. The respective results for U and Th concentrations and their ratio in all the measured samples are shown in Table 6.3.

Table 6.3: The elemental concentrations of uranium and thorium in all the measured samples.

Sample region	Sample ID	^{238}U (ppm)	^{232}Th (ppm)	Th/U ratio
		(^{234}Th)	(^{228}Ac - ^{212}Pb - ^{208}Tl)	
Namibia	LV393	3.6±0.1	6.6±0.2	1.9± 0.1
Namibia	LV395	4.2±0.3	9.2±0.2	2.2 ± 0.1
Namibia	LV396	3.7±0.2	8.1±0.2	2.2 ± 0.1
Namibia	LV398	5.0±0.4	6.8±0.2	1.4 ± 0.1
Australia	LV519	2.8±0.2	12.9±0.3	4.7 ± 0.4
Australia	LV520	2.9±0.2	14.1±0.3	4.8 ± 0.4
Australia	LV521	2.6±0.2	14.7±0.3	5.6 ± 0.5
Australia	LV522	2.7±0.2	12.9±0.3	4.8 ± 0.3
Namibia	LV523	6.5±0.4	8.6±0.2	1.3 ± 0.1
Namibia	LV524	5.0±0.4	8.2±0.2	1.6 ± 0.1
Czech Republic	LV389	1.5±0.2	5.1±0.1	3.5 ± 0.5
Czech Republic	LV390	1.4±0.2	5.4±0.2	4.0 ± 0.5
Czech Republic	LV391	1.9±0.2	5.8±0.2	3.1 ± 0.3
Germany	Nussi	2.5±0.2	8.0±0.2	3.3 ± 0.3

The elemental concentrations of the ^{238}U and ^{232}Th presented above also showed that sediments from Australia contain a uniform level of the uranium and thorium. Suggested reference elemental concentration of uranium and thorium are 2.3 ppm and 13 ppm, respectively [124]. Using these suggested reference values, the concentration of uranium (^{238}U) and thorium (^{232}Th) is normal for all the measured samples from Australia.

6.3 Disequilibrium in the Uranium series

6.3.1 Possible origins of disequilibrium in sediment and soil samples

Long-lived radionuclides in the uranium series may be expected to fractionate and vary according to the environmental conditions. For example, the behaviour of different isotopes in the environment is controlled by their chemical properties, and by specific processes related to their radioactive decay, i.e., alpha recoil [125]. In natural water, the fractionation results from the interaction with mineral or organics due to the difference in the chemical properties [125]. In sediment and soil samples disequilibrium can originate from different possible influences. Processes such as transport and deposition of mobile elements in water can interrupt the primary state of the system and produce a state of disequilibrium [126]. The variation in the chemical properties of the elements in the uranium series can cause fractionations. For example, uranium and radium are chemically mobile and thorium is immobile, due to the respective solubility properties of their ions [16]. Uranium and thorium both occur in nature in the state of +4, however, uranium can also exist in the form of +6 as uranyl ion ($UO_2{}^{+2}$), which forms compounds that are soluble in water. For example, the oxidation state of uranium and thorium in primary igneous rocks and minerals is the 4+ state, but uranium can be also oxidized to 5+ and 6+ states in the near-surface environment. In the redox state of +6 (oxidizing conditions), uranium is soluble and mobile, however, it is much less soluble and mobile in the state +4 (reducing conditions) [14]. Thorium is mostly transported on the surface of clay minerals where it is adsorbed [14]. Radium is a member of the alkaline earth metals and has similar chemical characteristics similar to the elements in this group. Therefore, radium can can pose significant interferences with calcium and barium [127, 128]. In solution, there is only one oxidation state for radium (Ra^{+2}) [129, 128] . In some circumstances, radium can be leached from clay and adsorbed to heavy metals or metal oxides such as manganese (Mn) and iron (Fe) [26].

The thorium decay series consists of isotopes that cannot be fractionated significantly from the parent due to their relatively short half-lives [34]. This fact results in the rapid return to the secular equilibrium condition even if a preferential chemical separation of

the various elements in the decay series has occurred. Consequently, it is expected that concentrations of radionuclides in the thorium decay series would be found in secular equilibrium. This is shown clearly from the results, Table 6.2, for all the measured samples from different locations. The situation is similar for some of the uranium decay series daughters, where short-lived isotopes are found. However, uranium decay series has three relatively long-lived progeny isotopes (^{234}U, ^{230}Th, and ^{226}Ra). Thus it is reasonable to consider that these might not be in equilibrium with the parent ^{238}U nuclide. The first long-lived isotopes in the decay series, ^{234}U and ^{230}Th, are alpha emitters without a significant gamma-ray signature. Therefore, alpha spectroscopy is the only effective means of measurement of these radionuclides.

In this work, the use of a high-resolution gamma-ray spectroscopy system resolved and measured ^{226}Ra (and its significant gamma emitting progeny) directly. The progenies of ^{226}Ra are very short-lived (^{214}Pb and ^{214}Bi) and have significant gamma-ray signatures that can be used to indicate equilibrium within the chain and to quantify the concentration of the parent ^{226}Ra isotope. A possible problem occurs with equilibrium within ^{238}U decay chain because the first daughter of ^{226}Ra is an isotope of Radon (^{222}Rn), which is a noble gas. The ^{222}Rn nuclide is potentially more mobile as a gas than ^{226}Ra. Therefore; the emanation of radon from the system may lead to a disequilibrium condition between ^{226}Ra and the rest of the decay chain [14]. However, this is not typically significant in situ but can be exacerbated by the process of sampling and sample preparation. In the present work, sealing the samples in airtight containers for a sufficient period of time before analysis permitted radon daughters ingrowth and ensured equilibrium conditions with ^{226}Ra have been reached. The observation that ^{210}Pb, ^{214}Pb, ^{214}Bi and ^{226}Ra have consistent activities shows that there was not loss of radon and indicates that samples were appropriately sealed.

6.3.2 Interpreting of the state of disequilibrium

The data collected by gamma-ray spectroscopy can be used to solve at least part of the problem. Understanding the processes that led to the fractionation of U-series nuclides

and thus disequilibrium is the crucial part for interpreting the obtained results. Interpretation of disequilibrium origin in this work is based on the simple idea that the most mobile element produces the most variable activities. The obtained results (Table 6.1) demonstrate that out of fourteen samples, six samples, which are LV393, LV395, LV396, LV398, LV523 and LV524, are found to be in a state of disequilibrium. The collection of these samples was from the same region; the Etosha Pan in Namibia. This location is a dried lake bed, which is depressed in a flat environment, that is flooded occasionally by overflowing rivers [130]. The sources of these rivers are in the tropics where there is abundant rainfall and in between flood periods the pan falls dry [130]. For more details about the nature and the environment of this region, the reader is referred to [106]. Sediments collected from the shoreline of the former lake display pronounced uranium series disequilibrium with fractionation of ^{226}Ra relative to the parent ^{238}U.

According to [1, 14], disequilibrium between Ra and U isotopes may be occurred in the decay chains due to (i) precipitation/ dissolution reactions, (ii) alpha recoil, and (iii) diffusion. The results indicate that leaching and accumulation of ^{226}Ra from inflowing water has taken place. Figures. 6.7, 6.8 and Table 6.1 illustrate the disequilibrium state in the samples from Namibia, which occurred between the head of the series ^{238}U and the ^{226}Ra radionuclide. As previously stated, uranium and radium are the most mobile elements in the environmental conditions and the study of their activity is able to show which is the most variable, and therefore, the origin of disequilibrium. Figure. 6.7 shows that ^{226}Ra is the most variable element since its activities are greater than the ^{238}U parent. This can be interpreted that the disequilibrium condition may result from the leaching of radium from different materials into the system.

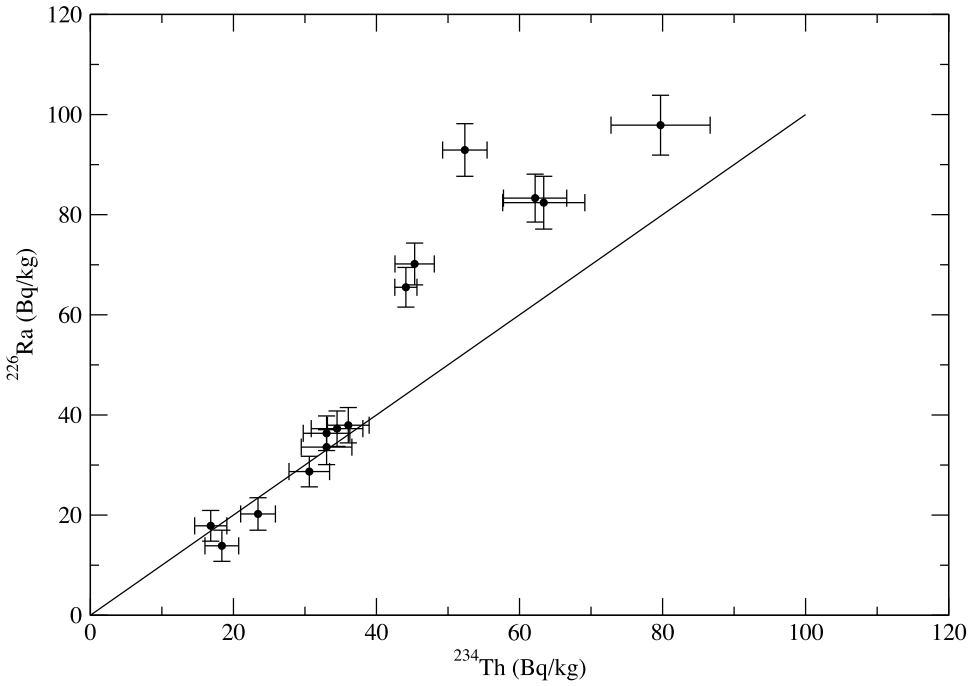

Figure 6.7: ^{226}Ra and ^{234}Th diagram for all the measured samples. The equilibrium line is displayed. ^{226}Ra varied in the six samples from Namibia (open circle pattern). These data are indicated in Table 6.1.

As shown in Table 6.4, in the samples from Namibia, the ^{226}Ra/^{238}U activity ratio ranges from 1.22 ± 0.13 to 1.77 ± 0.15. For LV523 and LV524 samples this ratio approaches the unity within the uncertainty value. These samples were collected from the same sand ridge indicating that the fractionation of radium at this part of the pan is lower compared to other sediments. This ratio gives a clear evidence that the main impact of the radium released to the system could arise from the direct deposition from sediments and/or the different incorporation and leaching properties of the radionuclide from the waters to the sedimentary environment. It is also observed that uranium and radium are in secular equilibrium for the remaining samples; LV389, LV390, LV391, LV519, LV520, LV521, LV522 and Nussi as shown in Table 6.4 and Fig. 6.9. The activities of ^{234}Th and ^{226}Ra in these samples are correlated and consistent with a line passing through the origin as shown

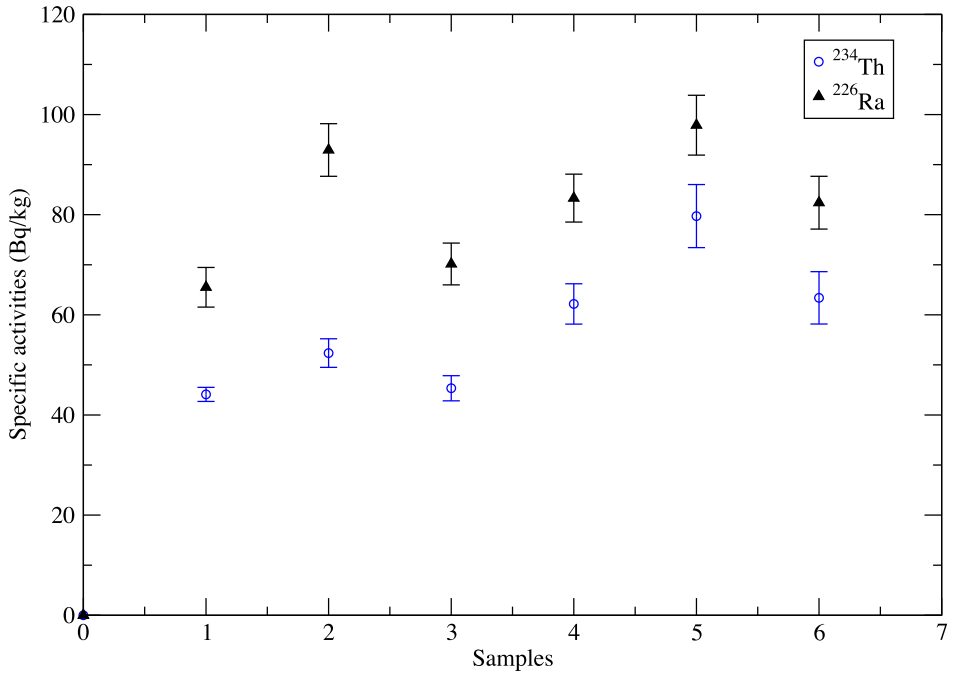

Figure 6.8: The variation of ^{234}Th and ^{226}Ra in samples that were found in equilibrium as indicated in Table 6.1. The numbers of 1, 2, 3, 4, 5 and 6 on X-axis refer to the samples ID of LV393, LV395, LV396, LV398, LV523 and LV524, respectively.

in Fig. 6.7. This indicates that these samples have a uniform ^{226}Ra : ^{238}U (^{234}Th) ratio and therefore the environments where they have been derived are close system. However, in the samples where the equilibrium was disturbed, the radium activity concentrations were high and the ratios are larger than unity, indicating that ^{226}Ra was brought to the system by the accummulation from the water column. The essential reason for this excess in radium is that radium an alkaline earth metal and occurs as Ra^{2+} when dissolved in water, which makes it mobile in most environments [76, 126].

Table 6.4: The activity ratio of ^{226}Ra to ^{238}U (^{234}Th) in all the measured samples.

Sample region	Sample ID	^{226}Ra/^{238}U
Namibia	LV393	1.49 ± 0.10
Namibia	LV395	1.77 ± 0.15
Namibia	LV396	1.55 ± 0.13
Namibia	LV398	1.34 ± 0.12
Australia	LV519	1.09 ± 0.14
Australia	LV520	1.05 ± 0.12
Australia	LV521	1.03 ± 0.12
Australia	LV522	1.10 ± 0.13
Namibia	LV523	1.22 ± 0.13
Namibia	LV524	1.32 ± 0.14
Czech Republic	LV389	0.75 ± 0.19
Czech Republic	LV390	1.06 ± 0.23
Czech Republic	LV391	0.86 ± 0.16
Germany	Nussi	0.94 ± 0.13

6.4 Reliability of the method

To ensure that the results from an analytical procedure are reliable, an experimental or theoretical verification process must be applied. Some of the results were validated using complementary independent techniques to confirm the ^{238}U and ^{232}Th concentrations. The measurements of the concentrations of ^{238}U and ^{232}Th (in ppm) in four of the analyzed samples have been determined independently with Inductively Coupled Plasma Mass Spectrometry (ICP-MS) at the University of Cambridge. Measurements were checked for accuracy against several standards from multiple sources (U.S. Geological Survey Geochemical Reference Materials and also synthetic matrix standards from European Suppliers). The ICP-MS measurements defined the elemental concentrations with uncertainties at the 3-5 % level based on repeated analysis. The respective results are listed in Table 6.5 for the two different techniques. It is shown that ICP-MS technique gave consistent uranium and thorium concentrations with those deduced from gamma-ray spectrometry. This indicates that the procedure followed using gamma-ray spectrometry in the present work is reliable. This is particularly of importance with respect to ^{238}U, which is quantified using the low-energy emitting radionuclide of ^{234}Th as discussed earlier. This also can be

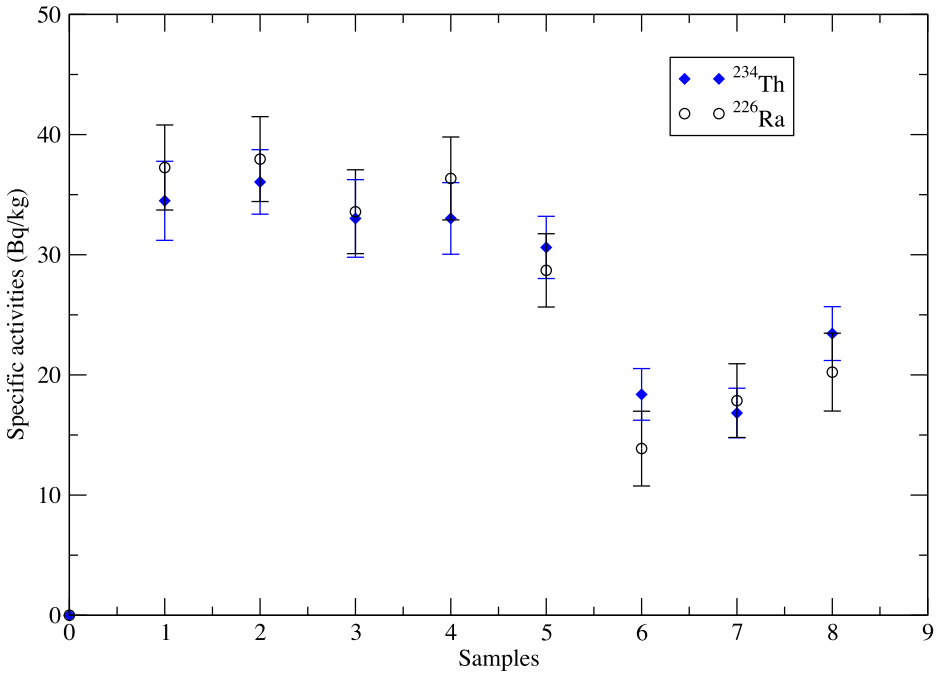

Figure 6.9: The variation of ^{234}Th and ^{226}Ra in non-equilibrium data as discussed above and shown in Table 6.1. The numbers of 1, 2, 3, 4, 5, 6, 7 and 8 on X-axis refer to the samples ID of LV519, LV520, LV521, LV522, LV389, LV390, LV391 and Nussi, respectively.

observed from the correlation diagram shown in Fig. 6.10. The good agreement obtained provides a confidence for the procedure followed to determine the ^{238}U concentrations. The situation is the same for ^{232}Th, where results denote the good agreement as indicated in Fig. 6.11.

Analysing reference materials is another procedure performed as a mean of validation. The results obtained for the standard material of IAEA-312 also indicate the good agreement between values obtained in the current study and the recommended values presented in the reference sheet for this material in Appendix A (A.1.3). Table 6.6 shows a comparison between these values.

Table 6.5: ^{238}U and ^{232}Th concentrations (ppm) from two independent techniques; [1]using BEGe detector, [2]using ICP-MS system.

Sample region	Sample ID	Gamma-ray Spectrometry[1] ppm		Mass Spectrometry[2] ppm	
		^{238}U	^{232}Th	^{238}U	^{232}Th
Czech Republic	LV389	1.5 ± 0.2	5.1 ± 0.1	1.6 ± 0.1	5.3 ± 0.3
Namibia	LV395	4.2 ± 0.3	9.2 ± 0.3	4.8 ± 0.2	10.1 ± 0.5
Namibia	LV396	3.7 ± 0.2	8.1 ± 0.3	3.8 ± 0.2	8.4 ± 0.4
Germany	Nussi	2.5 ± 0.2	8.0 ± 0.2	2.3 ± 0.1	8.7 ± 0.4

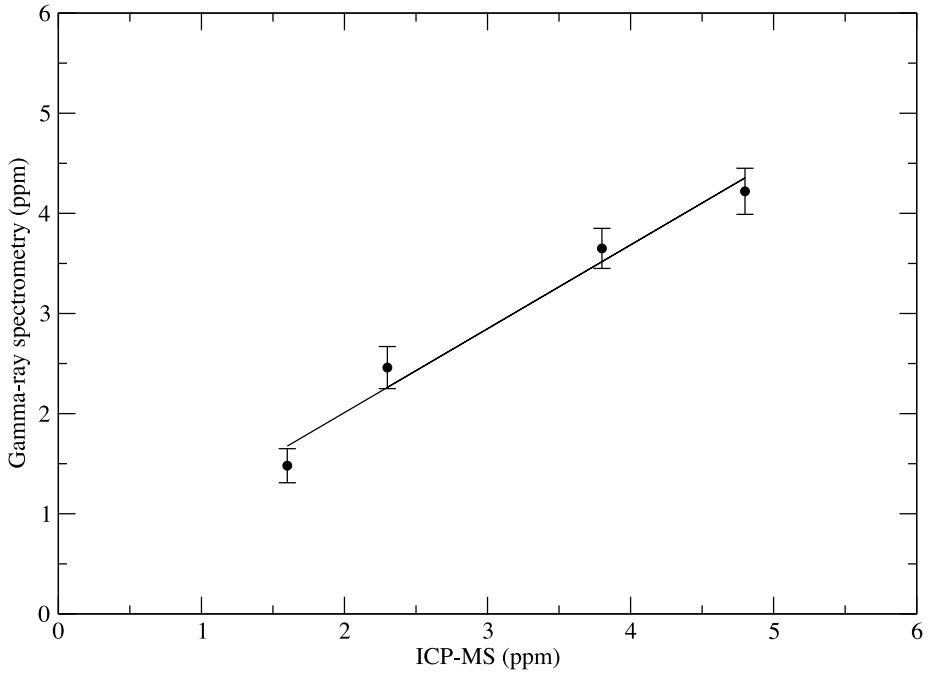

Figure 6.10: Comparison between the ^{238}U concentrations determined by gamma-ray spectrometry (BEGe detector) and ICP-MS system.

Eight of the measured samples show secular equilibrium between radionuclides from ^{238}U decay series, see Table 6.1 and Fig. 6.7. This also validates the method applied to determine ^{234}Th and thus ^{238}U. This is particularly significant for the low gamma-ray energies such as 46.5 keV from ^{210}Pb, 63.3 keV and 92.6 keV from ^{234}Th, which are influenced by several issues including sample self-attenuation and overlapping with other

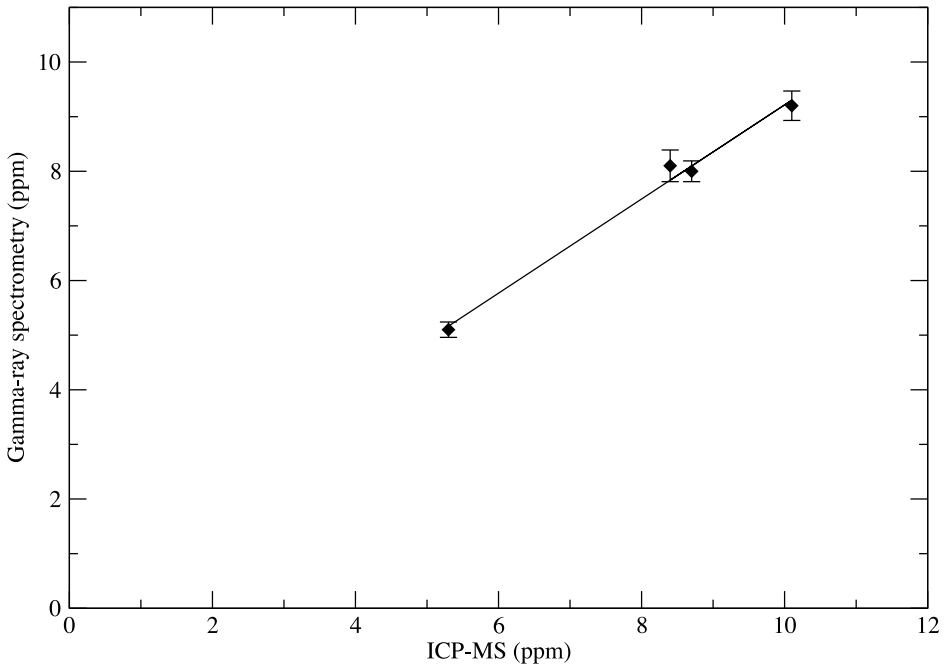

Figure 6.11: Comparison between the ^{232}Th concentrations determined by gamma-ray spectrometry (BEGe detector) and ICP-MS system.

Table 6.6: ^{238}U, ^{232}Th and ^{226}Ra concentrations (ppm) for IAEA-312 standard material from gamma spectrometry using BEGe detector and data presented in the reference sheet in Appendix A (A.1.3).

Element	Gamma Spectrometry results ppm	Recommended values	
		Mean value	95% Confidence interval
Uranium	17.1 ± 1.4	16.5	15.7-17.4
Thorium	84.7 ± 2.7	91.4	81.3-101.5
Radium	249.7 ± 15.4	269	255 -287

gamma or X-ray emissions.

The results in the present work also indicate that ^{226}Ra activity concentrations can be determined reliably using the peak of 186.2 keV in the sediment samples. This can be verified from the activity concentration of the ^{226}Ra calculated from the peaks of radon daughters (^{214}Pb and ^{214}Bi). In all the samples measured, ^{226}Ra was in a good agreement

with ^{210}Pb, which emits low-energy gamma-ray, suggesting that equilibrium existed and verifying the radioactive disequilibrium between ^{238}U and ^{226}Ra in some of the measured samples. Estimating the activity concentration of ^{226}Ra using its 186.2 keV gamma-ray emission is proved to be reliable even for different geological material such as coal slag samples as emphasized by [131].

The measurement of some of the samples investigated in this study using different method of gamma-ray spectrometry is another mean of validating to the procedure. The Nussi sample has been analysed using gamma-ray spectrometry in several laboratories allowing an opportunity to compare results obtained by different analytical approaches. These approaches were based on the conventional procedure, which includes calculating the activities with a comparison to certified material instead of an efficiency calibration for the system. The concentrations in ppm for ^{238}U and ^{232}Th in this sample from different systems and laboratories including the present results are indicated in Table 6.7.

Table 6.7: A comparison for concentrations of ^{238}U and ^{232}Th from Nussi sample obtained using different gamma-ray spectrometry systems; * Ge detector, • neutron activation analysis. Details about the results presented in this Table can be obtained by a personal communication with Babara Mauz.

Facility used	^{238}U (ppm)	^{232}Th (ppm)
*Liverpool-BEGe	2.5 ± 0.2	8.0 ± 0.2
*Liverpool-coaxial	3.1 ± 0.1	8.9 ± 0.2
*FS HD	3.3 ± 0.2	8.2 ± 0.9
*FS Canberra-spec	3.3 ± 0.1	7.6 ± 0.2
*FS old g-spec	3.1 ± 0.1	7.4 ± 0.2
*SAW Freiberg g-spec	3.0 ± 0.1	7.4 ± 0.3
*Dresden g-spec	2.4 ± 1.1	7.9 ± 0.4
•NAA, HD	2.8 ± 0.2	8.1 ± 0.2
*Fribourg g-spec	2.9 ± 0.2	7.2 ± 0.5
*TU Freiberg g-spec	3.0 ± 0.1	7.3 ± 0.2
•NAA MPI	3.0 ± 0.1	8.1 ± 0.1
•NAA MPI	2.8 ± 0.1	8.3 ± 0.9
*Freiberg	2.9 ± 0.4	7.5 ± 1.2

Table 6.7 shows that the results obtained in this work agree with the other results and for ^{232}Th the accuracy is comparable to the best of the other results.

Some of the measured samples (Namibia samples) were also analysed using another type of germanium detector (Coaxial geometry) and the results obtained are shown in Table 6.8. This was part of a different project [130]. The detector was in a 100 mm thick lead shield and had a size of 70.0 mm diameter and 32.4 mm length. For this work the low energy efficiency calibration was done with a single source of standard material (IAEA-375). The results in Table 6.8 show that the additional low energy efficiency calibration carried out in the present work result in different results.

Table 6.8: ^{234}Th and ^{210}Pb activities (Bq/kg) from two germanium detectors; * details about the results from this detector can be obtained by a personal communication with Babara Mauz.

Sample ID	BEGe detector Bq/kg		Coaxial detector* Bq/kg	
	^{234}Th	^{210}Pb	^{234}Th	^{210}Pb
LV393	44.1 ± 1.5	68.5 ± 5.0	51.0 ± 1.7	84.2 ± 13.1
LV395	52.5 ± 3.1	114.2 ± 8.2	70.4 ± 2.4	155.7 ± 24.1
LV396	45.4 ± 2.7	76.4 ± 5.6	56.2 ± 2.0	94.3 ± 14.7
LV398	62.1 ± 4.4	80.4 ± 5.6	79.6 ± 2.6	111.5 ± 17.3

Chapter 7

Conclusions and Future Work

7.1 Summary

The disequilibrium in U-series decay in sediments collected from four different regions has been quantified using high-resolution gamma-ray spectrometry. In this study, the measurements showed that radionuclides of ^{234}Th, ^{226}Ra, ^{214}Pb, ^{214}Bi and ^{210}Pb from ^{238}U and ^{228}Ac, ^{212}Pb and ^{208}Tl from ^{232}Th are detected and quantified in all the sediment samples. The radionuclide of ^{234}Th was used to determine the quantity of the parent nuclide of ^{238}U. The weighted average for the activities of ^{234}Th was calculated using the 63 keV peak and the 92 keV peak. The peak fitting software GF3 was used for the 92 keV peak as this lies in a complex region of the spectrum. The correction for self-absorption for both gamma-ray energies was studied in detail using a combination of calibrated samples for experimental measurements and the LabSOCS software which allow the correction to be adjusted for each sample. Consistent results were obtained for both gamma ray peaks. The calculation of ^{226}Ra activities was determined from its gamma-ray peak of 186 keV with a correction applied for the peak of similar energy from the decay of ^{235}U. For all samples the ^{226}Ra activity is consistent with results from its daughters of ^{214}Pb and ^{214}Bi. The activity of ^{210}Pb was determined using its peak of 46.5 keV. The same process, described above was used for self-absorption correction. A range of activities was found across the samples. In the results ^{232}Th was high in Australia compared to other

regions. The results also show that ^{238}U is high in some of the samples from Namibia, which are LV398, LV523 and LV524, compared to other samples from the same location. This is indicative that the results are influenced by geological structure variations in some of the regions studied. . Based on the Author' s knowledge the level of naturally occurring radioactive material are not assessed for the regions of the Czech Republic and the north coast of Western Australia in the literature. Therefore the results in this current study can be used as a baseline for the level of radionuclides from ^{238}U and ^{232}Th in the studied regions and the observation of any possible changes in the future.

The activity ratios between ^{226}Ra and ^{238}U, and between other granddaughters (^{214}Pb, ^{214}Bi and ^{210}Pb) and ^{226}Ra in ^{238}U decay series and between ^{228}Ac and its daughters in ^{232}Th decay series were used to validate the existence of radioactive equilibrium through the decay chains. The isotopic activity ratios of ^{226}Ra/^{214}Pb, and ^{214}Pb/^{214}Bi and ^{214}Bi/^{210}Pb in the ^{238}U decay series and those of ^{228}Ac/^{212}Pb and ^{212}Pb/^{208}Tl from the ^{232}Th decay chain were found to be close to unity. The results demonstrate that the state of secular equilibrium has been achieved in all samples between these radionuclides. However, the isotopic activity ratios of ^{226}Ra/^{238}U (^{234}Th) were larger than the unity in six of the measured samples. The origin of these samples was from the same location, which is Etosha Pan in Namibia. These results are indicative that a state of disequilibrium was produced in ^{238}U decay chain in this region. This may be as a result of the variation in the chemical properties of ^{226}Ra.

The activity concentrations of ^{238}U, ^{232}Th were converted into the elemental concentrations in terms of ppm (parts per million) in this current study. The ranges of the calculated elemental concentrations in all sediment samples in the current study are found to be 1.4 $\pm$ 0.2 to 6.5 $\pm$ 1.4 ppm for ^{238}U and 5.1 $\pm$ 0.1 to 14.9 ppm for ^{232}Th. The obtained results of the elemental ratios of Th/U varies from 1.3 $\pm$ 0.1 to 5.6 $\pm$ 0.5. A high value of the Th/U ratio as measured in some studied locations may be indicative of a depletion of uranium or an enrichment of thorium due to alteration or natural processes in those areas. These results obtained for ^{238}U and ^{232}Th are consistent with mass spectrometry (ICP-MS) measurement for LV389, LV395, LV396 and Nussi samples.

7.2 Conclusion

This work has shown that a standard BEGe detector in a 50 mm thick graded lead shield can be used for environmental measurements with activities as low as 10 Bq/kg. The excellent energy resolution of the BEGe detector, especially at low gamma-ray energy, results in spectra with an improved peak height to background ratio giving reliable and accurate results in a complex region of the spectrum. This is particularly important for the low energy gamma rays (46 keV, 63 keV and 92 keV) used in this work for investigating the ^{238}U decay chain.

The method of using a validated model calculation (LabSOCS) to determine the detection efficiency as a function of gamma-ray energy for each individual sample has been shown to be successful. The determination of the ^{238}U content relied on the use of 63 and 92 keV gamma rays. It has been shown that the efficiency for these low energies is dependent on the detailed geometry and composition of the samples and it is difficult to reproduce this variation across a range of samples with standard reference material. This work has demonstrated the need to know the geometry (size, shape and density) and composition of each sample in detail often requiring further measurements such as x-ray fluorescence in order to determine whether there are any higher Z (greater than about 20) present. All this information is needed for input to a model calculation which in turn needs to be validated using standard material or by gamma-ray transmission measurements using the actual samples to be measured. A model calculation needs to be carried out for each sample in order to get the correct low energy efficiency for that sample..

The method developed has shown that the ^{232}Th decay chain is in secular equilibrium in all the samples measured. The measurements further show that ^{238}U decay chain is in secular equilibrium in all samples measured except those from Namibia. In the latter samples there is an enhanced amount of ^{226}Ra and its daughters meaning the decay chain in disequilibrium.

The absolute values of U and Th in the samples are in agreement with results from mass spectrometry measurements (ICP-MS) further validating the methods used in the present work where low energy gamma rays were used to determine the Uranium content.

7.3 Future Work

The use of validated modelling of the efficiency at low gamma-ray energy could be investigated for a wider range of sample geometries and detector types. The problem arising from self-absorption will get bigger for larger and denser samples.

The state of disequilibrium found in this study was established as a results of the radium excess. The source of water in the regions from where the samples were collected was freshwater. Future work should include more freshwater and marine water source sediments. The variation in the sediments might give different results to what have been found here. For example in the marine environment disequilibrium can result from the variation in uranium not only radium [14, 16, 26]. Studying a variety of samples may give different type of disequilibrium based on the variation of the radionuclides properties.

Gamma-ray spectrometry does not detect radionuclides with no or very weak gamma-ray emissions such as ^{234}U and ^{230}Th from ^{238}U decay series. Therefore using a combination of different techniques [34, 132] will help to investigate further information for other nuclei in U-series decay.

Appendices

Appendix A

A.1 Standard sources certificates

A.1.1 NPRL604 Marinelli Beaker

Calibration certificate N° CT/120476/12/1542 **Page 3 / 3**

3 Results NPRL 604

REF DATE 03/12/2012 12:00

Activity by radionuclide :

Reference	Multigamma : **9ML01EGRM[15]** - No : **78251B / 1**	
Radionuclide	Activity concentration Bq (a)	Extented relative uncertainty in % (k=2) (8)
Americium 241	**1,637E+3**	**± 6**
Cadmium 109	**7,93E+3**	**± 6**
Cobalt 57	**394E+0**	**± 6**
Cerium 139	**397E+0**	**± 5**
Chromium 51	**16,22E+3**	**± 5**
Tin 113	**2,35E+3**	**± 5**
Strontium 85	**1,584E+3**	**± 5**
Cesium 137	**2,39E+3**	**± 5**
Cobalt 60	**2,37E+3**	**± 5**
Yttrium 88	**2,32E+3**	**± 5**

() See note enclosed.
For complementary informations consult LNHB web site : htpp://www,nucleide,org,
(a) Activity given equivalent water for an identical geometry and quantity flask,

The extented uncertainties mentioned are those corresponding to two incertitude composed type,
The uncertainties types have been calculated taking into account the different uncertainties components : reference standards, means if calibration, environmental conditions, the data of the calibrated instrument, repeatibility,,,

The delivery of a certificate calibration with logotype COFRAC guarantees the traceability of the calibration results according to the international unity system,

Only the original copy is valid.

A.1.2 IAEA-375 Standard Material

International Atomic Energy Agency
Analytical Quality Control Services
Wagramer Strasse 5, P.O.Box 100, A-1400 Vienna, Austria

REFERENCE SHEET

REFERENCE MATERIAL

IAEA-375

RADIONUCLIDES AND TRACE ELEMENTS IN SOIL

Date of issue: January 2000⊕

Recommended Values
(Based on dry weight)

Reference Date for decay correction: 31st December 1991

Radionuclide	Recommended Value Bq/kg	95% Confidence Interval Bq/kg	N*
^{40}K	424	417 – 432	84
^{90}Sr	108	101 – 114	43
^{106}Ru	56	53 – 58	26
^{125}Sb	77	74 – 79	38
^{129}I	0.0017	0.0013 – 0.0021	10
^{134}Cs	463	454 – 472	87
^{137}Cs	5280	5200 – 5360	91
^{226}Ra	20	18 – 22	37
^{232}Th	20.5	19.2 – 21.9	11

Recommended Values
(Based on dry weight)

Element	Recommended Value mg/kg	95% Confidence Interval mg/kg	N*
Th	5.2	5.0 – 5.4	26
U	1.86	1.66 – 2.05	30

* *Number of accepted laboratory means which were used to calculate the recommended values and confidence intervals.*

⊕ *Revision of the reference sheet dated December 1997; original report date: August 1994.*

Note: Some evidence has been presented to suggest that this material may be contaminated with "hot particles" resulting from the Chernobyl accident. The frequency of the occurrence of these "hot particles" is unknown and consequently, it is possible that significantly elevated activities may be observed for anthropogenic radionuclides in some sub-samples.

Information Values
(Based on dry weight)

Reference Date for decay correction: 31st December 1991

Radionuclide	Information Value Bq/kg	95% Confidence Interval Bq/kg	N*
^{228}Th	21	17 – 25	6
^{234}U	25	17 – 32	5
^{238}U	24.4	19.0 – 29.8	7
^{238}Pu	0.071	0.056 – 0.085	10
$^{239+240}$Pu	0.30	0.26 – 0.34	20
^{241}Am	0.13	0.11 – 0.15	6

Information Values
(Based on dry weight)

Element	Information Value mg/kg	95% Confidence Interval mg/kg	N*
As	2.56	2.24 – 2.88	6
Ba	335	316 – 354	6
La	17.6	15.3 – 19.9	5
Ni	9.7	7.9 – 11.6	5
Rb	48	44 – 52	8
Yb	1.73	1.24 – 2.22	5

* *Number of accepted laboratory means which were used to calculate the information values and confidence intervals.*

The values listed above were established on the basis of statistically valid results submitted by laboratories which had participated in an international intercomparison exercise organized in 1992. The details concerning the criteria for qualification as a recommended value can be found in the report (IAEA/AL/075) "Report on the Intercomparison Run IAEA-375: Radionuclides in Soil" [1]. This report is available free of charge upon request.

Intended Use

This sample is intended to be used as a reference material for the measurement of radionuclides in soil samples. It can also be used as a quality control material for the assessment of a laboratory's analytical work, for the validation of analytical methods and for quality assurance within a laboratory.

Dry weight determination

All recommended values are expressed on a dry weight basis. Therefore the dry weight must be determined at the time of analysis, using separate sub-samples of at least 500 mg dried to constant weight in a drying oven set to 105 °C. Subsequent weighings should differ by less than 5 mg.

Instructions for use

The recommended minimum intake masses for analysis of trace elements and radionuclides are 0.2 g and 6g respectively.

Analysts are reminded to take appropriate precautions in order to avoid contamination of the material during handling. No special precautions are required for the storage of this material.

References

[1] Strachnov V., LaRosa J., Dekner R., Zeisler R. and Fajgelj A., Report on the Intercomparison run IAEA-375: Radionuclides in Soil.
IAEA/AL/075, IAEA, Vienna, Austria 1996.

A.1.3 IAEA-312 Standard Material

International Atomic Energy Agency
Analytical Quality Control Services
Wagramer Strasse 5, P.O.Box 100, A-1400 Vienna, Austria

REFERENCE SHEET

REFERENCE MATERIAL

IAEA-312

^{226}Ra, Th and U
IN SOIL

Date of issue: January 2000⊕

Recommended Values
(Based on dry weight)

Reference Date: 30th January 1988

Element	Recommended Value Bq/kg	95% Confidence Interval Bq/kg	N*
^{226}Ra	269	250 – 287	25

Element	Recommended Value mg/kg	95% Confidence Interval mg/kg	N*
Th	91.4	81.3 – 101.5	32
U	16.5	15.7 – 17.4	29

* *Number of accepted laboratory means which were used to calculate the recommended values and confidence intervals.*

⊕ *Revision of the original reference sheet dated January 1991*

The values listed above were established on the basis of statistically valid results submitted by laboratories which had participated in an international intercomparison exercise organized during 1990. The details concerning the criteria for qualification as a recommended value can be found in the report (IAEA/AL/036) "Report on the Intercomparison Run IAEA-312: ^{226}Ra, Th and U in Soil" [1]. This report is available free of charge upon request.

Intended Use

This sample is intended to be used as a reference material for the measurement of ^{226}Ra, Th and U in soil samples. It can also be used as a quality control material for the assessment of a laboratory's analytical work, for the validation of analytical methods and for quality assurance within a laboratory.

Origin and preparation of the material

The soil sample collected from the Sibolga area of northern Sumatra was donated by the Indonesian Atomic Energy Commission (IAEC).

The material was air dried and then ground to pass through a 0.18 mm sieve before being homogenized. The material was dispensed into plastic bottles in 50 g units without any further processing. Subsequently, the samples were irradiated to a dose of 2.5×10^4 Gy using a ^{60}Co source to ensure long-term stability of the material by inhibiting microbial action.

Homogeneity

The homogeneity of the bottled material was assessed by the determination of uranium using laser fluorimetry in two 500 mg sub-samples taken from a number of bottles chosen at random from the whole production run. The between and within bottle variability was assessed (on the basis of the F test, at the 95% confidence level) and indicated that the contribution due the heterogeneity of the material was small and therefore the material could be considered to be homogeneous for a sample size at or above 500 mg.

Dry weight determination

All recommended values are expressed on a dry weight basis. Therefore the dry weight must be determined at the time of analysis, using separate sub-samples of at least 500 mg dried to constant weight in a drying oven set to 105 °C. Subsequent weighings should differ by less than 5 mg.

Instructions for use

The recommended sample size for analysis is 500 mg. Analysts are reminded to take appropriate precautions in order to avoid contamination of the material during handling. No special precautions are required for the storage of this material.

Legal disclaimer

The IAEA makes no warranties, expressed or implied, with respect to the data contained in this reference sheet and shall not be liable for any damage that may result from the use of such data.

References

[1] Strachnov V., Valkovic V., Zeisler R. and Dekner R., Report on the Intercomparison Run IAEA-312: ^{226}Ra, Th and U in Soil.
IAEA/AL/036, IAEA, Vienna, Austria 1991.

A.2 Samples specifications

Table A.1: Samples description; ; [1] poorly means different range of grain sizes, [2] well means that the grain sizes are all consistent.

Sample ID	Coordinates	Depositional Environment	Sediment Texture	Dominant grain size (μm)
LV393	18.41S, 16.15E	Lake shoreline	Poorly[1] sorted silty sand	100-200
LV395	18.41S, 16.15E	Lake shoreline	Poorly sorted silty sand	100-200
LV396	18.41S, 16.15E	Lake shoreline	Poorly sorted silty sand	100-200
LV398	18.41S, 16.15E	Lake shoreline	Poorly sorted silty sand	100-200
LV519	15.33S, 128.40E	Fluvial (slackwater) deposit	Poorly sorted silt	10-80
LV520	15.33S, 128.40E	Fluvial (slackwater) deposit	Poorly sorted silt	10-80
LV521	15.33S, 128.40E	Fluvial (slackwater) deposit	Poorly sorted silt	10-80
LV522	15.33S, 128.40E	Fluvial (slackwater) deposit	Poorly sorted silt	10-80
LV523	18.41S, 16.15E	Lake shoreline	Poorly sorted silty sand	100-200
LV524	18.41S, 16.15E	Lake shoreline	Poorly sorted silty sand	100-200
LV389	49.58N, 15.20E	Hill foot colluvium	Poorly sorted silt	40-80
LV390	49.58N, 15.20E	Hill foot colluvium	Poorly sorted silt	40-80
LV391	49.58N, 15.20E	Hill foot colluvium	Poorly sorted silt	40-80
Nussi	49.10N, 8.40E	Aeolian silt on hill surface	Well[2] sorted silt	20-40

A.3 Tables of Results for the activity calculations

Table A.2: Namibia samples.

Radionuclide	E_γ (keV)	LV393	LV395	LV396	LV398	LV523	LV524
Radionuclides from ^{238}U (Bq/kg)							
^{234}Th	63	44.39 ±1.66	49.70 ±4.25	44.27± 3.31	63.10± 5.21	81.15± 10.01	65.44± 5.92
	92	41.97 ±4.41	55.66 ±4.56	47.89± 4.95	59.66± 8.33	79.95± 5.47	56.41± 8.10
^{214}Pb	295	74.44 ±3.17	115.58 ±4.77	79.44± 3.36	87.56± 3.67	112.47± 4.72	96.37± 4.10
	351	76.17 ±3.14	116.98 ±4.75	79.96± 3.30	90.07± 3.69	113.98± 4.69	98.48± 4.08
^{214}Bi	609	70.25 ±2.27	106.11 ±3.28	73.18± 2.35	81.87± 2.59	99.64± 3.14	83.82± 2.70
	1120	66.04 ±4.75	109.93 ±5.04	76.18± 4.40	82.30± 4.45	94.76± 4.94	84.48± 4.70
	1764	77.57 ±5.07	114.39 ±5.69	83.07± 5.15	80.08± 5.11	99.93± 5.51	93.40± 5.37
Radionuclides from ^{232}Th (Bq/kg)							
^{228}Ac	338	28.26 ±1.88	36.09 ±2.07	33.00± 2.48	28.80± 1.85	35.52± 2.42	35.30± 2.39
	911	28.78 ±1.72	38.48 ±1.89	32.98± 1.79	27.92± 1.69	35.39± 2.00	33.72± 1.95

Table A.3: Australia samples.

Radionuclide	E_γ (keV)	LV519	LV520	LV521	LV522
Radionuclides from ^{238}U (Bq/kg)					
^{234}Th	63	34.79 ±3.94	35.88 ±3.94	33.57± 3.96	32.91± 3.73
	92	33.62 ±4.73	36.29 ±4.35	31.62± 4.38	33.25± 2.57
^{214}Pb	295	28.47 ±1.70	29.34 ±1.71	31.10± 1.78	27.80± 1.66
	351	28.97 ±1.49	29.81 ±1.51	33.13± 1.63	28.29± 1.45
^{214}Bi	609	25.75 ±1.28	28.03 ±1.25	31.89± 1.33	26.65± 1.32
	1120	26.30 ±3.20	27.48 ±3.75	33.01± 3.59	25.87± 3.82
	1764	26.79 ±4.03	28.42 ±4.28	32.06± 4.36	27.36± 4.71
Radionuclides from ^{232}Th (Bq/kg)					
^{228}Ac	338	53.08 ±3.03	55.22 ±3.07	53.08± 3.03	55.22± 3.07
	911	55.11 ±2.44	62.07 ±2.57	55.11± 2.44	62.07± 2.57

Table A.4: Nussi and samples from Czech Republic.

Radionuclide	E_γ (keV)	LV389	LV390	LV391	Nussi
Radionuclides from ^{238}U (Bq/kg)					
^{234}Th	63	18.07 ±2.75	17.19 ±2.64	22.50± 3.56	30.03± 3.32
	92	19.29 ±4.61	15.78 ±4.33	24.32± 3.33	32.29± 5.45
^{214}Pb	295	15.39 ±0.92	18.48 ±1.21	19.40± 1.04	33.88± 1.68
	351	18.00 ±0.87	20.25 ±1.02	21.06± 0.98	34.89± 1.49
^{214}Bi	609	16.50 ±0.77	17.35 ±0.89	17.91± 0.77	31.68± 1.14
	1120	15.00 ±2.33	17.39 ±2.53	19.79± 2.24	31.42± 2.49
	1764	19.44 ±2.29	20.39 ±2.76	20.52± 2.27	36.96± 2.63
Radionuclides from ^{232}Th (Bq/kg)					
^{228}Ac	338	20.77 ±1.68	20.31 ±2.09	25.76± 1.91	32.26± 2.11
	911	20.50 ±1.29	22.59 ±1.43	24.14± 1.40	32.89± 1.53

A.4 The spectra of the measured samples

A.4.1 Standard materials

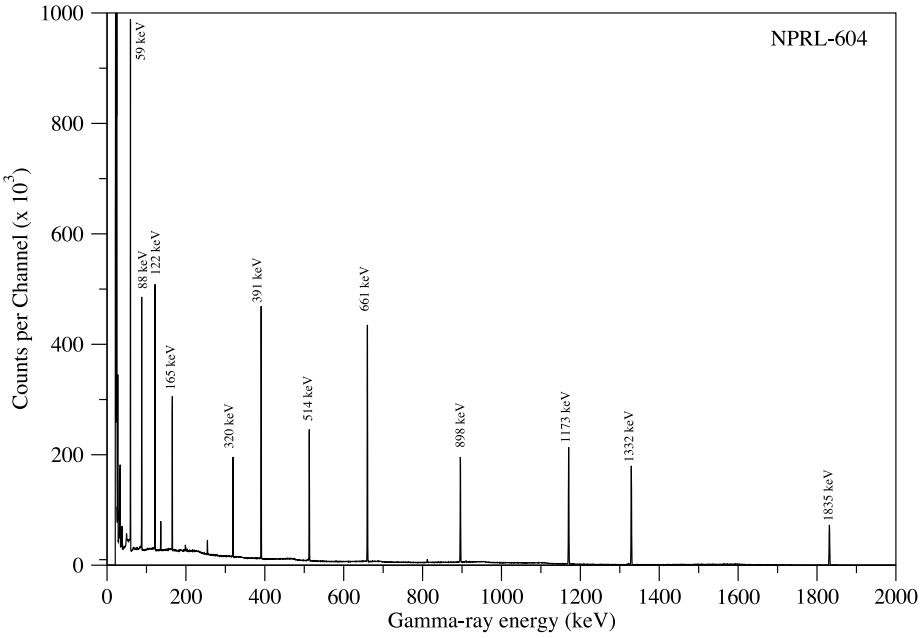

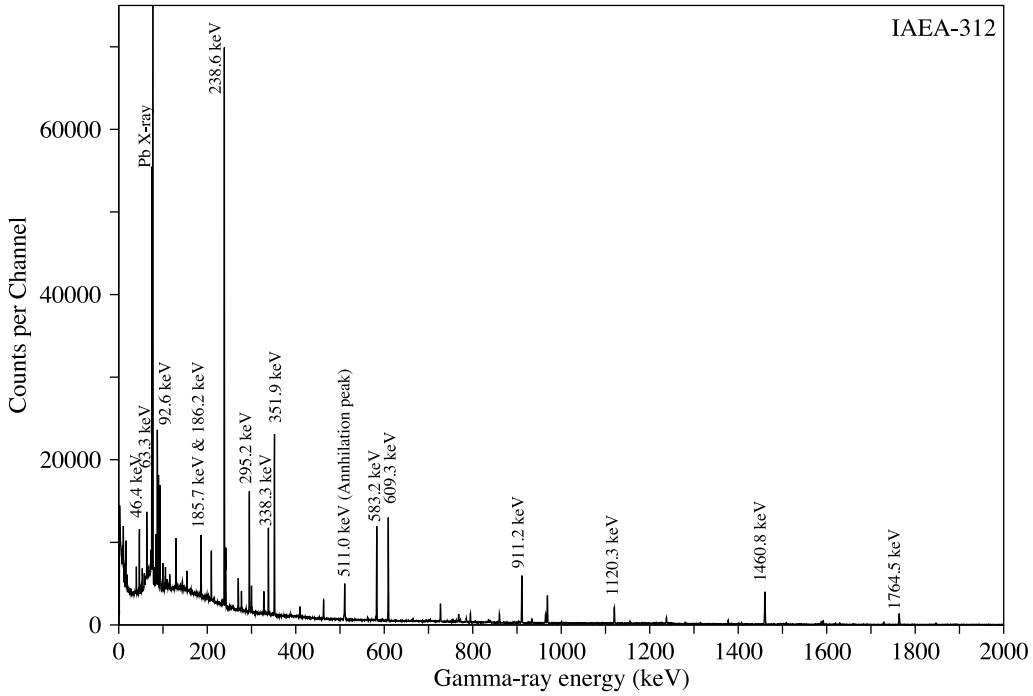

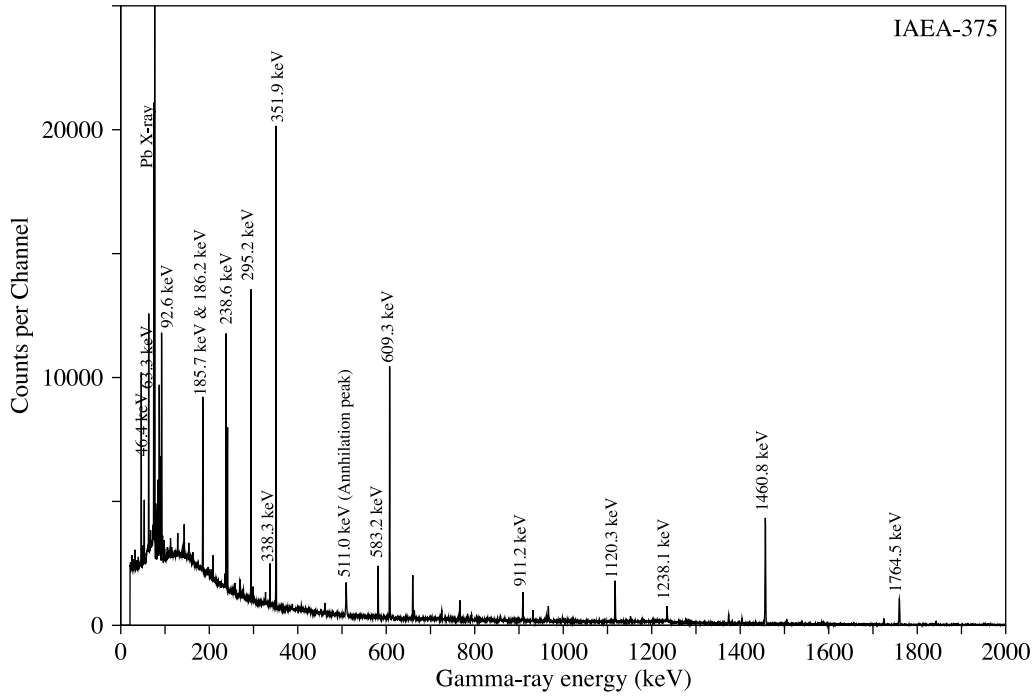
IAEA-375
Counts per Channel
Gamma-ray energy (keV)
Pb X-ray
46.4 keV
63.3 keV
92.6 keV
185.7 keV & 186.2 keV
238.6 keV
295.2 keV
338.3 keV
351.9 keV
511.0 keV (Annihilation peak)
583.2 keV
609.3 keV
911.2 keV
1120.3 keV
1238.1 keV
1460.8 keV
1764.5 keV
0
10000
20000
0
200
400
600
800
1000
1200
1400
1600
1800
2000

A.4.2 Samples from Czech Republice

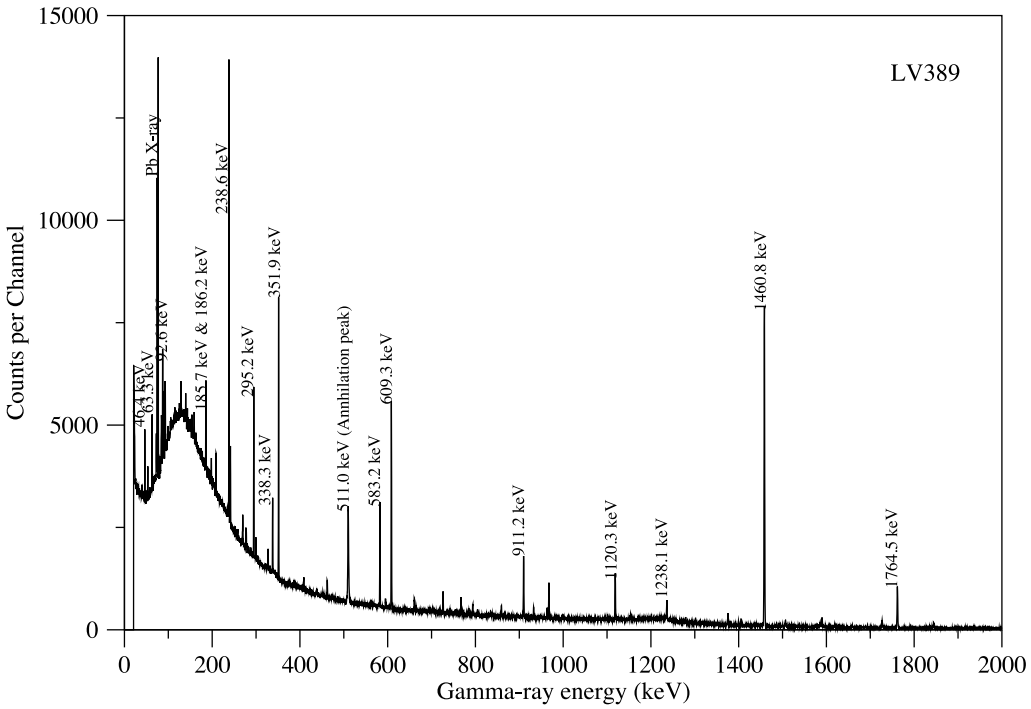

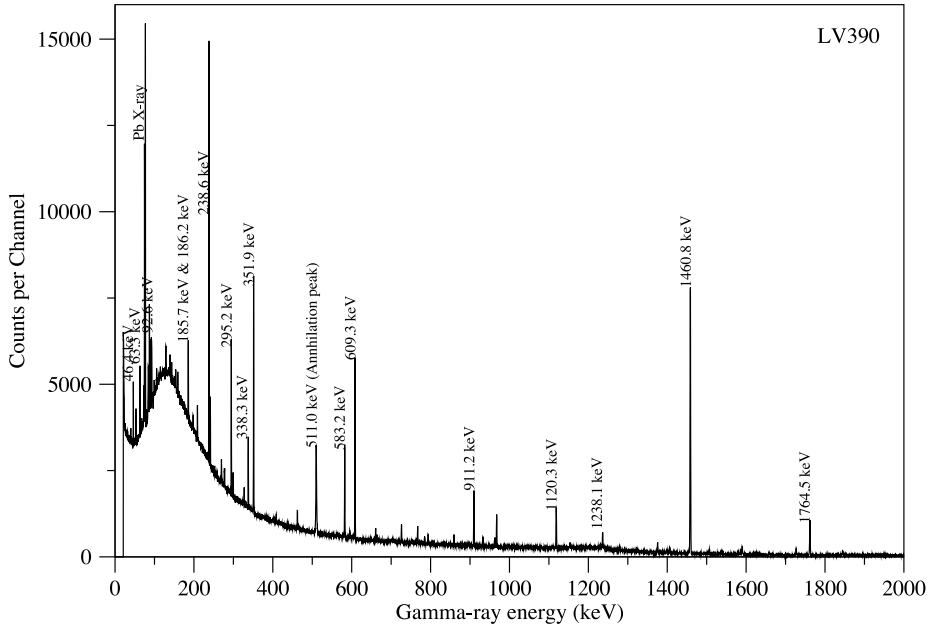

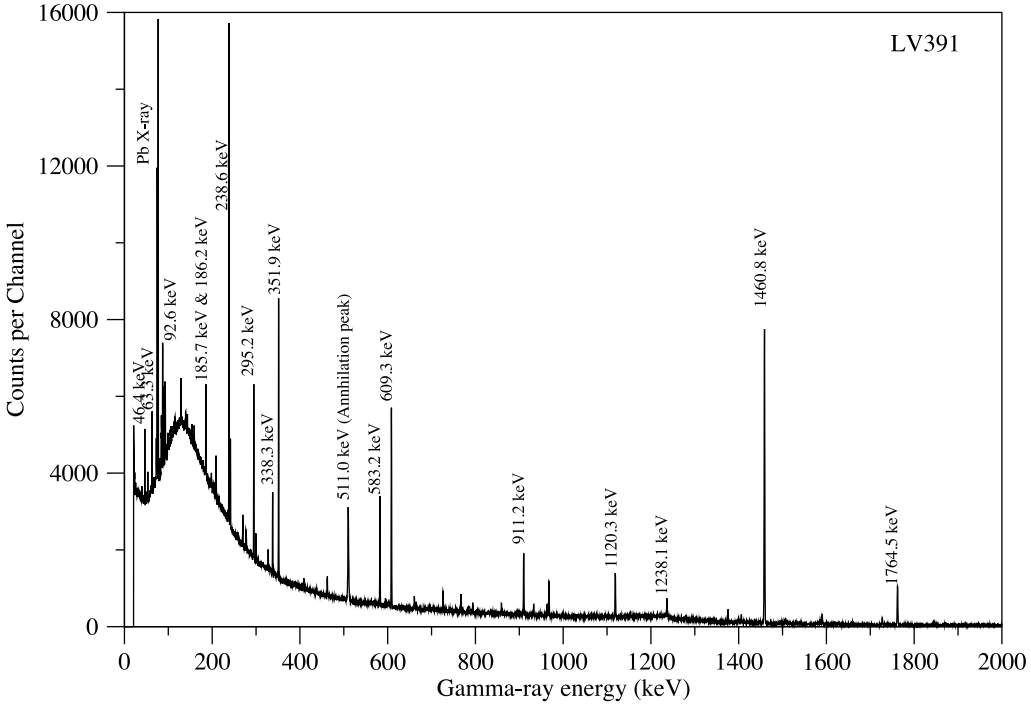

A.4.3 Sample from Germany

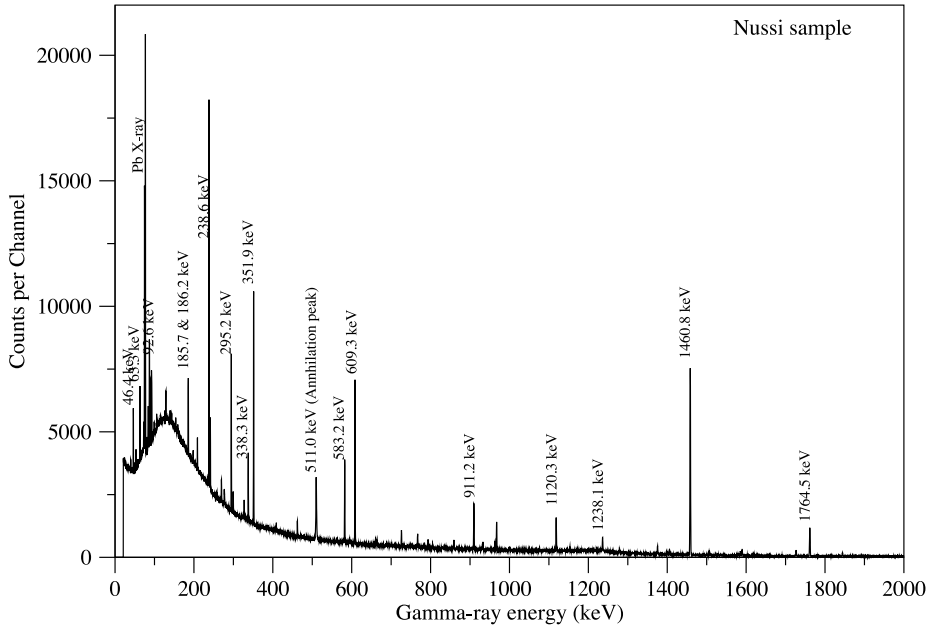

A.4.4 Samples from Australia

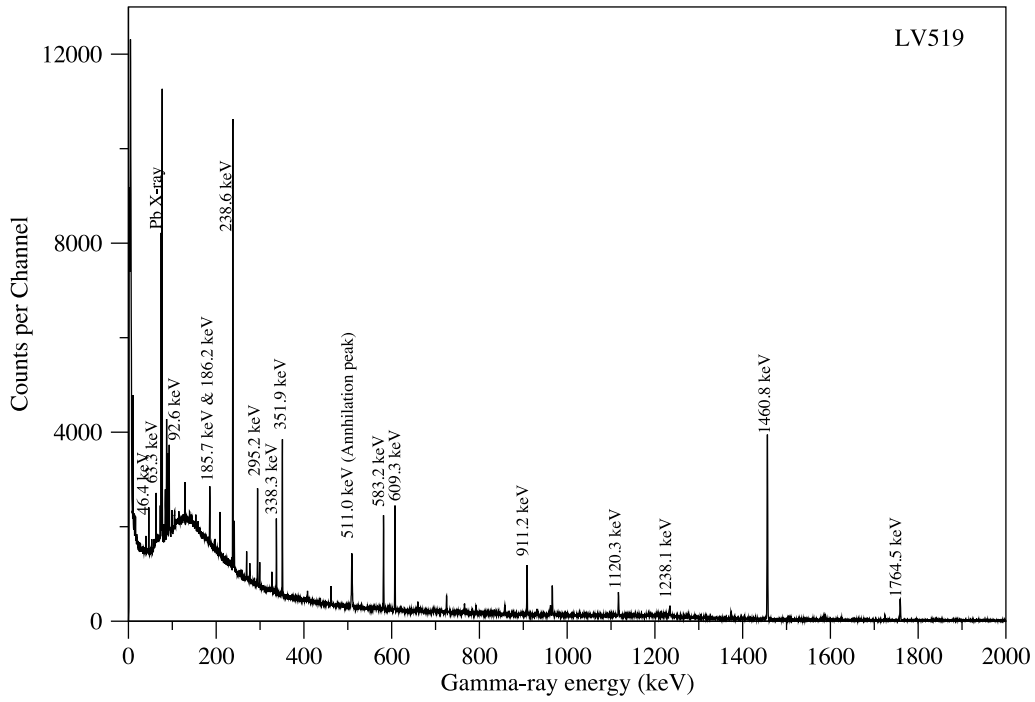

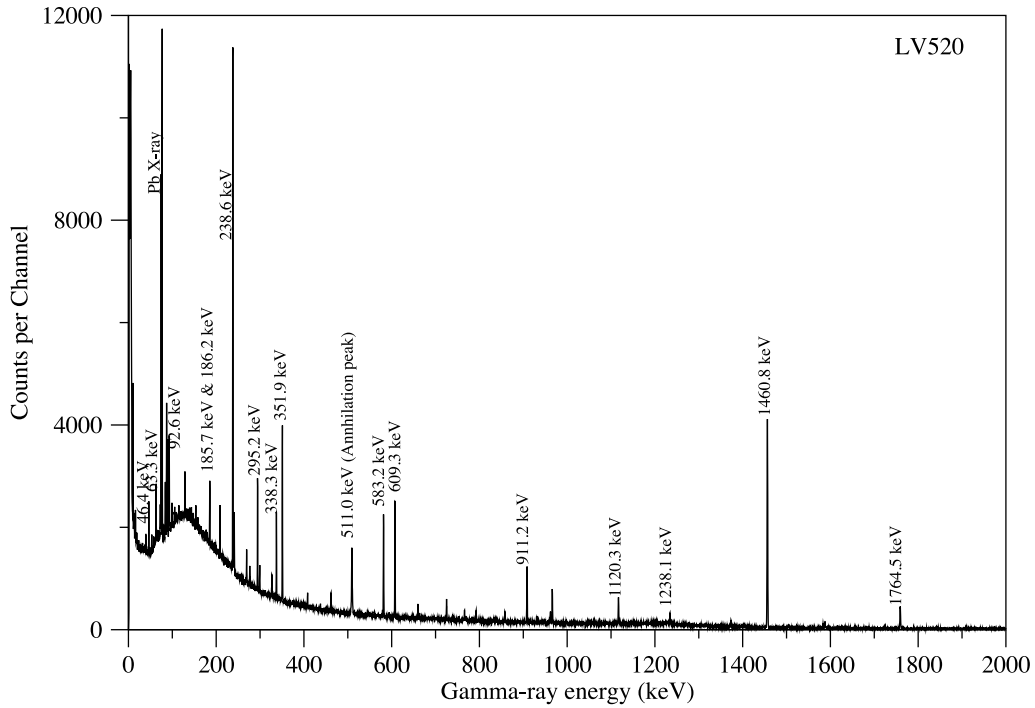

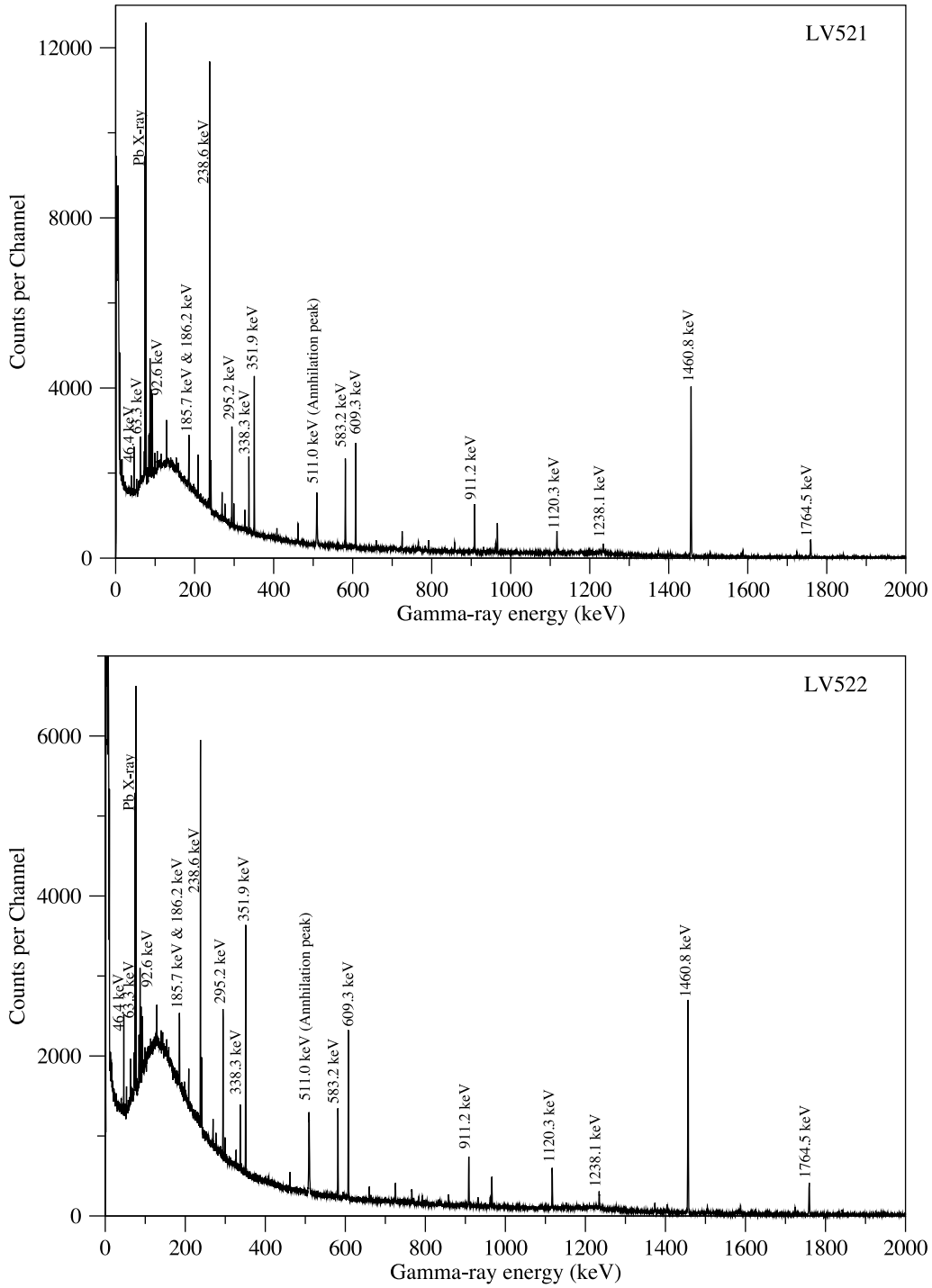

A.4.5 Samples from Namibia

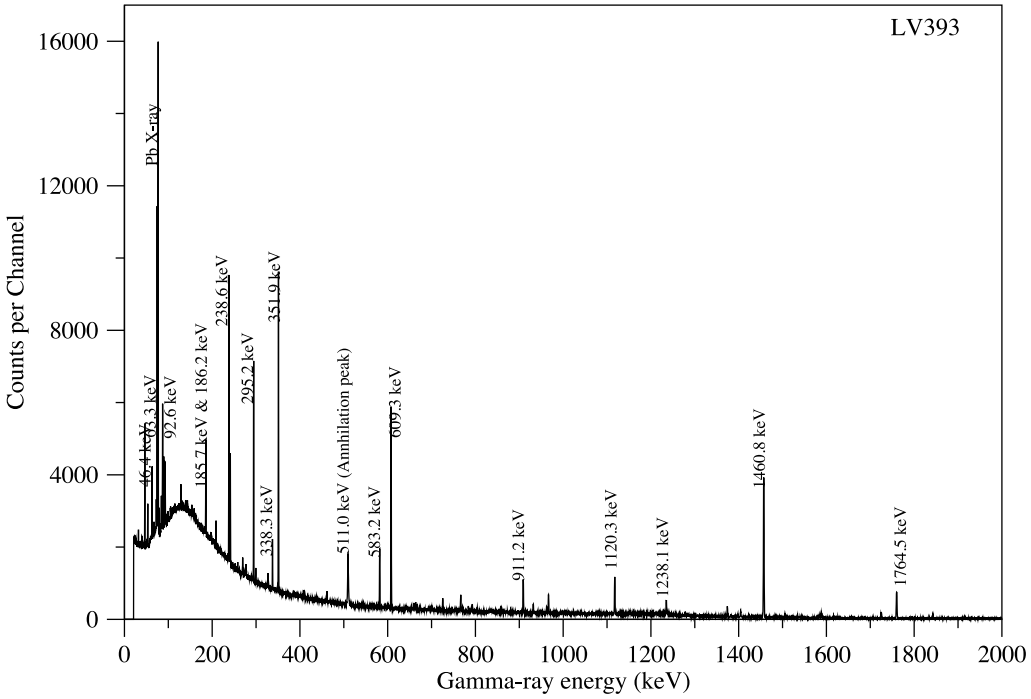
LV393
Counts per Channel
Gamma-ray energy (keV)
Pb X-ray
46.4 keV
63.3 keV
92.6 keV
185.7 keV & 186.2 keV
238.6 keV
295.2 keV
338.3 keV
351.9 keV
511.0 keV (Annhilation peak)
583.2 keV
609.3 keV
911.2 keV
1120.3 keV
1238.1 keV
1460.8 keV
1764.5 keV

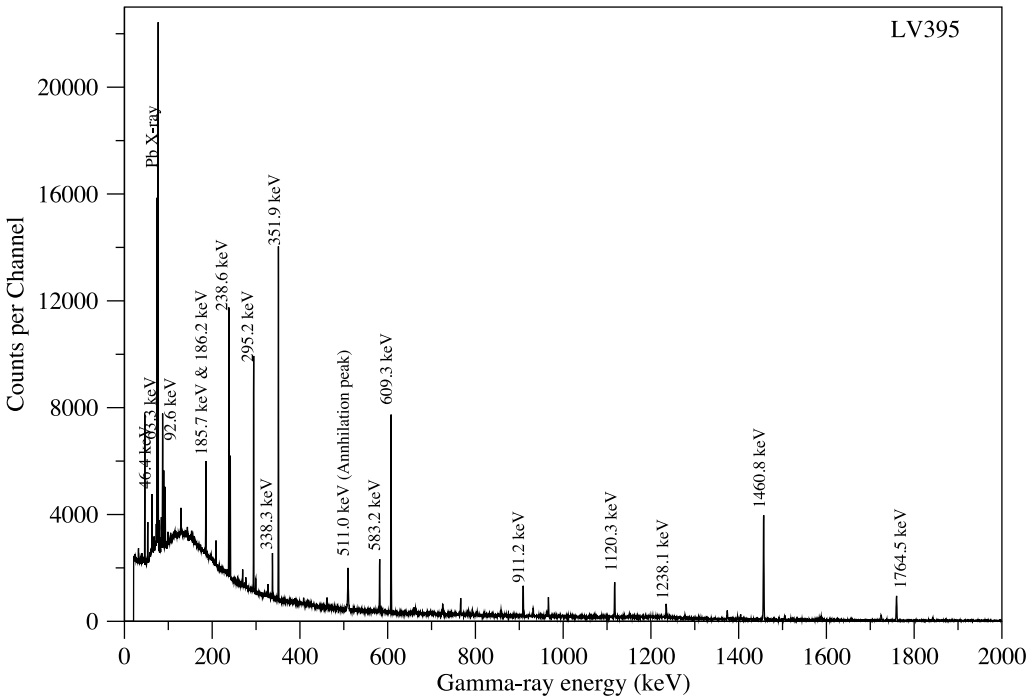
LV395
Counts per Channel
Gamma-ray energy (keV)
Pb X-ray
46.4 keV
63.3 keV
92.6 keV
185.7 keV & 186.2 keV
238.6 keV
295.2 keV
338.3 keV
351.9 keV
511.0 keV (Annhilation peak)
583.2 keV
609.3 keV
911.2 keV
1120.3 keV
1238.1 keV
1460.8 keV
1764.5 keV

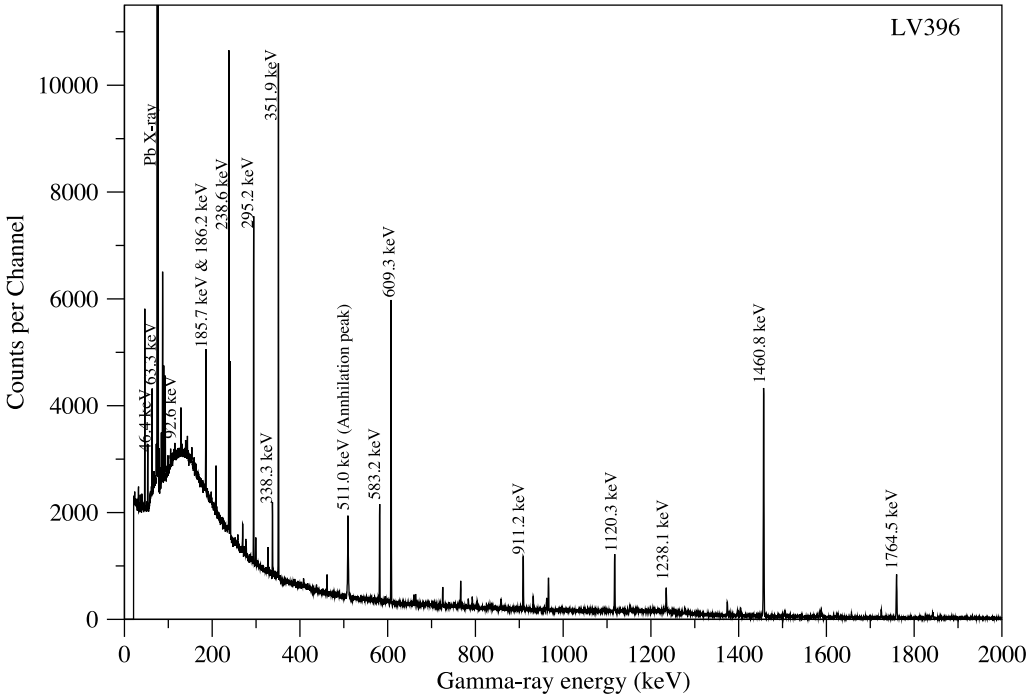
LV396
Counts per Channel
Gamma-ray energy (keV)
Pb X-ray
46.4 keV
63.3 keV
92.6 keV
185.7 keV & 186.2 keV
238.6 keV
295.2 keV
338.3 keV
351.9 keV
511.0 keV (Annhilation peak)
583.2 keV
609.3 keV
911.2 keV
1120.3 keV
1238.1 keV
1460.8 keV
1764.5 keV

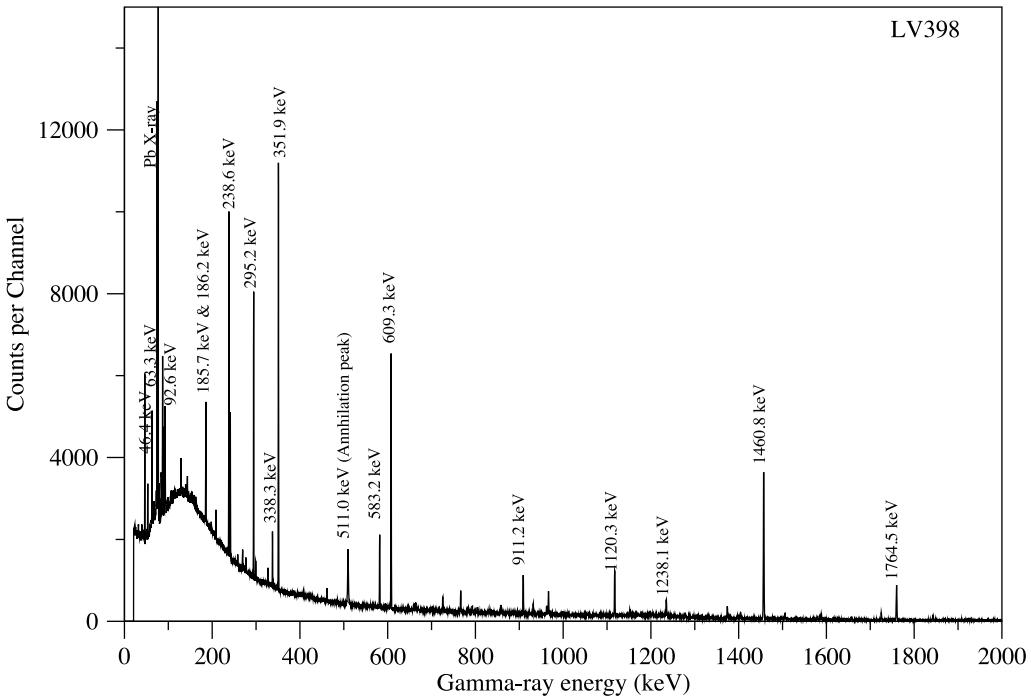
LV398
Counts per Channel
Gamma-ray energy (keV)
Pb X-ray
46.4 keV
63.3 keV
92.6 keV
185.7 keV & 186.2 keV
238.6 keV
295.2 keV
338.3 keV
351.9 keV
511.0 keV (Annhilation peak)
583.2 keV
609.3 keV
911.2 keV
1120.3 keV
1238.1 keV
1460.8 keV
1764.5 keV

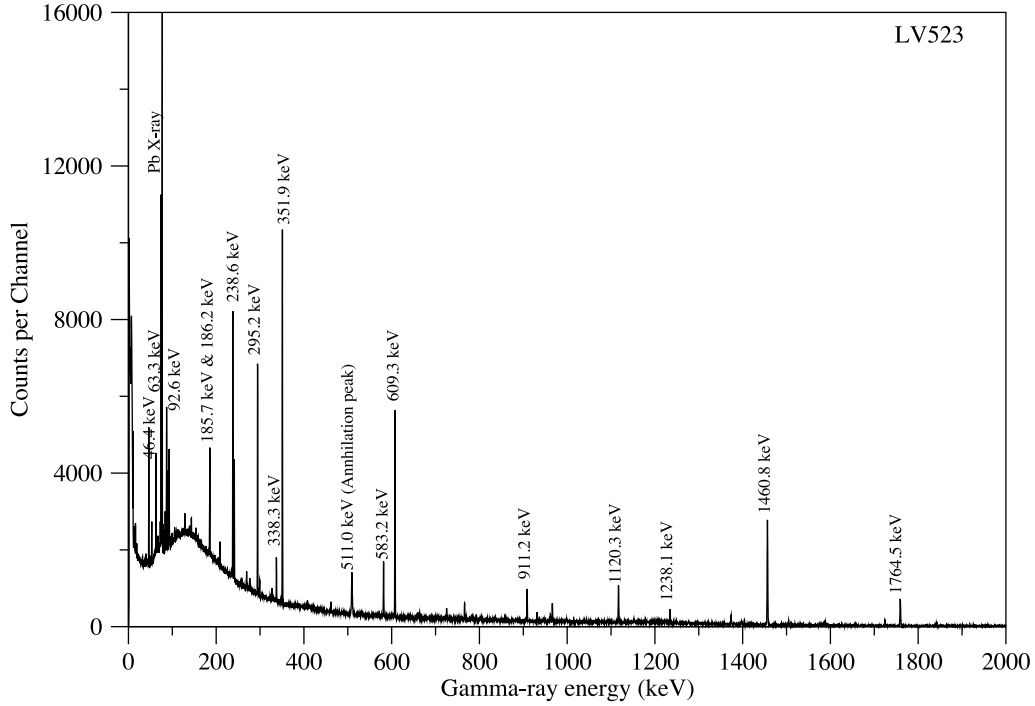
LV523
Counts per Channel
Gamma-ray energy (keV)
Pb X-ray
46.4 keV
63.3 keV
92.6 keV
185.7 keV & 186.2 keV
238.6 keV
295.2 keV
338.3 keV
351.9 keV
511.0 keV (Annhilation peak)
583.2 keV
609.3 keV
911.2 keV
1120.3 keV
1238.1 keV
1460.8 keV
1764.5 keV

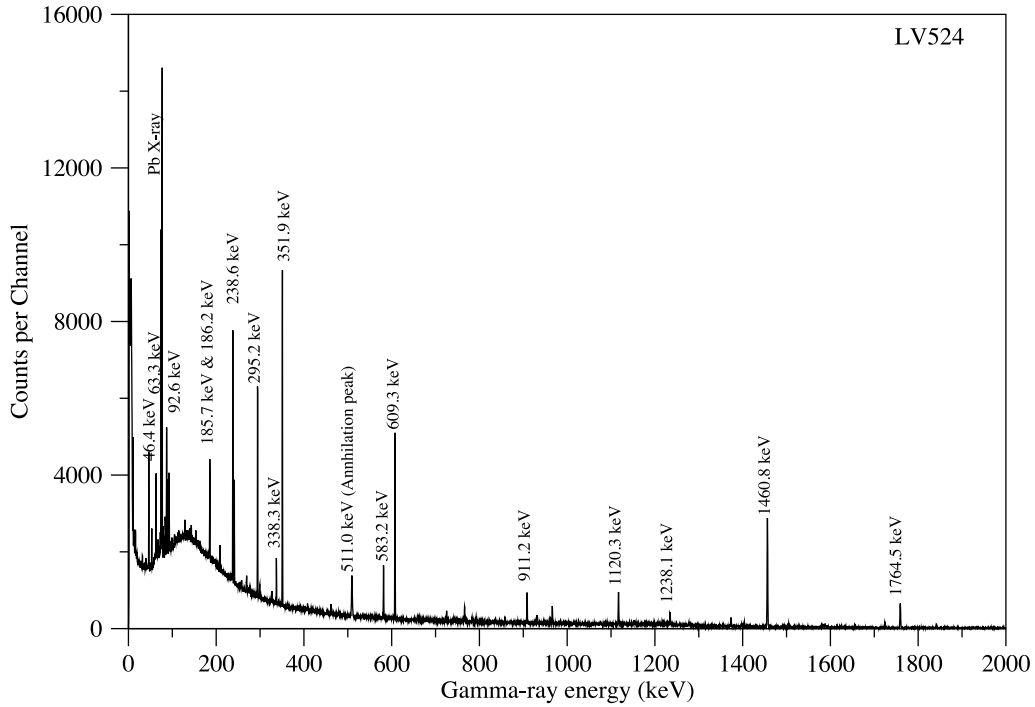
LV524
Counts per Channel
Gamma-ray energy (keV)
Pb X-ray
46.4 keV
63.3 keV
92.6 keV
185.7 keV & 186.2 keV
238.6 keV
295.2 keV
338.3 keV
351.9 keV
511.0 keV (Annhilation peak)
583.2 keV
609.3 keV
911.2 keV
1120.3 keV
1238.1 keV
1460.8 keV
1764.5 keV

Bibliography

[1] M. F. LÀnnunziata, *Handbook of Radioactivity Analysis, 3rd Edition.* Elsevier Inc, 2012.

[2] J. P. McLaughlin, E. S. Simopoulos, F. Steinhusler, *The Natural Radiation Environment VII.* Elsevier Science, 2005.

[3] A. MARIN and S. HARBISON, *An introduction to radiation protection, 5th Edition.* Hodder Arnold Education, 2006.

[4] R. Tykva and D. Berg, *Man-made and natural radioactivity in environmental pollution and radiochronology.* Kluwer Academic Publishers, 2004.

[5] N. C. on Radiation Protection and Measurements, "Natural background radiation in the united states," Report 45, 1975.

[6] M. Eisenbud and T. Gesell, ed., *Environmental Radioactivity from Natural, Industrial and Military Sources, 4th Edition.* Academic Press, San Diego, CA, 1997.

[7] National Nuclear Data Centre (NNDC), "Chart of nuclides, http://www.nndc.bnl.gov/chart/," 2012.

[8] B. David, "Environmental radioactivity in the uk: the airborne geophysical view of dose rate estimates.," *Journal of Environmental Radioactivity*, vol. 138, p. 249263, 2014.

[9] T. P. Mernagh and Y. Miezitis, "A review of the geochemical processes controlling the distribution of thorium in the earths crust and *Australia*s thorium resources.," *Journal of Geoscience* Australia, 2008.

[10] A. El-Taher, M. A. M Uosif and A. A. Orabi., "Natural radioactivity levels and radiation hazard indices in granite from aswan to wadi el-allaqi southeastern desert, egypt.," *Journal of Radiation Protection Dosimetry*, vol. 124, pp. 148 – 154, 2007.

[11] I. A. Alnour, N. Ibrahim and I, Hossain., "Concentration of ^{214}Pb, ^{214}Bi in ^{238}U series and ^{208}Tl, ^{228}Acac-228 in ^{232}Th series in granite rock in (kadugli) sudan.," *Indian Journal of Pure and Applied Physics*, vol. 50, pp. 285 – 288, 2012.

[12] J. E. Martin, *Physics for radiation protection, 1st Edition.* Wiley & Sons Inc, USA, 2000.

[13] M. Eisenbud and T. Gesell, *Environmental Radioactivity from Natural, Industrial, and Military sources, 4th Edition.* Academic Press, 1997.

[14] M. Ivanovich and R. S. Harmon, *Uranium-series disequilibrium : applications to earth, marine, and environmental sciences, 2nd Edition.* Clarendon Press, Oxford, 1992.

[15] A. S. Murray, E. Wohl and J. East, "Thermolumines- cence and excess 2z radecay dating of late quaternary fluvial sands east alligator river," *Quaternary Research*, vol. 37, pp. 29–41, 1992.

[16] B. Bourdon, G.M. Henderson, C. C. Lundstrom and and P. Turner, *Uranium-Series Geochemistry: Reviews in Mineralogy and Geochemistry*, vol. 52. The Mineral Society of America, USA, 2003.

[17] Mike. S. Lee, ed., *Mass Spectrometry Handbook.* Wiley, 2012.

[18] P. Mokkongpai and V. Cheevaporn, "Pb-210 radiometric dating of estuarine sediments from the eastern coast of thailand.," *Journal of the Science Society of Thailand*, vol. 22, pp. 313–324, 1996.

[19] M. Baskaran., ed., *Handbook of Environmental Isotope Geochemistry.* Springer, 2012.

[20] R. W. Boyle, "Geochemistry overview; in geophysics and geochemistry in the search for metallic ores," *Economic Geology Report 31*, pp. 25–31, 1979.

[21] J. B. Birks, *The Theory and Practice of Scintillation Counting, 1st Edition*. Pergamon Press Ltd, 1964.

[22] R. Hofstadter, "The detection of gamma-rays with thallium-activated sodium iodide crystals," *Physical Review*, vol. 75, p. 796, 1949.

[23] D. Kevin, "Historical account: Francis william aston: the man behind the mass spectrograph," *European Journal of Mass Spectrometry*, vol. 13, 2007.

[24] D. Sonia, V. Nicola, S. Oreste, M. Costanza and P. Francesco, "Determination of depleted uranium in human hair by quadrupole inductively coupled plasma mass spectrometry: method development and validation," *Analytical Methods*, vol. 2, pp. 1184–1190, 2010.

[25] V. Zsolt, W. Maria and M. Klaus, "Age determination of uranium samples by inductively coupled plasma mass spectrometry using direct measurement and spectral deconvolution," *Journal of Analytical Atomic Spectrometry*, vol. 25, pp. 1958–1962, 2010.

[26] S. Krishnaswami and J. Kirk Cochran, *U- Th series Nuclides in Aquatic System, ebook*. ElsevierScienceLtd, 2008.

[27] International Atomic Energy Agency, "Analytical methodology for the determination of radium isotopes in environmental samples," *IAEA Analytical Quality in Nuclear Applications No. IAEA/AQ/19*, no. 19, pp. 1–59, 2010.

[28] J. M. Olley, A. S. Murray and R. G. Robers, "The effects of disequilibria in the uranium and thorium decay chains on burial dose rates in fluvial sediments.," *Journal of*, vol. 15, pp. 751–760, 1996.

[29] R. Kritsananuwat, S. K. Sahoo , M. Fukushi, K. Pangza and S. Chanyotha, "Radiological risk assessment of ^{238}U, ^{232}Th and ^{40}K in thailand coastal sediments at selected areas proposed for nuclear power plant sites," *Journal of Radioanalytical and Nuclear Chemistry*, vol. 303, pp. 325–334, 2015.

[30] G. Yaprak and G. Yener, "Direct measurement of ^{238}U and disequilibrium state in geological samples by low energy scintillation gamma spectroscopy," *Journal of Geochemical Exploration*, vol. 42, pp. 345–350, 1992.

[31] P. G. Killeen, "Gamma ray spectrometric methods in uranium exploration - application and interpretation," tech. rep., 1979.

[32] R. Culbert and D. G. Leighton, "Low energy gamma spectrometry in the geochemical exploration for uranium," *Journal of Geochemical Exploration*, vol. 14, pp. 49–68, 1981.

[33] R. G. Roberts, N. A. Spooner, R. Jones, S. Cane, J. M. Olley, A. S. Murray and M. J. Head, "Preliminary luminescence dates for archaeological sediments on the nullarbor plain, *South Australia*," *Australian Archaeology*, vol. 42, pp. 7–16, 1996.

[34] J. M. Olley, A. S. Murray and R. G. Robers, "Disequilibrium in uranium decay series in sedimentary deposits at allens cave, nullarbor plain, *Australia*: Implications for dose rate determinations.," *Journal of Radiation Measurements,*, vol. 27, pp. 433–443, 1997.

[35] O. Agar, I. Boztosun, M. E. Korkmaz and S. F. Özmen, "Measurement of radioactivity levels and assessment of radioactivity hazardos of soil samples in karaman, turkey," *Radiation Protection Dosimetry*, vol. 162, p. 630 637, 2014.

[36] K.E. Hyde, I. Perlman and G.T. Seaborg, "The nuclear properties of the heavy element," *Englewood Cliffs, N.J., Prentice-Hall*, vol. 2, p. 1107, 1964.

[37] S. Mubarakmand, P. Chaudhry and F. I. Nagi, "Absolute determination of uranium concentration in rocks by gamma-ray spectroscopy," *Nuclear Instrumentation and Methods*, vol. 140, pp. 133–135, 1977.

[38] S. R. Joshi, "Nuclear spectrometric determination of uranium isotopes without use of radiochemical yield monitors.," *Nuclear Instruments and Methods in Physics Research*, vol. 254, pp. 349–354, 1987.

[39] E. S. Frank, M. M. Robert, B. T. Allan, R. B. George and W. P. Philip, "Intrinsic germanium detector used in borehole sinde for uranium exploration," *Nuclear Inst. and Methods in Physics Research*, vol. 138, pp. 371–380, 1976.

[40] A. M. Hassan, M. Abdel-Wahab, A. Nada, N. Walley El-dine and A. Khazbak, "Determination of uranium and thorium in egyptian monazite by gamma-ray spectrometry," *Applied Radiation and Isotopes*, vol. 48, pp. 149–152, 1997.

[41] A. Luca, "Evaluation of ^{234}Th nuclear decay data," *Applied Radiation and Isotopes*, vol. 68, pp. 1591–1594, 2010.

[42] J. L. Parker, "A correction for gamma-ray self–attenuation in regular heterogeneos materials," Report LA-8987-MS, 1981.

[43] M. E. Medhat, N. Demirc, U. A. Tarimc and O. Gurler, "Calculation of gamma-ray mass attenuation coefficients of some egyptian soil samples using monte carlo methods," *Radiation Effects Defects in Solids*, vol. 169, pp. 706–714, 2014.

[44] I. O. Okunade, G. I. Adebe. S. A. Jonah and A. O. Oladipo, "Measurement of mass attenuation coefficienct of zaria soil using gamma ray transmission method," *Nigerian Journal of Physics*, vol. 20, pp. 23–28, 2008.

[45] O. V. Gorbatyuk, E. M. Kadisov, V. L. Miller and V. L. Shashkin, "Analysis of uranium and thorium ores using a gamma ray spectrometer with a ge(li) detector," *Atomic Energy*, vol. 35, pp. 1037–1040, 1973.

[46] D. G. Coles, J. W. T. Meadows and C. L. Lindekin, "Ge(li) spectrometric measurements of isotopic uranium ratios in soils treated with aapatite-derived fertilizers," urcl- 75619, 1974.

[47] R. L. Brodzinski and N. A. Wogman, *Californium-252 in-situ activation and photon detection techniques for uranium ore deposit evaluation.* International Atomic Energy Agency (IAEA), 1976.

[48] O. V. Gorbatyuk, E. M. Kadisov, V. L. Miller and V. L. Shashkin, "Use of the 1001 kev peak of ^{234m}Pa daughter of ^{238}U in measurement of uranium concentration by hpge gamma-ray spectrometry," *Nuclear Inst. and Methods in Physics Research*, vol. 413, pp. 74–82, 1998.

[49] A. Vrtes, S. Nagy and K. Svegh, ed., *Nuclear Methods in Mineralogy and Geology: Techniques and Applications*. Springer Science Business Media, 1998.

[50] M. H. T. Hipondoka, B. Mauz, E. M. H. Nande and J. Bloemendal., "Reconnaissance survey of radionuclides in soil and possible impact on seasonal anthrax outbreak at etosha national park, namibia.," *International Science and Technology Journal of Namibia*, vol. 2, pp. 59–69, 2013.

[51] J. A. Oyedele, S. Sitoka and I. Davids., "Radionuclide concentrations in soils of *Northern Namibia*, *Southern Africa.*," *Radiation Protection and Dosimetry*, vol. 131, pp. 482–486, 2008.

[52] J. A. Oyedele, S. Shimboyo, S. Sitoka and F. Gaoseb., "Assessment of natural radioactivity in the soils of rössing uranium mine and its satellite town in western namibia, south africa.," *Nuclear Instruments and Methods in Physics Research A*, vol. 619, pp. 467–469, 2010.

[53] P. Calsteren and L. Thomas, "Uranium-series dating applications in natural environmental science.," *Earth-Science Reviews*, vol. 75, pp. 155–175, 2006.

[54] P. Guibert, C. Lahaye and F. Bechtel, "The importance of *U*-series disequilibrium of sediments in luminescence dating: *A* case study at the *Roc* de *Marsal Cave* (*Dordogne*, *Frcance.*," *Radiation Measurements*, vol. 44, pp. 223–231, 2009.

[55] E. Rutherford, J. Chadwick and C. D. Ellis, *Radiation from radioactive substances*. Cambridge University Press, 2010.

[56] J. Lilley, *Nuclear physics: principles and Applications*. Wiley & Sons, Ltd, USA, 2013.

[57] K. S. Krane, *Introductory: Nuclear Physics.* Wiley & Sons, Ltd, USA, 1988.

[58] M. F. LAnnunziata, *Radioactivity: Introduction and History.* Elsevier B.V, Amsterdam, 2007.

[59] G. F. Knoll, *Radiation Detection and Measurement, 4th Edition.* USA, 2010.

[60] G. Choppin, J. Liljenzin and J. Rydberg, *Radiochemistry and Nuclear Chemistry, 4th edn.* Elsevier Inc, 2013.

[61] R. W. Gurney and E. U. Condon *Nature*, vol. 122, p. 439, 1928.

[62] R. W. Gurney and E. U. Condon *Phys. Rev.*, vol. 33, p. 127, 1929.

[63] G. Gamow *Z. Phys.*, vol. 51, p. 204, 1928.

[64] G. Claus and B. Irne, ed., *Handbook of Particle Detection and Imaging.* Springer, 2012.

[65] L. Kirkpatrick and G. Francis, *Physics: A World View, 6th Edition.* Thomson Wadsworth, USA, 2007.

[66] H. Cember and T. E. Johnson, *Introduction to Health Physics, 4th Edition.* The McGraw-Hill Companies, Inc, 2008.

[67] G. Faure and T.M. Mensing, *Isotopes: Principles and Applications, 3rd Edition.* Wiley & Sons, Inc, New Jersey, 2005.

[68] J. H. Han and J. H. Choi, "Broad energy hpge gamma spectrometry for dose rate estimation for trapped charge dating," *Journal of Analytical Science and Technology.*, vol. 2, pp. 98–108, 2010.

[69] W. E. Burchan, *Nuclear Physics an Introduction, 2nd edn.* William Clowes & Sons, London, 1973.

[70] M. Eisenbud., *Environmental radioactivity, 3rd Edition.* Academic Press, Inc, 1987.

[71] M. Oddone, L. Giordani, F. Giacobbo, M. Mariani, S. Morandi., "Practical considerations regarding high resolution gamma-spectrometry measurements of naturally occurring radioactive samples.," *Radioanalytical and Nuclear Chemistry*, vol. 277, pp. 579–585, 2008.

[72] A. Cocherie and M. Robert, *An Introduction to ICP Spectrometries for Elemental Analysis in Inductively Coupled Plasma Mass Spectrometry.* Wiley-VCH, Inc, New York, 1998.

[73] S. M. Nelms, *ICP Mass Spectrometry Handbook, 1st Edition.* Blackwell Publishing Ltd, USA, 2005.

[74] A. T. Lebedev, *Comprehensive Environmental Mass Spectrometry, 1st Edition.* ILM Publications, USA, 2012.

[75] N. Q. Huy, T. T. Bich and N. V. Suc, "Determination of uranium and thorium isotopes in soil samples by coprecipitation.," *Journal of Radioanalytical and Nuclear Chemistry*, vol. 269, pp. 129–133, 2006.

[76] B. Mark, *Handbook of Environmental Isotope Geochemistry.* Springer, USA, 2012.

[77] Z. Karpas, *Analytical Chemistry of Uranium: Environmental, Forensic, Nuclear, and Toxicological Applications.* CRC Press, 2014.

[78] M. U. Khandaker, "High purity germanium detector in gamma-ray spectrometry.," *International Journal of Fundamental Physical Sciences (IJFPS)*, vol. 1, pp. 42–46, 2011.

[79] R. D. Evans, *The Atomic Nucleus.* McGraw-Hill Book Co, New York, 1955.

[80] G. F. Knoll, *Radiation Detection and Measurement.* John Wiley Sons, New York, 1979.

[81] G. F. Knoll, *Radiation Detection and Measurement, 3rd Edition.* John Wiley and Sons. Inc, 2000.

[82] United States Environmental Protection Agency, "application of germanium detectors to environmental monitoring interagency energy/environmental r&d program report.," p. 129, 1979.

[83] S. Bernard, A. S. Lester, K. B. Brian Kent, *Handbook of Health Physics and Radiological Health, 3rd Edition.* Williams Wilkins, Baltimore MD, 1998.

[84] G. R. Gilmore, *Practical Gamma-ray Spectrometry, 2nd Edition.* John Wiley Sons, 2008.

[85] A. Cocherie and M. Robert, *LA-MC-ICP-MS Applied to U-Pb Zircon Geochronology in Mass Spectrometry Handbook.* John Wiley and Sons, Inc, 2012.

[86] Canberra Website, "Broad energy germanium detectors (bege)." http://www.canberra.com/products/detectors/pdf/BEGe-SS-C40426.pdf, 2013.

[87] D. Barrientos, A. J. Boston, H. C. Boston, B. Quintana, I. C. Sagrado, C. Unsworth, S. Moon and J. R. Cresswell, "Chracterisation of a broad energy germanium (bege) detector.," *Journal of Nuclear Instrumentation and Methods in Physics Research A*, vol. 648, pp. S228–S231, 2011.

[88] R. Britton, J. Burnett and A. Davies, "Determining the efficiency of a broad-energy hpge detector using monte carlo simulations.," *Journal of Radioanalytical and Nuclear Chemistry*, vol. 295, pp. 2035–2041, 2013.

[89] R. G. Ordua, M. Hult, E. Andreotti and G. Marissens, "Pulse shape analysis for background reduction in bege detectors," *Journal of Analytical Science and Technology*, vol. 286, pp. 1–32, 2010.

[90] M. F. LAnnunziata, *Handbook of Radioactivity Analysis, 1st Edition.* Academic Press, USA, 1998.

[91] Canberra Website, "www.canberra .com/products/detectors/pdf/germanium-det-ss-c39606.pdf." www.Canberra .com/products/detectors/pdf/Germanium-Det-SS-C39606.pdf, 2014.

[92] A. E. M. Khater and Y. Y. Ebaid , "A simplified gamma-ray self- attenuation correction in bulk samples.," *Applied Radiation and Isotopes*, vol. 66, pp. 407–413, 2008.

[93] Y. Y. Ebaid , "On the use of reference materials in gamma ray spectrometric efficiency calibration for environmental samples.," *Journal of Radio- analytical and Nuclear Chemistry*, vol. 280, pp. 21–25, 2009.

[94] P. Appleby, "Private communication,"

[95] I. Adsley, A. Nichols and J. Toole, "Self-absorption correction in determining the ^{238}U activity of soil samples via 63.3 kev gamma ray using mcnp5 code.," *Applied Radiation and Isotopes*, vol. 71, pp. 11–20, 2013.

[96] N. Q. Huy and T. V. Luyen, "A method to determine ^{238}U activity in environmental soil samples by using 63.3 kev-photopeak-gamma hpge spectrometer.," *Applied Radiation and Isotopes*, vol. 61, pp. 1419–24, 2005.

[97] J. C. Aguiar, E. Galiano and J. Fernandez, "Peak efficiency calibration for attenuation corrected cylindrical sources in gamma ray spectrometry by the use of point source.," *Applied Radiation and Isotopes*, vol. 64, p. 16431647, 2006.

[98] M. Bruggeman, L. Verheyen, T. Vidmar and B. Liu., "Assessing sample attenuation parameters for use in low-energy efficiency transfer in gamma-ray spectrometry.," *Applied Radiation and Isotopes*, vol. 109, pp. 547–550, 2015.

[99] B. Gillespie and M. Zebarth, "Comparison of a variety of gamma attenuation corrections techniques for different waste materials.," 1992.

[100] M. S. Shackley, *X-Ray Fluorescence Spectrometry (XRF) in Geoarchaeology.* Springer, USA, 2011.

[101] R. V. Grieken and A. Markowicz , *Handbook of X-ray Spectrometry, 2nd Edition.* CRC Press, Taylor and Francis Group, 2001.

[102] M. S. Shackley , *An Introduction to X-Ray Fluorescence (XRF) Analysis in Archaeology, in X-Ray Fluorescence Spectrometry (XRF) in Geoarchaeology.* Springer Link, 2011.

[103] F. L. Bronson, "Validation of the accuracy of the labsocs software for mathematical efficiency calibration of ge detectors for typical laboratory samples.," *Journal of Radioanalytical and Nuclear Chemistry*, vol. 255, p. 137141, 2003.

[104] Canberra, "Model s574 labsocs calibration software.," 2013.

[105] R. L. Njinga and V. M. Tshivhase, "A comparison of labsocs and source-based full energy efficiency generation in measurements.," *International Journal of Advanced Research in Physical Science*, vol. 3, pp. 4–8, 2016.

[106] M.H.T. Hipondoka, B. Mauz, J. Kempf, S. Packman, R.C. Chiverrell, J. Bloemendal, "Chronology of sand ridges and the late quaternary evolution of the etosha pan, namibia," *Geomorphology*, vol. 25, pp. 553 – 563, 2014.

[107] N. L. Hassing, J. W. Wanless and L. J. Philips, "The effects of counting time on reliably detectable activity (rda) when assessing contamination monitor performance," *Waste Management Symposium*, vol. 22, pp. 267–273, 1990.

[108] K. H. Kim and W. C. Burnett, "Gamma-ray spectrometric determination of uranium-series nuclides in marine phosphorites," *Analytica Chemistry*, vol. 55, p. 1796.

[109] "Gamma-ray spectrometric methods in uranium exploration-application and interpretation," tech. rep.

[110] D.C. Radford, "Private communication,"

[111] I. Adsley, A. Nichols and J. Toole, "Decay of ^{234}Th and daughter ^{234m}Pa in secular equilibrium. resolution of observed anomalies," *Applied Radiation and Isotopes*, vol. 32, 2000.

[112] C. A. Papachristodoulou, P. A. Assimakopoulos, N. E. Patronis and K. G. Ioannides, "Use of hpge y-ray spectrometry to assess the isotopic composition of uranium in soils.," *Journal of Environmental Radioactivity*, vol. 64, p. 195203, 2003.

[113] F. De Corte, H. Umans, D. Vandenberghe, A. De Wispelaere and P. Van den haute, "Direct gamma-spectrometric measurement of the ^{226}Ra 186.2 kev line for detecting ^{238}U/^{226}Ra disequilibrium in determining the environmental dose rate for the luminescence dating of sediments.," *Applied Radiation and Isotopes*, vol. 63, pp. 589–598, 2005.

[114] M. Dowdall, . G. Selnaes, J. P. Gwynn and C. Davids, "Simultaneous determination of ^{226}Ra and ^{238}U in soil and environmental materials by gamma-spectrometry in the asbsence of radium progeny equilibrium," *Journal of Radioanalytical and Nuclear Chemistry*, vol. 261, pp. 513–521, 2004.

[115] X. Hou and P. Roos, "Critical comparison of radiometric and mass spectrometric methods for the determination of radionuclides in environmental, biological and nuclear waste samples.," *Analytica Chimica Acta*, vol. 608, pp. 105–139, 2008.

[116] M. García-Talaveraa, J.P. Laedermannb, M. De combaz, M.J. Daza, B. Quintana, "Coincidence summing corrections for the natural decay series in gamma-ray spectrometry," *Radiation and Isotopes*, vol. 54, pp. 769 – 776, 2001.

[117] M. C. Lepy, T. Altzitzoglou, M.J. Anagnostakis, D. Arnold, M. Capogni, A. Ceccatelli, P. De Felice, R. Dersch, P. Dryak, A. Fazio, L. Ferreux, M. Guardati, J.B. Han, S. Hurtado, K.L. Karfopoulos, S. Klemola, P. Kovar, K.B. Lee, R. Ocone, O. Ott, O. Sima, S. Sudar, A. Svec, Chau Van Tao, Tran Thien Thanh and T. Vidmar, "Intercomparison of methods for coincidence summing corrections in gamma-ray spectrometry," *Journal of Applied Radiation and Isotopes*, vol. 68, pp. 1407 – 1412, 2010.

[118] A. M. Ababneh and M. M. Eyadeh, "Coincidence summing corrections in hpge gamma- ray spectrometry for marinelli-beakers geometry using peak to total (p/t)

calibration," *Journal of Radiation Research and Applied Sciences*, vol. 8, pp. 323 – 327, 2015.

[119] J. E. Martin, *Physics for Radiation Protection: A Handbook, 2nd Edition, Completely Revised and Enlarged*. Wiley & Sons Inc, USA, 2008.

[120] E. Browne, J. M. Dairiki and R. E. Doebler, *Table of Isotopes, 7th Edition*. Wiley and Sons Inc, 1978.

[121] S. S. M. Wong, *Introductory Nuclear Physics, Second Edition*. Wiley-VCH Verlag GmbH, Weinheim, Germany, 1998.

[122] R. M. Yousuf and K. O. Abullah, "Measurement of natural radioactivity in soil collected from the eastern of sulaimany governorate in kurdistanregion, iraq," *Journal of Science and Technology*, vol. 3, pp. 749 – 757, 2013.

[123] M. Tzortzis and H. Tsertos., "Determination of thorium, uranium and potassium elemental concentrations in surface soils in cyprus.," *Journal of Environmental Radioactivity*, vol. 77, pp. 325 – 338, 2004.

[124] International Atomic Energy Agency, "Guidelines for radioelement mapping using gamma ray spectrometry data," *IAEA Analytical Quality in Nuclear Applications No. IAEA-TECDOC-1363*, pp. 1–179, 2003.

[125] S. Krishnaswami and J. Kirk Cochran, ed., *U-Th Series Nuclides in Aquatic Systems*. Radioactivity in the Environment, 2008.

[126] M. Gascoyne, ed., *Geochemistry of the Actinide and Their Daughters*. Clarendon Press, 1992.

[127] B. M. Rajesh, M. S. Chandrashekara, P. Nagaraja, A. Chandrashekara and L. Paramesh, "Distribution of 226ra and 222rn in bore well and lake water of mysore taluk, karnataka state, india.," *International Journal of Environmental Science*, vol. 4, pp. 558–566, 2014.

[128] H. W. Kirby and M. L. Salutsky, "The radiochemistry of radium.," vol. NAS-NS3057, pp. 558–566, 1964.

[129] M. N. V. Prasad, K. S. Sajwan and R. Naidu, *Trace Elements in the Environment: Biogeochemistry, Biotechnology, and Bioremediation.* CRC Press Taylor and Francis Group, 2005.

[130] B. Muaz, "Private communication,"

[131] Peter Volgyesi, Zoltan Kis, Zsuzsanna Szabo and Csaba Szabo, "Using the 186-kev peak for ^{226}Ra activity concentration determination in hungarian coal-slag samples by gamma-ray spectroscopy," *Journal of Radioanalytical and Nuclear Chemistry*, vol. 302, p. 375383, 2015.

[132] J.R. Prescott and J.T. Hutton., "Environmental dose rates and radioactive disequilibrium from some *Australian* luminescence dating sites.," *Quaternary Geochronology*, vol. 14, pp. 439 – 448, 1995.